El 107

ACTA POLYTECHNICA SCANDINAVICA

ELECTRICAL ENGINEERING SERIES No. 107

Magnetic Field Analysis of Electric Machines Taking Ferromagnetic Hysteresis into Account

JÚLIUS SAITZ

Helsinki University of Technology
Laboratory of Electromechanics
P.O.Box 3000
FIN-02015 HUT
Finland

Dissertation for the degree of Doctor of Science in Technology to be presented with due permission for public examination and debate in Auditorium S1 at Helsinki University of Technology (Espoo, Finland) on the 6th of November, 2001, at 12 o'clock.

ESPOO 2001

Saitz, J. **Magnetic Field Analysis of Electric Machines Taking Ferromagnetic Hysteresis into Account**. Acta Polytechnica Scandinavica, Electrical Engineering Series No. 107, Espoo 2001, 123 p. Published by the Finnish Academies of Technology.
ISBN 951-666-583-7, ISSN 0001-6845

Keywords: electric machines, ferromagnetic hysteresis, finite element analysis, losses, Preisach models

Abstract

This thesis deals with the magnetic field analysis of electric machines by means of the finite element method taking the ferromagnetic hysteresis into account. The hysteresis is considered through a vector Preisach model, consisting of scalar Preisach models distributed along a finite number of angular directions. The incorporation of the vector hysteresis model into a two-dimensional time-stepping field solution in terms of the magnetic vector potential is accomplished by the Fixed-Point iterative technique. A combination of the field formulations and circuit equations of the windings presents a general voltage-driven solution with hysteresis, applicable to a 2D analysis of any electric machine. The time discretization is performed by using the Crank-Nicholson algorithm and the rotation of the rotor is modeled by moving the finite element mesh in the air gap.

The verification of the scalar hysteresis model has been performed by comparison to dc-field measurements. The vector hysteresis model has been validated indirectly by the computation of the hysteresis torque and the associated losses in a rotor structure of an induction motor. The computation of the power balance in a simplified structure has been used to accredit the accuracy of the presented numerical techniques.

The method of analysis has been applied to the magnetic field simulation and core loss computation of three individual cage induction motors. The computations have been carried out for the motors running at synchronous speeds and supplied from a sinusoidal voltage source. The computed core losses have been compared with the measured ones, yielding generally acceptable results. The influence of the time-step size and the number of scalar models included in a vector model has been studied. Many computations with the presented method, which takes account of the ferromagnetic hysteresis already when solving the field, have shown that although the technique is rather slow, it is robust, reliable and always convergent. These findings are the most important results of the thesis.

Preface

This work was carried out in the Laboratory of Electromechanics at Helsinki University of Technology. The work is part of a research project concerning losses in rotating electric machines.

I would like to express my gratitude to Professor Tapani Jokinen, Head of the Laboratory of Electromechanics, for the guidance, advice and encouragement during the course of this work. I am obliged to Professor Antero Arkkio for invaluable discussions, help during the measurements and some measured data provision. Consultations with Professor Asko Niemenmaa, Dr. Juhani Tellinen, Doc. Ing. Valéria Hrabovcová, Ph.D., M.Sc. Jan von Pfaler, Lic.Sc. Áron Szücs and RNDr. Tomáš Madaras, Ph.D. are gratefully acknowledged.

I thank my mother Mária Eleonóra and my brother Peter for constant understanding, encouragement and support.

I am grateful to Mr. Nigel Kimberley for revision of the language.

The financial support of the Academy of Finland (Graduate School of Electrical Engineering), the Research Foundation of Helsinki University of Technology, the Foundation of Imatran Voima and the SIL Foundation is thankfully appreciated.

Espoo, September 2001

Július Saitz

Contents

List of symbols

$\boldsymbol{A}$, A	magnetic vector potential, z-component of $\boldsymbol{A}$ and approximate solution in FEM
$\mathbf{A}$, A_j	column vector of the nodal values of A, j-th component of $\mathbf{A}$
A_b	z-component of $\boldsymbol{A}$ on the boundary in the hysteresis torque computation (page 66)
$\hat{A}_\mathrm{b}$	peak value of A_b
$\boldsymbol{B}$, B	magnetic flux density, magnitude of $\boldsymbol{B}$
$\hat{B}$	amplitude of the fundamental flux density component in the air gap (page 67)
$\underline{\mathbf{B}}$	two-column vector of $\boldsymbol{B}$ in elements, defined by (3.29) on page 50
B^e	e-th component of $\underline{\mathbf{B}}$
B_i^m	i-th component of the measured flux density values identifying a limiting curve (page 34)
$B_{k\mathrm{maj}}$	major axis of the ellipse traced by the k-th harmonic component of $\boldsymbol{B}$
B_lim	descending branch of the limiting hysteresis loop (page 34)
$B_\mathrm{lim}^\mathrm{s}$	descending branch of the limiting hysteresis loop associated with $\mathbb{B}^\mathrm{s}$ (page 36)
$B_\mathrm{lim}^\mathrm{s\text{-}v}$	descending branch of the limiting hysteresis loop associated with $\mathbb{B}^\mathrm{s\text{-}v}$ (page 36)
B_p	peak value of $\boldsymbol{B}$
B_r	radial component of $\boldsymbol{B}$
B_φ	tangential component of $\boldsymbol{B}$
B_{φ_n}	geometrical projection of $\boldsymbol{B}$ in the direction defined by angle φ_n
B_{rk}	peak value of k-th harmonic component of B_r
$B_{\varphi k}$	peak value of k-th harmonic component of B_φ
B_s	saturation value of the magnetic field density
B_sv	single-valued function of the flux density defined by (2.16) on page 37
B_z	magnetic field density defined in Fig. 2.1 (page 36)
C_class	classical loss coefficient, defined by (3.56) on page 60
C_hys, n_hys	hysteresis loss coefficients
C_exc	excess loss coefficient
$\mathrm{C_u}$	constant defined by (3.42) on page 54
$\mathbf{D}$, D_{ij}	matrix defined by (3.24), i, j-th component of $\mathbf{D}$ defined by (3.20) on page 49
d	lamination thickness

$\mathbf{E}$	matrix defined by (3.43) on page 55
$\boldsymbol{e}_{\varphi}$, $\boldsymbol{e}_{\varphi_n}$	unit vectors in directions given by polar angles φ and φ_n, respectively
$\boldsymbol{e}_z$	unit vector in the z-direction
$F(H)$	distribution function defined by (2.10) and (2.11) on page 35
f	frequency
$\mathbf{G}_{\mathrm{D1}}$	matrix defined by (3.40) on page 53
$\mathbf{G}_{\mathrm{D2}}$	matrix defined by (3.41) on page 54
$\mathbf{g}$	column vector defined by (3.44) on page 55
$\boldsymbol{H}$, H	magnetic field intensity, magnitude of $\boldsymbol{H}$
$\underline{\mathbf{H}}$	two-column vector of $\boldsymbol{H}$ in elements, defined by (3.29) on page 50
H^e	e-th component of $\underline{\mathbf{H}}$
H_{lim}	descending branch of the limiting hysteresis loop (page 34)
$H_{\mathrm{lim}}^{\mathrm{s}}$	descending branch of the limiting hysteresis loop associated with $\mathcal{H}^{\mathrm{s}}$ (page 36)
$H_{\mathrm{lim}}^{\mathrm{s\text{-}v}}$	descending branch of the limiting hysteresis loop associated with $\mathcal{H}^{\mathrm{s\text{-}v}}$ (page 36)
H_i^{m}	i-th component of the measured magnetic field values identifying a limiting curve (page 34)
H_{s}	saturation value of the magnetic field intensity
H_{z}, H_0	magnetic field intensities defined in Fig. 2.1 (page 36) and by (2.17), respectively
H_{φ}	geometrical projection of $\boldsymbol{H}$ into the direction defined by angle φ
h_{a}, h_{b}	"up" and "down" switching fields of the elementary hysteresis operator (page 18)
$\mathbf{I}$	unity $m \times m$ matrix
$\mathbf{i}$, i_i	column vector of phase currents, current of phase i
$\boldsymbol{J}$, J	electric current density, z-component of $\boldsymbol{J}$
k	iteration step; harmonic order
L_{ew}	end-winding inductance
l_{Fe}	equivalent core length of the machine
$\boldsymbol{M}$, M	magnetization, magnitude of $\boldsymbol{M}$
m	number of phases of the stator winding
N_{FC}	number of Fourier components included in the analysis
N_{a}	number of free (active) nodes in a finite element mesh
$N_{\mathrm{c}i}$	number of turns of a coil of the phase i

N_d	number of directions (scalar models) included in a vector model (Fig. 2.2, page 38)
N_i	global shape function in the finite element method corresponding to the node i
N_n	the total number of nodes in the finite element mesh
$N_\mathrm{tot}^\mathrm{m}$	total number of measured points on a limiting curve (page 34)
N_s	number of symmetry sectors included in the analysis
n	direction index in a vector model definition (2.19), page 38; time step
$\mathbf{P}$, P_j	column vector defined by (3.25), j-th component of $\mathbf{P}$ defined by (3.21) on page 49
$P_\mathrm{vhm}^\mathrm{hys}$	hysteresis loss computed by means of a vector hysteresis model
P^in	input power
P_δ^in	input air-gap power in the computation of the hysteresis torque (page 67)
P^out	output power on the shaft
p^class	classical loss density, defined by (3.55) on page (60)
$p_\mathrm{sin}^\mathrm{class}$	classical loss density under sinusoidal flux, defined by (3.59) on page (62)
p^core	total core loss density
p^exc	excess loss density, defined by (3.57) on page (61)
$p_\mathrm{sin}^\mathrm{exc}$	excess loss density under sinusoidal flux, defined by (3.60) on page (62)
$p_\mathrm{sin}^\mathrm{hys}$	hysteresis loss density under sinusoidal flux, defined by (3.58) on page (61)
$p_\mathrm{st}^\mathrm{hys}$	hysteresis loss density in the stator core, defined by (3.47) on page (58)
$p_\mathrm{rt}^\mathrm{hys}$	hysteresis loss density in the rotor core, defined by (3.54) on page (60)
$p_\mathrm{st}^\mathrm{hys\text{-}alt}$	hysteresis loss density in the stator under alternating flux, defined by (3.49) on page 59
$p_\mathrm{st}^\mathrm{hys\text{-}rot}$	hysteresis loss density in the stator under rotating flux, defined by (3.50) on page 59
p	number of pole pairs of the motor
Q_R	number of rotor bars
$\boldsymbol{R}_\mathrm{FP}$, $\underline{\mathbf{R}}_\mathrm{FP}$	Fixed-Point residual; column vector of $\boldsymbol{R}_\mathrm{FP}$ in elements, defined by (3.29) on page 50
R_FP^e	e-th component of $\underline{\mathbf{R}}_\mathrm{FP}$
R_s	total phase winding resistance
r, φ, z	cylindrical coordinates, subscript: φ-, z-components of quantities
r_in , r_out	inner and outer radii of the air-gap
S_i	cross-sectional area of the i-th phase coil side
S_n	cross-sectional area of the n-th rotor bar
S_ag	cross-sectional area of the air gap

$\mathbf{S}$, $S_{i,j}$	coefficient matrix defined by (3.22), i, j-th component of $\mathbf{S}$ defined by (3.18) on page 49
$\mathbf{T}$, T_{ij}	mass matrix defined by (3.23), i, j-th component of $\mathbf{T}$ defined by (3.19) on page 49
T_{e}	electromagnetic torque
T_{h}	hysteresis torque, defined by (3.75) on page 68
t	time
Δt	time interval in the time-stepping method
$\mathbf{u}$, u_i	column vector of phase voltages, voltage of phase i
x, y, z	Cartesian coordinates, subscript: x-, y-, z-components of quantities
$\mathbf{Z}_{\mathrm{LD}}$, $\mathbf{Z}_{\mathrm{RD}}$	matrices defined in association with (3.38) on page 53

α	angle of lag between $\boldsymbol{H}$ and $\boldsymbol{B}$
β_i	functions defined by (3.6) on page 46
$\hat{\gamma}(h_{\mathrm{a}}, h_{\mathrm{b}})$	elementary hysteresis operator (page 18)
φ_0	angle associated with vector hysteresis models (page 38)
φ_n	angle of the n-th direction in a vector hysteresis model (2.21), Fig. 2.2 on page 38
$\Delta\varphi$	discretization angle in a vector hysteresis model (page 38)
μ_0	permeability of free-space
$\mu^{\mathrm{s}}(h_{\mathrm{a}}, h_{\mathrm{b}})$	scalar Preisach distribution function
$\mu^{\mathrm{v}}(h_{\mathrm{a}}, h_{\mathrm{b}})$	vector Preisach distribution function
μ_{sv}	permeability defined by (2.15) on page 36
μ_{z}	permeability defined in Fig. 2.1 (page 36)
ν_{sv}	single-valued function of the magnitude of $\boldsymbol{B}$
ν_0	reluctivity of free space
ν_{xy}	function of position defined by (3.10) on page 47
$\nu_{\max}$, $\nu_{\min}$	maximum and minumum slopes of a nonlinear curve (page 21)
ν_{FP}	Fixed-Point coefficient (page 21)
ϑ_{rk}, $\vartheta_{\varphi k}$	phases of k-th harmonic components of B_r and B_φ, respectively
θ	angular position of $\boldsymbol{B}$
σ	conductivity
Ω	solution region

ω_e	electrical angular frequency
ω_m	mechanical angular frequency
ξ	trial function in the weighted-residual approach
Ψ_i	flux linkage of the *i*-th phase associated with the two-dimensionally modeled core region

$\mathcal{B}^s$	scalar hysteresis model, direct Preisach model (page 32)
$\mathcal{B}^{s\text{-}v}$	scalar hysteresis model working under a vector hysteresis model, direct Presach model (page 33)
$\mathcal{B}^v$	vector hysteresis model, direct Preisach model (page 32)
$\mathcal{F}^v$	nonlinear function defined by (3.2) on page 45
$\mathcal{F}_r^v$	nonlinear function defined by (3.70) on page 66
$\mathcal{H}^s$	scalar hysteresis model, inverted Preisach model (page 33)
$\mathcal{H}^{s\text{-}v}$	scalar hysteresis model working under a vector hysteresis model, inverted Presach model (page 33)
$\mathcal{H}^v$	nonlinear function (page 21); vector hysteresis model, inverted Presach model (page 33)

Abbreviations:

EHO	Elementary Hysteresis Operator (page 18)
FEM	Finite Element Method
NRM	Newton-Raphson Method (page 20)
FPT	Fixed-Point Technique (page 20)
B-FPT	B-version of FPT (page 20)
H-FPT	H-version of FPT (page 20)
CPM	Classical Preisach Model (page 18)
VPM	Vector Preisach Model (page 19)

1 Introduction

1.1 Background of the study

A substantial part of the losses in electric machines is the loss in the iron core. For successful design of electric machines it is important to get as accurate information about this loss as possible. The information about the core loss is closely related to the knowledge of the magnetic field in the machine. Therefore, the ability to produce an accurate prediction of the flux density distribution throughout the motor both in spatial and time coordinates is of major concern.

Owing to the complicated operation and geometry of electric machines, the variation of the magnetic field in the machine is very complex, and a numerical technique is needed to solve this field. In this respect, the finite element method (FEM) has proved to be an efficient tool, which is widely used in the analysis of the magnetic field in electric machines. However, the three-dimensionality and time-dependency of the magnetic field in an electric machine render a comprehensive solution too large a task even for present-day computers. To ease the computational burden, it is a common practice to assume the magnetic field to be two-dimensional, independent of the coordinate parallel to the shaft of the machine. The field analysis is performed over the cross-section of the machine, which is in a plane perpendicular to the shaft.

As for the core losses, a conventional 2D finite element computation of the magnetic field in an electric machine neglects the core loss effects. The negligence of the eddy-current loss comes naturally, because the iron core is laminated and the currents flowing along the laminations are not compatible with 2D analysis. The hysteresis loss is excluded from the analysis by replacing a multi-valued hysteretic relationship of the iron core with a single-valued function. Overall, this means that the iron sheets are assumed to be made from nonhysteretic, nonlinear material with zero conductivity. The losses in the iron core of the machine are not taken into account when solving the magnetic field, which means that the damping response caused by these losses is missing from the analysis. These simplifications limit the application of conventional methods to the computation of the core losses. The core loss calculation is performed using empirical or semi-empirical formulae, after the magnetic flux density distribution has been determined. Even if the formulae for predicting the iron loss

were accurate, the obvious error is already present in the exclusion of the iron loss from the field computation.

In order to accurately estimate the core losses, the hysteresis branching has to be modelled instead of single-valued functions (Nakata, 1998). In general, it is a problem of combining FEM with hysteresis modelling. This is a very complex task that has only recently become solvable, primarily owing to the growth of computer capacities and the development of methods combining accurate hysteresis models with suitable finite element field formulations in the frame of robust iterative techniques, which are able to handle the hysteretic nonlinearities efficiently.

In the following sections of the introduction, the two above-mentioned approaches of the core loss computation come under closer scrutiny. In the frame of the conventional approach, the FEM methodology is taken for granted (Silvester and Ferrari, 1991). Section 1.2 focuses on empirical formulae, where their evolution, state-of-the-art and applications are briefly outlined. Section 1.3 introduces the necessary items of the hysteresis incorporation in the finite element magnetic field analysis, namely a hysteresis model and an iterative technique, which creates an important interface between the hysteresis model and a finite element field formulation. This overview is followed by a literature review concerning the inclusion of hysteresis into finite element field analysis.

1.2 Evolution in brief and state-of-the-art of empirical formulae

1.2.1 Core loss separation

According to the statistical theory (Bertotti, 1988), the average power loss per unite volume in soft magnetic materials consists of the sum of the hysteresis, classical and excess loss contributions

$$p^{\text{core}} = p^{\text{hys}} + p^{\text{class}} + p^{\text{exc}} \tag{1.1}$$

The hysteresis loss originates from the discontinuous character of the magnetization process (localized irreversible changes) on a very microscopic scale. The hysteresis loss is equal to the area of the quasi-static hysteresis loop times the magnetizing frequency. The classical eddy-current loss is associated with the material macroscopic large-scale behavior, where the

presence of magnetic domains is disregarded, the magnetization process is assumed to be perfectly homogeneous in space and in the range of magnetizing frequencies where the skin effect is negligible. The excess loss is caused by the domain wall motion, which generates local eddy currents in the vicinity of the moving walls, and by the wall interaction with inhomogenities of the lattice.

In particular, the empirical and analytical formulae associated with these three contributions depend on the nature of the flux density variation. In rotating electric machines, owing to slotting and saturation, and owing to the harmonic contents of the voltage supply in the case of inverter supply, the magnetic flux density may be significantly distorted from the ideal sinusoidal variation. In addition, in some parts of the machine the magnetic flux density becomes rotational rather then alternating.

1.2.2 Alternating losses

For a long time, the core losses in rotating electric machines have been computed using the alternating core loss models. This was mainly because of the lack of data associated with the rotational core losses and the lack of appropriate models. The computation of alternating core losses is essentially based on the statistical theory of Bertotti (1988) and Fiorillo and Novikov (1990a, 1990b). In all the papers discussed below, FEM was used to compute the flux density distribution.

One-term formulae (total specific loss) and two-term formulae (hysteresis and eddy-current loss) together with different distortion and correction factors to account for distorted flux density waveforms and possibly minor hysteresis loops have been used, for instance, by Jamil and Demerdash (1990), Smith and Phipson (1991), Jamil et al. (1992), Akbaba and Fakhro (1992), Arkkio and Niemenmaa (1992) and Saari and Arkkio (1994).

A three-term formula has been used by Atallah et al. (1992), who also employed an expression for the distorted excess loss and predicted the core loss in a radial-field brushless DC motor under different operating modes. However, the rotational effects were disregarded; instead, the losses were computed from the contributions obtained for each of the two equivalent orthogonal alternating flux density components. This loss computation approach was adopted by Flack and Williamson (1996), who investigated the possibility of using the magnetic slot wedges to reduce the core loss in cage induction motors, and by McClay et al.

(1996), who proposed a reduced finite element model to calculate the rotor core loss in an induction motor. The influence of the stator frame design on the no-load losses in large cage induction motors was studied by Smith et al. (1996) and Ferreira da Luz et al. (2000) computed the core losses and investigated the effect of different slot openings on the core loss in a non-skewed induction motor.

1.2.3 Rotational losses

The iron loss associated with the angle of lag between the magnetic field $\boldsymbol{H}$ and magnetic flux density $\boldsymbol{B}$ is called the rotational power loss. According to Moses (1990), this loss is at least as important as the alternating one and it can account for 50% of the loss in a rotating machine stator core. At low and medium flux density levels, the rotational loss may be three times higher than the loss measured at the same alternating flux density level. The anisotropy increases the rotational loss; thus, the more isotropic the material is the lower the rotational loss, when compared to the analogous loss under alternating magnetization (Moses, 1990). The rotational power loss occurs in the regions of electromagnetic devices, where the flux direction varies in the plane of laminations. In rotating electrical machines these regions are at the roots of the stator teeth and all along the yoke of the stator. Concerning induction machines, the rotational loss also occurs to a certain extent in the rotors, owing to the difference between the rotational speeds of the rotor and the field of the stator. Similarly to the alternating loss, the rotational loss can also be separated into rotational hysteresis, classical and excess losses (Fiorillo and Rietto, 1990; Zhu and Ramsden, 1998)

In respect of the loss measurements under 50 Hz sinusoidal alternating flux and purely rotating flux, which have been performed by Fiorillo and Rietto (1990) in nonoriented SiFe laminations, Bertotti et al. (1991) used the experimental ratio between circular and alternating hysteresis loss components as a function of the peak flux density. The experiments indicated that this ratio is a monotonically decreasing function of the peak flux density and it is fairly independent of the type of lamination and always lower than 1 above 1.5 T. Hysteresis rotational loss under distorted elliptical flux was computed using a linear interpolation between alternating and purely rotational hysteresis loss. Rotational classical loss was estimated through the analytical two-dimensional formula, and the same formula was also used to estimate the rotational excess loss. The core loss of an induction motor was calculated

with the results 20% lower than the measured ones. Bertotti et al. (1994) also introduced a separate formula for the rotational excess loss, which involved the ratio between the circular and alternating sinusoidal excess loss. This ratio is independent of frequency and its dependence on the peak flux density is similar to the one associated with the hysteresis loss. The computed loss for an induction motor with a slotless rotor was compared with the one provided by the conventional model, where the flux density is assumed to be unidirectional and sinusoidal. A considerable difference between the loss values estimated by the two models was obtained in the regions where the flux is essentially two dimensional. However, the differences were not so remarkable for the losses computed over the whole stator core.

Zhu et al. (1992) calculated the core losses in a permanent magnet motor by using the three-term formula (Atallah et al., 1992), into which the rotational effects of the classical and excess losses were included. However, the rotational hysteresis was replaced by alternating because of the lack of data, and the calculated loss was about 20% less than the measured one. Zhu and Ramsden (1993a) continued the research on the rotational hysteresis loss with measurements using a square specimen testing system (Zhu and Ramsden, 1993b), where the total loss was separated into appropriate rotational components (1.1) and the corresponding coefficients have been worked out for the particular loss calculation. The error of 20% from the previous paper has now been reduced to 10%; however, since the hysteresis loss under elliptical flux was estimated by using a linear interpolation between alternating and circular hysteresis losses, it was only a rough estimate. Therefore, Zhu et al. (1994) introduced a quadratic interpolation and Zhu et al. (1995), based on their own measurements as well as some other researchers' (Cecchetti et al., 1978) measurements, proposed a model for the circular hysteresis loss, which made use of the similarity between a curve of the circular hysteresis loss versus peak flux density and a torque/slip curve of a single-phase induction machine. The application of this new model (Zhu and Ramsden 1995, 1998) produced an error of 13%. The model has also been adopted by Štumberger et al. (2000), who analyzed an interior permanent magnet synchronous motor in steady-state under different loads, supply conditions and speeds.

There are many papers in which the basic core loss formulae are modified and adjusted for various types of electrical machines and for different types of nonsinusoidal excitation. For switched reluctance motors, refer for instance, to Hayashi and Miller (1995). As for the

permanent magnet motors, reference can be made to Slemon and Liu (1990). For the losses in a DC bias field see, e.g. Köfler (1990). The approach for the core loss computation of an induction motor supplied from a current source inverter has been reported by Klug and Ibrahim (1987). How the core loss formulae are treated under PWM voltage excitation conditions can be found, for example, in a series of papers by Amar et al. (1994), Amar and Kaczmarek (1995) and Kaczmarek et al. (1996). An interesting contribution to the iron loss evaluation in electrical machines was presented by Amin (1995), who proposed a simple formulation, similar to that used for the evaluation of the copper loss.

1.3 Magnetic field analysis taking the hysteresis into account

The inclusion of hysteresis in the 2D field analysis is a complex task that requires consideration of several relatively separate problems.

Firstly, taking hysteresis into account requires an accurate hysteresis model. From the electromagnetic design and analysis point of view, the hysteresis model should be computationally efficient and capable of describing hysteresis phenomena in ferromagnetic materials as accurately as possible from the macroscopic behavior perspective. The detailed explanation of microscopic processes does not have a superior importance. In particular, the Preisach hysteresis model appears to be the most suitable choice. It is also the most used hysteresis model (Bottauscio et al., 1999) and it has been chosen in this work as well.

However, zero dimensional hysteresis modeling is not appropriate for geometrically complicated systems, such as an electric machine. Therefore, a hysteresis model has to be coupled with the appropriate Maxwell equations, which would then provide a complete description of a magnetic field problem from a macroscopic point of view. Furthermore, the magnetic field equations should be combined with the circuit equations of a feeding electrical network and a motion equation of the rotor. All these equations create a system of equations that should be solved simultaneously.

Ultimately, since FEM is used to solve the field equations, the hysteresis model has to be combined with FEM field formulation. The link between the hysteresis model and finite elements is provided by a nonlinear iterative scheme, capable of handling hysteretic characteristics. The Fixed-Point technique (FPT) has proven to have certain advantages over

other methods, when complicated hysteretic relationships are considered (Saitz, 1999a, 1999b).

To sum up, in order to consider hysteresis in magnetic field analysis, firstly, an accurate hysteresis model, and, secondly, an efficient procedure for handling hysteretic nonlinearities associated with the incorporation of a hysteresis model into a finite element scheme are needed. In this respect, the Preisach hysteresis model and the Fixed-Point technique have been chosen in this work, and they are briefly reported in the following, together with the reasoning supporting these choices. After that, a literature review concerning the magnetic field computation taking the hysteresis into account is given.

1.3.1 Preisach hysteresis model

Many different hysteresis models have been proposed over the years. A comprehensive review of available hysteresis models is given by Iványi (1997). The Preisach model of hysteresis (Mayergoyz, 1991) seems to be the most common choice (Bottauscio et al., 1999) in many different applications. Owing to its ability to provide relatively accurate predictions, and its efficiency and robustness, the Preisach model is a prevailing hysteresis model in the area of magnetic field analysis.

Another common hysteresis model is the Jiles-Atherton model (Jiles and Atherton, 1984; Jiles, 1994), which, in terms of the occurrence in applications takes the second place, but well after the Preisach model (Bottauscio et al., 1999).

The Jiles-Atherton model is a physical model for ferromagnetic hysteresis based on the energy balance exposed in a magnetic material. In this model, the energy supplied to a material is equal to the sum of the stored magnetostatic energy and the energy dissipated through the domain wall movement when overcoming the hindrance of microscopic imperfections in the material, resulting in the hysteresis loss. In the case of no hysteresis loss, the stored energy is equal to the supplied energy and the magnetization follows the anhysteretic curve.

A comparison of the Jiles-Atherton and the Preisach hysteresis models in magnetodynamics was presented by Philips et al. (1995). According to their findings, the correspondence with measurements is generally better for the Preisach model than for the Jiles-Atherton one. The identification of parameters in the Preisach model requires relatively

extensive measurements, but hardly any fitting. The opposite is true for the Jiles-Atherton model. Furthermore, Philips et al. (1995) concluded that the effort required for implementing and running the models was about the same for both the models regarding their classical versions. However, the generalized Preisach model (Bertotti, 1992) required considerably more effort than the generalized Jiles-Atherton model (Jiles, 1994).

The following provides a brief description of the Preisach model and one of its vector versions. For detailed information about the Preisach model, its properties, variations and different extensions, refer to Mayergoyz (1991), Bergqvist (1994) or Iványi (1997).

Classical Preisach model

The Preisach model is a phenomenological model of hysteresis that was originally proposed in 1935 by F. Z. Preisach. Since then many variations of Preisach models have appeared. The basis for all Preisach-type models is the classical Preisach model (CPM).

Philips et al. (1994a) demonstrated that, under static conditions, there is a reasonable agreement between CPM and measurements, at least for silicon iron. CPM is frequency-independent and it cannot account for the frequency dependence of hysteresis effects. In order to include the frequency dependence in hysteresis modeling, a dynamic scalar Preisach model of hysteresis was suggested by Bertotti (1992). For comparison between the static and dynamic Preisach models in magnetodynamic field computation, see for example, Philips et al. (1994a), or Rouve et al. (1996).

According to the Preisach theory, the magnetization M is determined as a superposition of elementary hysteresis operators (EHOs). EHO, denoted as $\hat{\gamma}(h_\mathrm{a}, h_\mathrm{b})$ with h_a and h_b being the "up" and "down" switching fields, acts on the applied magnetic field H, giving the output value according to the current value of H as well as its past history. If H is smaller than h_b, the value of $\hat{\gamma}(h_\mathrm{a}, h_\mathrm{b})H$ is –1. If H is greater than h_a, the value of $\hat{\gamma}(h_\mathrm{a}, h_\mathrm{b})H$ equals +1. Finally, if H lies between h_b and h_a, the value of $\hat{\gamma}(h_\mathrm{a}, h_\mathrm{b})H$ does not change. EHO is defined only for $h_\mathrm{a} \geq h_\mathrm{b}$. The definition of the classical Preisach model reads

$$M = \iint_{h_\mathrm{a} \geq h_\mathrm{b}} \mu^\mathrm{s}(h_\mathrm{a}, h_\mathrm{b}) \hat{\gamma}(h_\mathrm{a}, h_\mathrm{b}) H \,\mathrm{d}\, h_\mathrm{a} \,\mathrm{d}\, h_\mathrm{b} \tag{1.2}$$

where $\mu^{\mathrm{s}}(h_{\mathrm{a}}, h_{\mathrm{b}})$ is the Preisach (distribution) function, representing the distribution EHOs.

Vector Preisach model (VPM)

A scalar hysteresis can be considered to be a special case of vector hysteresis, in which the magnetic field is restricted to vary along one fixed direction. In such a case, a scalar hysteresis model can be employed. However, if the assumption of variation along the fixed direction is not applicable (rotating electric machines), the hysteretic relation has to be handled by using a vector hysteresis model. To account for the vector hysteresis, the Preisach model has been generalized by Mayergoyz (1991).

The classical vector Preisach model is defined as a superposition of scalar Preisach models continuously distributed along all possible angular directions. In the two-dimensional case, the magnetization $\boldsymbol{M}$ is computed from

$$\boldsymbol{M} = \int_{-\frac{\pi}{2}}^{\frac{\pi}{2}} \boldsymbol{e}_{\varphi} \left(\iint_{h_{\mathrm{a}} \geq h_{\mathrm{b}}} \mu^{\mathrm{v}}(h_{\mathrm{a}}, h_{\mathrm{b}}, \varphi) \hat{\gamma}(h_{\mathrm{a}}, h_{\mathrm{b}}) H_{\varphi} \, \mathrm{d}\, h_{\mathrm{a}} \, \mathrm{d}\, h_{\mathrm{b}} \right) \mathrm{d}\varphi \tag{1.3}$$

where $\boldsymbol{e}_{\varphi}$ is a unit vector along the direction given by the polar angle φ, $\mu^{\mathrm{v}}(h_{\mathrm{a}}, h_{\mathrm{b}}, \varphi)$ is the vector distribution function, and

$$H_{\varphi} = \boldsymbol{H} \cdot \boldsymbol{e}_{\varphi} \tag{1.4}$$

is the geometric projection of $\boldsymbol{H}$ in the direction of $\boldsymbol{e}_{\varphi}$. Since the distribution function $\mu^{\mathrm{v}}(h_{\mathrm{a}}, h_{\mathrm{b}}, \varphi)$ is sensitive to the selected direction, that is, it depends on the direction angle φ, the expression (1.3) introduces an anisotropic vector Preisach model. If the distribution function is selected to be identical along any direction, that is, independent of the direction angle φ, it reduces to $\mu^{\mathrm{v}}(h_{\mathrm{a}}, h_{\mathrm{b}})$ and the resulting vector hysteresis model is considered isotropic.

Identification of the Preisach model

The Preisach model is a phenomenological hysteresis model. In order to use such a model in practical applications, the model must be related to a particular material, the hysteretic behaviour of which is intended to be modelled. This link between the model and the real material is accomplished in the Preisach model through the distribution function. Experimental determination of the distribution function, which in turn means fitting the model to some experimental data, is called the identification of a hysteresis model. The identification procedure as performed in this work is described in detail in Chapter 2.

1.3.2 Fixed-Point technique

The Fixed-Point technique (FPT) has been proposed in magnetics by Hantila (1975). The technique splits the particular nonlinear function into a linear part and a variable nonlinear residual, which has to be determined through an iterative process.

The Fixed-Point technique seems to be the most widely used numerical scheme for handling the hysteretic nonlinearities (Bottauscio et al., 1999; Saitz, 1999a). Two versions of the Fixed-Point scheme can be identified: B-version (B-FPT) and H-version (H-FPT). In addition, some other Fixed-Point-based methods have been reported in the literature, which retain the basic Fixed-Point feature of splitting the nonlinear function, but the coefficients used do not guarantee the best convergence.

The analysis of major iterative schemes connected with the classical Preisach model on a test application (Saitz, 1999a, 1999b) unveils their possibilities, advantages and drawbacks. A combined Fixed-Point Newton-Raphson procedure (NRM) is found to be particularly fast, but in some cases it may become unstable. The implementation difficulties for NRM are greater than for Fixed-Point-based techniques. FPT is robust with sure convergence from any starting value, but usually relatively slow owing to its linear convergence rate (Chiampi et al., 1980, 1994a, 1994b; Mayergoyz, 1982; Ionita, 1991a; Ionita et al., 1996). If a nonlinear function is monotonous and its first derivative is continuos, the Newton-Raphson iteration is unconditionally stable (Silvester and Ferrari, 1991). A numerical optimization method for correcting the material data in order to improve the convergence of the Newton-Raphson algorithm was proposed by Pahner et al. (1998). FPT does not impose constraints on the smoothness of nonlinear curves, thus allowing their rough definition and even the presence of inflection points. If FPT is involved, a simple piecewise linear approximation is adequate to

model the nonlinear curves (Chiampi et al., 1995). For the purpose of this research, the robustness and reliability are preferred to the speed, and therefore FPT has been chosen for the implementation.

Using FPT following its B-version, a nonlinear function $\mathcal{H}^{\nu}$ of the magnetic flux density $\boldsymbol{B}$ is split into two parts

$$\mathcal{H}^{\nu}(\boldsymbol{B}) = \nu_{\mathrm{FP}}\boldsymbol{B} + \boldsymbol{R}_{\mathrm{FP}} \tag{1.5}$$

where ν_{FP} is the Fixed-Point coefficient and $\boldsymbol{R}_{\mathrm{FP}}$ is the Fixed-Point residual, which is computed iteratively. It is possible to show (Hantila, 1974) that the best convergence is achieved if ν_{FP} is chosen within an interval around the average between maximum $\nu_{\max}$ and minimum $\nu_{\min}$ slopes of a particular nonlinear curve

$$\nu_{\mathrm{FP}} = \frac{\nu_{\max} + \nu_{\min}}{2} \tag{1.6}$$

The iterative algorithm of FPT is illustrated in a nonlinear magnetostatic problem formulated in terms of the magnetic vector potential $\boldsymbol{A}$ and represented by

$$\nabla \times \mathcal{H}^{\nu}(\nabla \times \boldsymbol{A}) = \boldsymbol{J} \tag{1.7}$$

where $\boldsymbol{J}$ is the current density. Applying FPT and substituting (1.5) into (1.7), the nonlinear problem (1.7) reduces to a succession of linearized problems having the form

$$\nu_{\mathrm{FP}} \nabla \times \nabla \times \boldsymbol{A}^{k} = \boldsymbol{J} - \nabla \times \boldsymbol{R}_{\mathrm{FP}}^{k\text{-}1} \tag{1.8}$$

where k denotes the iteration step. The solution of this equation provides the unknown magnetic vector potential $\boldsymbol{A}^{k}$, provided of course that the residual $\boldsymbol{R}_{\mathrm{FP}}^{k\text{-}1}$ is known (in the beginning some initial guess $\boldsymbol{R}_{\mathrm{FP}}^{0}$ is assumed). From the calculated $\boldsymbol{A}^{k}$, the flux density $\boldsymbol{B}^{k}$ is evaluated and then the residual nonlinearity

$$\boldsymbol{R}_{\mathrm{FP}}^{k} = \mathcal{H}^{\mathrm{v}}\left(\boldsymbol{B}^{k}\right) - \nu_{\mathrm{FP}}\boldsymbol{B}^{k} \tag{1.9}$$

is computed. After that, the second term on the right-hand side of (1.8) is updated, replacing $\boldsymbol{R}_{\mathrm{FP}}^{k\text{-}1}$ with $\boldsymbol{R}_{\mathrm{FP}}^{k}$ and the procedure is repeated until a convergence limit is satisfied.

From the graphical representation point of view, every nonlinear iterative scheme replaces the nonlinear curve with a straight line. Regarding FPT, the slope of the substituting line is fixed, since ν_{FP} is kept constant during the iterative process. This is unlike the Newton-Raphson scheme, where the local slope of the linearized characteristic is updated in each iteration step. In FPT, the slope never changes and the straight line is only vertically shifted as the iteration proceeds. Consequently, in applying FEM, the finite element stiffness matrix is never modified, which in turn means that the computational process is accelerated.

1.3.3 Literature review

One of the first papers dealing with the inclusion of hysteresis in the numerical magnetic field analysis appears to be the contribution published by Del Vecchio (1980). He incorporated a scalar Preisach model in the 1D diffusion equation and applied the finite difference method for space discretization. Del Vecchio (1982) extended the previous approach to the 2D FEM analysis of the diffusion equation over the cross-section of an infinitely long rectangular bar carrying sinusoidal flux.

Since then, an abundance of papers on the subject of hysteresis incorporation in FEM have appeared in the literature. In general, the studied 2D problems can be classified into two basic categories: current- (voltage-) driven problems (analysis of electrical devices) and flux-driven problems. As for current- (voltage-) driven problems, the field analysis is performed in a plane perpendicular to the flow of the current (electric machines, transformers). Flux-driven problems essentially refer to the 2D lamination analysis, which can be tolerably reduced to the 1D analysis, if the ratio between lamination width and thickness is greater than five (Bottauscio et al., 2000a).

Since the research carried out in this thesis is associated with the analysis of electrical devices, the survey presented below concentrates on current- (voltage-) driven problems. For a detailed literature review concerning flux-driven problems refer to Saitz (1999a).

A short reference to flux-driven problems

The Newton-Raphson method has been used in connection with a Preisach model in a 2D lamination analysis by Boucetta et al. (1994) and Rouve et al. (1996). A method similar to the simple iteration combined with a Preisach model in a 1D lamination analysis has been reported by Philips et al. (1994a, 1994b), Gyselinck et al. (1996, 1998) and Dupré et al. (1997a, 1997b, 1998b, 1998d). A technique for time-periodic flux-driven problems has been proposed by Appino et al. (1996) and used by Bottauscio et al. (1996) and Boglietti et al. (1996) in combination with a Preisach model and B-FPT or H-FPT (Boglietti et al., 1998). Dupré et al. (1998c, 1999) compared the two different numerical procedures, described by Boglietti et al. (1998) and e.g. Dupré et al. (1998b), both involving a dynamic Preisach model (Bertotti, 1992) and intended for the magnetic field analysis of laminations subject to a time-periodic flux excitation.

Among other papers dealing with 1D or 2D lamination problems with hysteresis, contributions from Naidu (1991), Miano et al. (1995), Gourdin et al. (1998), Raulet and Masson (1998), Tellinen (1998) or Machado and Ribeiro (1998) could be of interest.

Current- (voltage-) driven problems

Féliachi and Meunier (1985) and Ossart and Meunier (1991) studied a magnetic recording problem in storage media by applying 2D FEM magnetostatic analysis with a Fixed-Point-based technique and an astroid hysteresis model.

The idea of using VPM in computations of magnetostatic fields in media with hysteresis was first realized by Friedman and Mayergoyz (1989). They used an integral equation approach for the solution of a 2D magnetostatic problem. The approach has been extended by Adly et al. (1993), where a 3D generalization of VPM (Adly and Mayergoyz, 1993) was employed to simulate some magnetic recording processes.

Ionita (1991a) theoretically dealt with H-FPT and applied it to study a dynamic hysteretic problem of permanent magnet magnetization (Ionita, 1991b).

Henrotte et al. (1992) combined a scalar Preisach model applied in the reversed fashion and NRM to analyze a 2D magnetic circuit including an air gap and supplied by time-dependent currents. The authors reported difficulties connected with the convergence of NRM. The same computational algorithm was applied by Philips and Delincé (1993) for the

computation of *B-H* trajectories in the torus. The track of this research was continued by Delincé et al. (1994), who combined the field analysis with the circuit equations to study a ferromagnetic core that coupled the primary and secondary coils. This paper clearly indicated the influence of hysteresis on current and voltage waveforms in inductors and concluded that the computations that are performed only with single-valued nonlinearities are unable to correctly predict the actual behavior of such devices.

Bergqvist et al. (1993) adopted the approach of Henrotte et al. (1992) to express the constitutive law, but the quantities involved were defined in a slightly different manner. A VPM was employed and the field was computed in a 2D magnetic circuit used in a magnetostrictive device. The influence of an electric circuit was accounted for by adding a circuit equation. The nonlinear algebraic equations were solved by the simple iteration with a relaxation factor. Bergqvist (1994) continued the previous work by employing a lag hysteresis model. A NRM iteration formulation was derived to solve the obtained nonlinear system of equations. An application to a simple current-excited 2D magnetic circuit was reported.

Some further research concerning NRM and problems involving scalar hysteresis (scalar Preisach model) has been conducted, for example, by Leonard et al. (1995) and Ninet et al. (1996, 1998).

Kurz et al. (1993) proposed an iterative process formulated in terms of $\boldsymbol{M}$ and $\boldsymbol{H}$ variables, and combined it with a VPM and 2D time-stepping FEM. Several examples of relatively simple current-driven magnetic circuits were computed and compared with analytical solutions showing good accuracy. Fetzer et al. (2000) adopted the iteration scheme proposed by Kurz et al. (1993) and studied a 3D magnetic field problem of a ferromagnetic sphere immersed in a time-varying uniform field. The same iteration has also been used by Amor et al. (2000), who combined a Preisach model and 2D FEM for a cylindrical ferromagnetic sample surrounded by a coil inductor and studied the influence of a relaxation coefficient on the iterative scheme convergence.

Alotto et al. (1994) incorporated a scalar Preisach model and a VPM in 2D magnetostatic finite element analysis. The resulting system was solved by a Fixed-Point-based iterative technique. To test a vector model, a particular geometry was adopted, in which the hysteretic material was surrounded by a double ferromagnetic nonlinear yoke, which was supplied by two systems of coils with orthogonal magnetic axes. Along with this simple

geometry, a more complex problem, consisting of the simplified structure of a stepping motor, was also analyzed.

Bottauscio et al. (1995) presented a method specially prepared for time-periodic magnetic field problems driven by current. The method features a coupling of a Preisach model with a finite element solution, formulated in terms of the magnetic vector potential. The B-version of FPT is used to solve the nonlinear hysteretic system. The Preisach model is applied in the reversed fashion through a secant method coupled with a backup bisection procedure. In each iteration step, the solution for all the time samples is computed to provide the instantaneous variation of the magnetic vector potential. From this variation, the periodic evolution of the magnetic flux density in each element is obtained and, through the hysteresis model, the symmetric hysteresis cycle is determined. Subsequently, the time variation of the Fixed-Point residual is evaluated. The proposed method was applied to a 1D problem of infinite ferromagnetic hollow cylinder. The same technique but with the Jiles-Atherton model was reported by Chiampi et al. (1995) and with H-FPT by Bottauscio et al. (1998), who combined a VPM and 2D FEM to study a 4-pole configuration, energized by two independent sinusoidal currents with phases in quadrature, allowing an elliptical flux to be produced. Toms et al. (2001) extended the approach presented by Chiampi et al. (1995) to a general 2D case with scalar hysteresis.

Ionita et at. (1996b) proposed a hysteresis model based on CPM and completed it with new rules to describe vector dynamic hysteresis. The model was combined with B-FPT and incorporated into 2D magnetic field formulation in terms of the magnetic vector potential, which was time-stepped by using the Crank-Nicholson scheme and applied to analyze an impulse magnetizer.

Dupré et al. (1997a) prepared a 2D FEM model of a single-tooth region of an induction motor and connected it to a VPM. The fluxes through the boundary parts were obtained from the local measurements in the motor and imposed by proper boundary conditions. The computed field patterns in the tooth model served to derive the local excitation conditions for the second-level magnetodynamic lamination model. This model comprised a 1D lamination analysis in two directions, allowing the rotational effects to be taken into account. A reasonable agreement was found between the global machine losses obtained by the combined tooth region-lamination model and the measured losses.

Dupré et al. (1998a) utilized the differential permeability to facilitate the inclusion of the vector hysteresis in the finite element scalar and vector magnetic potential formulation for magnetostatic problems. The governing equations were rewritten in terms of the partial time derivatives of $\boldsymbol{H}$ and $\boldsymbol{B}$. Thus, the static equations became time-dependent (ordinary differential equations) and the Crank-Nicholson time-stepping scheme was employed to solve them. In each time step the nonlinear system is solved by an iterative technique involving the differential permeability. A VPM, introduced through the differential permeability tensor, takes care of the material hysteretic behavior. The developed numerical technique was applied to a T-joint region of a three-phase inductor with rotating flux excitation and with the inclusion of eddy currents by means of an additional conductivity matrix (Gyselinck et al., 1999b) to the no-load simulation of a voltage-supplied three-phase transformer core (Gyselinck et al., 1999a).

Deblecker et al. (1998) presented an algorithm for 2D magnetodynamic problems with hysteresis based on the transmission-line modeling technique, and Kim et al. (1998a) employed a VPM (Hong et al., 1994, 1995), FEM and a Fixed-Point-based technique to analyze the magnetic field in a hysteresis motor.

Lee et al. (1998) and Lee and Hyun (2000) analyzed a synchronous reluctance motor using 2D FEM time-stepping included in a vector control scheme (Kim et al., 1998b). The hysteresis was incorporated through a Preisach model applied independently for two orthogonal components of the magnetic field. A Fixed-Point-based technique handled the nonlinear system. The field equations were combined with circuit equations and a PWM voltage supply was considered. The same computational methodology but with a current supply was applied for a permanent magnet assisted synchronous reluctance motor by Lee and Hyun (1999).

Bottauscio et al. (2000a) modified a technique for periodic supply conditions developed earlier (Bottauscio et al., 1995; Bottauscio et al., 1998), writing the linearized problem in the frequency domain by introducing a truncated Fourier series. Thus, in each 2D FEM iteration step (H-FPT), the computation of the field solution for the considered harmonic components and the update of the residual are required. An inverse fast Fourier transform is used to obtain the time dependence of the flux density and magnetic field; the latter serves as in input to a dynamic Preisach model. Then, the time variation of the Fixed-Point residual is obtained and the harmonic spectrum of it is evaluated by a fast Fourier transform. A coupling between the

field and circuit equations enabled a voltage-driven solution of the field problem. The method has been applied to the analysis of an Epstein frame and an eccentric toroidal core, fitted with a number of localized pick-up coils, enabling to follow hysteresis branching in different parts of the core. As a conclusion, the authors stated that introducing the magnetic hysteresis in core modeling considerably improved the accuracy of the numerical computation.

In order to include eddy currents in the 2D FEM analysis, Bottauscio et al. (2000b) extended their previous study (Bottauscio et at., 2000a) with the 1D lamination model (e.g. Boglietti et al., 1998). In each 2D FEM iteration step (B-FPT), the solution provides the waveform of the flux density in each element of the mesh. This waveform is then used as an input to a 1D lamination flux-driven problem, comprising the classical or dynamic Preisach model, and solved by means of H-FPT. The solution to the 1D problem provides the time variation of the magnetic field intensity, which is used to update the Fixed-Point residual in the 2D Fixed-Point iterative scheme. The method has been applied to a toroid constituted from a single sheet and an eccentric toroid, as described in the previous paragraph. Based on the numerous results presented in the paper, the authors concluded that the eddy-current effects are important in the simulation of the behavior of laminated cores with negligible air gaps. However, their effect decreases with the supply frequency; local quantities are affected by the material modeling and a significant improvement is obtained considering the hysteresis of the magnetic material. Regarding the method of analysis, the authors observed a significant increase in the processing time by inclusion of eddy currents.

Gyselinck et al. (2000) incorporated the hysteresis and eddy-current losses in a 2D FEM time-stepping no-load analysis of an induction motor. The hysteresis was modeled by a vector Preisach model inverted by means of NRM. The authors observed fast convergence and stated that the relaxation of the iteration scheme had been rarely required. The eddy-current losses were accounted for by introducing an additional conductivity matrix into finite element equations (Gyselinck et al., 1999a, 1999b), neglecting the skin effect in the laminations. The field equations were combined with circuit equations and a sinusoidal voltage supply was considered. The resulting nonlinear system of equations was solved by NRM. Comparisons between computed and measured stator phase currents as well as computed loci of hysteresis loops in different parts of the motor were reported. The total computed core losses were about 10% smaller than the measured ones. The proposed method has been reported to be

computationally very expensive, when compared to the analysis with a single-valued *B-H* curve.

Inclusion of other core loss components into 2D FEM

As mentioned earlier, the explicit inclusion of the classical eddy-current losses in 2D field analysis is impossible. In order to model them explicitly, a very expensive 3D analysis is required (Dular et al., 1998). However, the eddy-currents can be directly included in a 2D field analysis, with certain limitations, by introducing an additional conductivity matrix into the finite element equations, as proposed by Gyselinck et al. (1999a, 1999b, 2000). Another possibility is the combination of 2D analysis with 1D lamination modeling (Bottauscio et al., 2000b). The excess loss can be included by adopting a dynamic hysteresis model (Bertotti, 1992).

Application of a hysteresis model a posteriori

Another possibility of computing the core losses from the known variation of the flux density is to use some hysteresis model a posteriori. This approach means that the flux density distribution is determined in a conventional way (2D FEM with a single-valued function) and afterwards this computed variation serves as an input to a hysteresis model or, in a more advanced case, to a lamination model, in which the eddy currents and hysteresis are included. Such an approach was presented, for instance, by Nee and Nipp (1994), where the core loss was evaluated by using a combination of the Jiles-Atherton hysteresis model, Rayleigh theory and empirical expressions, Jayaraman and Strangas (1994), where the Jiles-Atherton hysteresis model and a 1D FEM model of a transformer limb were used to estimate the hysteresis and eddy-current losses, or Gyselinck et al. (1996, 1998), who employed a 1D FEM lamination model (Philips et al., 1994a, 1994b) to calculate the core loss in an induction motor.

Summary

The dominance of Preisach-family hysteresis models in magnetic field computations taking the hysteresis into account is undeniable. The hysteretic nonlinearity is mostly handled by Fixed-Point-based techniques. Current-driven problems are found to be the largest application area. They essentially include the 2D field computation of relatively simple geometrical and

supply configurations (simple transformer-like and rotating machine-like structures). However, in the last 2-3 years, the application areas have been slowly shifted from rather simple current-driven problems into complete voltage-driven simulations of ferromagnetic cores and rotating machines.

1.4 Objectives, scope and novelty of the presented work

The main purpose of this work is to develop and implement a method for finite element modeling of the magnetic field in a rotating electric machine, taking the ferromagnetic hysteresis into account through a vector Preisach model. When calculating the losses of a machine, the time-dependence has to be solved with a general time-stepping method allowing for the real time-variation of the magnetic field. In order to consider the damping effect of hysteresis on this time-variation, the methods to be developed should work within a time-stepping algorithm, and the losses should be taken into account already when solving the magnetic field.

The work consists of two principal tasks. The first task is the actual development and implementation of the method of analysis. This part involves the identification of a scalar hysteresis model by DC-field measurements (Appendix B) on a wound-ring sample (Appendix A), testing the prepared scalar model, identification and testing of a vector hysteresis model, determination of the empirical core loss coefficients by core loss separation measurement on the same wound-ring sample and theoretical development and construction of computational routines with incorporated hysteresis suitable for a field analysis of voltage-driven 2D magnetic circuits.

The next task is to apply the developed methods of analysis to the magnetic field modeling and the core loss evaluation of actual electric machines. Since the developed methods are general, the application to 2D analysis of any electric machine is possible, provided of course that the construction and supply specifications of a particular machine are respected. Primarily for the availability reasons, induction motors have been chosen as the test samples. The methods of analysis have been applied to 30, 37 and 315 kW cage induction motors.

The core losses are determined from the computed field, which includes the effects of hysteresis. The other loss components (classical and excess) are evaluated by using analytical

and empirical formulae. In order to compare the numerically obtained results with the measured ones, an additional task involves the experimental measurements of the core loss on actual induction motors.

Chapter 2 and Chapter 3 deal with the theoretical development and implementation of methods of numerical analysis and measurements. Questions concerning the originality of the material presented in these chapters are important and they are addressed in the following.

Chapter 2 describes the hysteresis model used in the study, which is a Preisach model well known from the literature (for instance Mayergoyz (1991)). The procedure for identification of the scalar model (Section 2.2.1) and the exponential approximation of the magnetization curve close to saturation (Section 2.2.2) are based on the literature (Naidu, 1990; Macfadyen et al., 1973). The presentation, determination of the coefficients, implementation of the formula for the exponential approximation and its combination with the Preisach model are original. The theory of the vector model consisting of angularly distributed scalar models (Section 2.3.1) is well-known from the literature (for instance Mayergoyz (1991)). The idea for identification of the vector model comes from the literature (Gyimóthy and Iványi, 1994). However, the derivation and implementation of the particular formulae associated with the identification of the vector model (Section 2.3.2) have been adjusted to be suitable for the connection with the identification of the scalar model, as used in this work, and therefore they are original.

Chapter 3 describes the incorporation of hysteresis in the field analysis of electric machines. Section 3.1 summarizes the simplifying assumptions. The theory presented in Section 3.2 related to the hysteresis model inclusion in FEM is original. The core loss model, based mainly on the empirical formulae and presented in Section 3.3 is well-known from the literature (for instance Zhu and Ramsden (1998)). The power balance model is original (Section 3.4) with the components computed from the generally well-known formulae (for instance Arkkio (1987)). The numerical computation of the hysteresis torque (Section 3.5.1) is original. The method of the hysteresis torque and core loss measurement on induction motors (Section 3.5.2) has been developed by Dr. Antero Arkkio, who has also performed or supervised the measurements on actual motors and provided the measured data to the author.

The novelty of the thesis is connected with a suitable combination and implementation of the finite element method, Preisach model and Fixed-Point iterative procedure and the

application of these techniques to the field solution and core loss calculation in cage induction motors. This represents a voltage-driven solution in a rotating machine taking the hysteresis into account.

The study is limited to a sinusoidal voltage supply and unskewed motors. The rotor of a motor is forced to rotate at synchronous speed. The rotor cage is assumed to be perfectly short-circuited. Apart from the simplifying assumptions mentioned above, other, say "conventional", simplifications include: a 2D approach with 3D end-region fields modeled approximately by constant end-winding impedances in the circuit equations of the stator winding, negligence of the eddy-current loss in the stator winding, and treatment of the laminated iron core as isotropic, and nonconducting material in the computation of the magnetic field. The simplifying assumptions are discussed in detail in Chapter 3, Section 3.1.

2 Hysteresis model

As discussed in Chapter 1, the hysteresis is modeled in this study by means of a vector Preisach model that consists of angularly distributed scalar Preisach models. The principles of the scalar and vector Preisach models have been summarized in Section 1.3.1. In this chapter, the implementation and distribution function determination of both the scalar and vector models, as performed in this work, are described. First, however, some notations regarding hysteresis models and ***B***-***H*** relation are introduced.

2.1 Hysteresis models and *B*-*H* relation

Expressing the relation between the magnetic flux density ***B*** and magnetic field ***H*** in a hysteretic case requires special attention. If the hysteresis is considered and ***H*** is taken as an independent variable, the value of ***B*** is not uniquely determined by the current value of ***H*** but it also depends on the past history of ***H***. Thus, the function involved is multi-valued and creates hysteresis branches. In practical computations such a hysteretic function is realized by a vector hysteresis model, denoted here by the script $\mathscr{B}^{\mathrm{V}}$

$$\boldsymbol{B} = \mathscr{B}^{\mathrm{V}}\left(\boldsymbol{H}\right) \tag{2.1}$$

This notation implies that the value of ***B*** at a given time depends on the current value of ***H*** and on the whole past history of ***H*** until that instant in time. A configuration of input and output variables represented by the script $\mathscr{B}^{\mathrm{V}}$ is typical for direct application of the Preisach model.

If the input ***H*** varies along one direction only, a scalar model $\mathscr{B}^{\mathrm{S}}$ can be defined

$$B = \mathscr{B}^{\mathrm{S}}\left(H\right) \tag{2.2}$$

expressing the relationship between a scalar input H and a scalar output B, which represent the magnitudes of ***H*** and ***B***, respectively.

Now, choosing $\boldsymbol{B}$ as an independent input variable, the hysteresis models $\mathcal{H}^{\mathrm{v}}$ and $\mathcal{H}^{\mathrm{s}}$, as counterparts of $\mathcal{B}^{\mathrm{v}}$ and $\mathcal{B}^{\mathrm{s}}$, can be introduced

$$\boldsymbol{H} = \mathcal{H}^{\mathrm{v}}\left(\boldsymbol{B}\right) \tag{2.3}$$

$$H = \mathcal{H}^{\mathrm{s}}\left(B\right) \tag{2.4}$$

Since the Preisach model uses $\boldsymbol{H}$ as its input variable, the practical realization of hysteresis models $\mathcal{H}^{\mathrm{v}}$ is not straightforward. One possibility of tackling this problem is to employ such a computational algorithm and iterative scheme that would allow the use of $\boldsymbol{H}$ as an input variable (Dupré, 1998a). Another possibility is the inversion of the Preisach model, which means the application of the model $\mathcal{B}^{\mathrm{v}}$ in the reversed fashion, using $\boldsymbol{B}$ as an input variable. For this purpose, a suitable iterative search should be used. Henrotte et al. (1992) proposed using the Regula Falsi method, Bottauscio et al. (1995) suggested a secant method coupled with a backup bisection procedure, and Gyselinck et al. (2000) employed the Newton-Raphson method. Alternatively, the Preisach model with $\boldsymbol{B}$-input and $\boldsymbol{H}$-output can be realized by using the so-called "inverse distribution function method" used by Takahashi et al. (1998). This allows the identification of the Preisach model so that it is possible to use it directly in the form (2.3), which means that no iterations are needed to get $\boldsymbol{H}$ from $\boldsymbol{B}$ through $\mathcal{B}^{\mathrm{v}}$ in (2.1).

If a vector model $\mathcal{B}^{\mathrm{v}}$ or $\mathcal{H}^{\mathrm{v}}$ consists of angularly distributed scalar models, as is the case in this work, two more hysteretic functions have to be introduced

$$B = \mathcal{B}^{\mathrm{s\text{-}v}}\left(H\right) \tag{2.5}$$

$$H = \mathcal{H}^{\mathrm{s\text{-}v}}\left(B\right) \tag{2.6}$$

The scripts $\mathcal{B}^{\mathrm{s\text{-}v}}$ and $\mathcal{H}^{\mathrm{s\text{-}v}}$ represent scalar models working under a vector model. From the implementation point of view, these models are the same as their pure scalar counterparts $\mathcal{B}^{\mathrm{s}}$ and $\mathcal{H}^{\mathrm{s}}$. The difference lies in the distribution function, which is usually different for $\mathcal{B}^{\mathrm{s\text{-}v}}$ and $\mathcal{H}^{\mathrm{s\text{-}v}}$ from the one for $\mathcal{B}^{\mathrm{s}}$ and $\mathcal{H}^{\mathrm{s}}$.

2.2 Scalar model

The scalar model $\mathscr{H}^{\mathrm{s}}$ used in this work is the classical Preisach model $\mathscr{B}^{\mathrm{s}}$, which is applied in the reversed direction

$$\mathscr{H}^{\mathrm{s}}(B) = \left(\mathscr{B}^{\mathrm{s}}(B)\right)^{-1} \tag{2.7}$$

The inversion of $\mathscr{B}^{\mathrm{s}}$ is realized by a combined bisection-modified Regula Falsi iterative search. In the following, the identification and implementation of $\mathscr{B}^{\mathrm{s}}$ is outlined.

2.2.1 Implementation and identification of the scalar model

The standard identification process for CPM is based on the measurements of the first-order reversal curves. This approach requires a substantial amount of experimental data. Simplified identification procedures that require only a reduced set of measured data were proposed, for example, by Biorci and Pescetti (1958) or Naidu (1990). The latter has been adopted in this work.

The main advantage of the approach proposed by Naidu (1990) is that the measurement of the reversal curves is avoided, because the only requirement to identify the model is the descending (upper) branch of the limiting hysteresis loop, denoted here as $B_{\mathrm{lim}}(H)$ or alternatively as $H_{\mathrm{lim}}(B)$. This function is determined from a DC-field measurement (Appendix B) and is defined by the measured pairs $\left[H_i^{\mathrm{m}}, B_i^{\mathrm{m}}\right]$, where i runs from 1 through the total number of measured points $N_{\mathrm{tot}}^{\mathrm{m}}$, and

$$H_1^{\mathrm{m}} = H_z; \qquad H_{N_{\mathrm{tot}}^{\mathrm{m}}}^{\mathrm{m}} = -H_z \tag{2.8}$$

$$B_1^{\mathrm{m}} = B_z; \qquad B_{N_{\mathrm{tot}}^{\mathrm{m}}}^{\mathrm{m}} = -B_z \tag{2.9}$$

where H_z and B_z denote the values of H and B near the saturation, after which the hysteresis is no longer discernible by practical measurements. The B-H relationship is considered to be hysteretic in between these values, whereas above and below these values the B-H relationship

is modeled by an analytical single-valued function, as described later. The linear interpolation is used to compute the values lying in between the measured points on the limiting curve.

According to Naidu (1990), a distribution function $F(H)$ is defined by the following equations ($H \geq 0$)

$$F(-H) = \sqrt{B_{\lim}(H)} \tag{2.10}$$

$$2F(H)F(-H) = B_{\lim}(H) + B_{\lim}(-H) \tag{2.11}$$

The relation between the distribution functions $F(H)$ and $\mu^{s}(h_a, h_b)$ is fully explained by Naidu (1990) and is omitted here.

Using the distribution function $F(H)$ defined by (2.10) and (2.11), an arbitrary magnetization curve can be determined. For the upward curve from a reversal point (H_R, B_R) holds

$$B^{up}(H) = B_{\lim}(-H) - B_{\lim}(H_R) + B_R + 2F(-H_R)F(H) \qquad H \geq H_R \tag{2.12}$$

and the downward trajectory from a reversal point (H_R, B_R) is given by

$$B^{down}(H) = B_{\lim}(H) + B_{\lim}(-H_R) + B_R - 2F(H_R)F(-H) \qquad H \leq H_R \tag{2.13}$$

The initial magnetization curve $B_i(H)$ is calculated from

$$B_i(H) = \frac{1}{4B_{\lim}(H)}\left(B_{\lim}(H) - B_{\lim}(-H)\right)^2 \tag{2.14}$$

Expressions (2.12)-(2.14) together with the definition of the distribution function (2.10)-(2.11) fully define a scalar hysteresis model $\mathscr{B}^{s}$. It is obvious that the output from the model completely depends on the limiting curve $B_{\lim}$. For different limiting curves, different models are obtained. Therefore, it can be emphasized that the identification of the scalar model, i.e. the identification of the distribution function $F(H)$, in fact means the determination of the limiting curve $B_{\lim}$. As indicated earlier, the limiting curve associated with the scalar model $\mathscr{B}^{s\text{-}v}$

working under a vector model is different from the limiting curve of a pure scalar model $\mathcal{B}^{s}$. To distinguish the two, the limiting curve of a pure scalar model $\mathcal{B}^{s}$ ($\mathcal{H}^{s}$) will be denoted as B_{lim}^{s} (H_{lim}^{s}) and the limiting curve of a scalar model working under a vector model $\mathcal{B}^{s\text{-}v}$ ($\mathcal{H}^{s\text{-}v}$) as $B_{\text{lim}}^{s\text{-}v}$ ($H_{\text{lim}}^{s\text{-}v}$).

2.2.2 Modeling of magnetization curve towards saturation

As previously mentioned, the last point considered on the upper branch of the limiting hysteresis loop B_{lim} is the point after which the hysteresis is no longer discernible by practical measurements, and the coordinates of this point are H_z and B_z (Fig. 2.1 b).

If the magnetic field (flux density) is larger than H_z (B_z), the *B-H* relationship is modelled by a single-valued function B_{sv}, schematically shown in Fig. 2.1 b). Assuming an exponential behaviour of the permeability μ_{sv} (Fig. 2.1 a)

$$\mu_{\text{sv}}(H) = \mu_0 + (\mu_z - \mu_0) e^{-\frac{H-H_z}{H_0}} \tag{2.15}$$

the following expression can be derived for the single-valued function B_{sv}

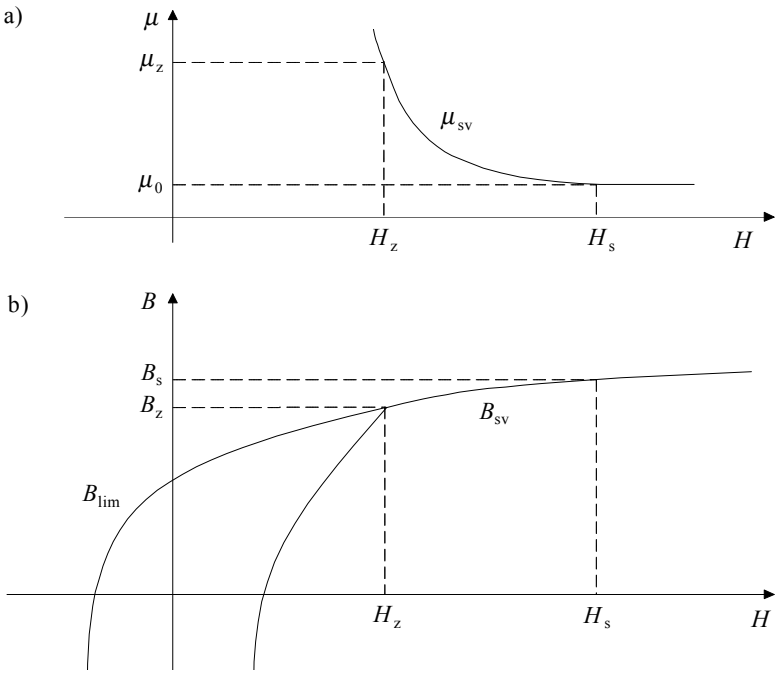

Fig. 2.1. Schematic diagram defining the hysteretic and single-valued parts of the B-H relationship.

$$B_{\mathrm{sv}}(H) = B_z + \mu_0(H - H_z) + (\mu_z - \mu_0) H_0 \left(1 - e^{-\frac{H - H_z}{H_0}} \right) \tag{2.16}$$

Here, μ_z represents the differential permeability defined as the average between the left and right derivatives of the function given by the limiting curve B_{lim} at (H_z, B_z) and ($-H_z$, $-B_z$), respectively. The permeability μ_0 is the permeability of free space and H_0 in (2.16) is computed from

$$H_0 = \frac{B_{\mathrm{s}} - B_{\mathrm{z}} - \mu_0 (H_{\mathrm{s}} - H_{\mathrm{z}})}{\mu_{\mathrm{z}} - \mu_0} \tag{2.17}$$

where H_{s} and B_{s} are the saturation values of the magnetic field and flux density, respectively.

According to Macfadyen et al. (1973), the exponential approximation of the form (2.16) gives satisfactory representation of a magnetization curve over a limited region. The region close to saturation, in which the exponential approximation is used in this work, can be considered to be such a limited region. If, however, the exponential approximation over a wider range, even starting from the origin, is desired, Macfadyen et al. (1973) recommended using a series of terms similar to (2.16).

2.3 Vector model

2.3.1 Implementation of the vector model

The vector model used in this work is the classical vector Preisach model, essentially defined by (1.3), considered in its isotropic form, applied in the reversed fashion and consisting of scalar models distributed along angular directions. In particular, the output $\boldsymbol{H}$ from the vector model $\mathcal{H}^{\mathrm{V}}$ (2.3) is computed from

$$\boldsymbol{H} = \mathcal{H}^{\mathrm{V}}(\boldsymbol{B}) = \frac{2}{\pi} \int_{-\frac{\pi}{2}+\varphi_0}^{\frac{\pi}{2}+\varphi_0} \boldsymbol{e}_\varphi \mathcal{H}_\varphi^{\mathrm{S\text{-}V}}(\boldsymbol{B} \cdot \boldsymbol{e}_\varphi) \mathrm{d}\varphi \tag{2.18}$$

where the angle φ_0 defines the integration half-plane (Fig. 2.2), $\boldsymbol{e}_\varphi$ is the unit vector along the direction given by polar angle φ and $\mathscr{H}_\varphi^{\text{S-V}}$ is the scalar model corresponding to the direction given by polar angle φ, working under the vector model and defined by (2.7).

After choosing a finite number of equally-spaced directions N_d (Fig. 2.2), the integral in (2.18) is transformed into a sum

$$\boldsymbol{H} = \frac{2}{\pi}\Delta\varphi\sum_{n=1}^{N_\text{d}} \boldsymbol{e}_{\varphi_n}\mathscr{H}_n^{\text{S-V}}\left(\boldsymbol{B}\cdot\boldsymbol{e}_{\varphi_n}\right) \tag{2.19}$$

where $\Delta\varphi$ is the discretization angle

n is the direction index

$\boldsymbol{e}_{\varphi_n}$ is the unit vector along the direction given by polar angle φ_n

$\mathscr{H}_n^{\text{S-V}}$ is the scalar model corresponding to the direction given by polar angle φ_n, working under the vector model and defined by (2.7)

and

$$B_{\varphi_n} = \boldsymbol{B}\cdot\boldsymbol{e}_{\varphi_n} \tag{2.20}$$

is the geometrical projection of $\boldsymbol{B}$ in the direction of $\boldsymbol{e}_{\varphi_n}$ and the angle φ_n is given by

$$\varphi_n = -\frac{\pi}{2} + \varphi_0 + n\Delta\varphi; \qquad n = 1,2,...,N_\text{d} \tag{2.21}$$

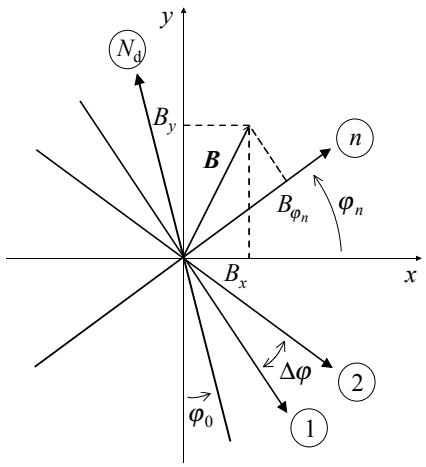

Figure 2.2. Finite number of directions in a vector model.

Obviously, there is an infinite number of scalar models in a vector model defined by Equation (2.18). The model exhibits the rotational symmetry, meaning that the output from the model does not depend on the choice of the angle φ_0. The introduction of a finite number of directions, however, disturbs the rotational symmetry, which causes the output from the vector model defined by Equation (2.19) to depend on the angle φ_0. There is a possibility to tackle this problem if the incorporation of the vector model in the finite element analysis is considered. The angle φ_0 is randomly chosen in each vector hysteresis model included in the finite element analysis, whereby the error is diminished and may be considered statistically negligible (Gyimóthy and Iványi, 1994).

The setting procedure of the limiting curve $H_{\text{lim}}^{\text{s-v}}$ associated with the scalar model $\mathcal{H}^{\text{s-v}}$ is described in the following subsection. Since only isotropic materials are considered, the same distribution function is used for each direction of the vector model.

2.3.2 Identification of the vector model

The identification procedure for a vector model is in general naturally more involved than that for a scalar one and it requires measurements in rotating fields (Mayergoyz, 1991). These measurements are complex and require a special experimental set-up, which has not been available. An advantageous feature of the vector Preisach model, which is the possibility, for isotropic materials, to identify the vector distribution function directly from the scalar one (Bottauscio et al., 1998) has been utilized. For the purpose of identification, a trivial condition has been used, stating that the output from a vector model magnetized along one direction should be equal to the output of the scalar model. A similar identification of a vector model has been performed by Gyimóthy and Iványi (1994), who calculated the Everett table for a scalar model working under a vector model.

The simplifying assumptions related to the vector distribution function can be stated as follows: In accordance with what has been stated above, the isotropic materials are considered only and therefore also the vector distribution function corresponds to a hysteresis model for an isotropic case. The determination of the vector distribution function is performed according to a simple procedure described in the following.

As previously discussed, the identification of a particular scalar model used in this work practically means the determination of the limiting curve. Therefore, the goal here is to determine the limiting curve $H_{\mathrm{lim}}^{\mathrm{s\text{-}v}}$ of a scalar model working under a vector model from the limiting curve $H_{\mathrm{lim}}^{\mathrm{s}}$ of a pure scalar model, and thus from the only measured data.

Consider the input $\boldsymbol{B}$ to the vector model $\mathcal{H}^{\mathrm{v}}$ varying along one direction, in particular along the direction coinciding with the *y*-axis in Fig. 2.2 and thus, assuming for simplicity φ_0 equal to zero, with the N_{d}-th direction of the vector model

$$\boldsymbol{B} = B_y \boldsymbol{j}\,; \qquad B_x = 0 \tag{2.22}$$

The output $\boldsymbol{H}$ from the vector model $\mathcal{H}^{\mathrm{v}}$ is computed through (2.19) with $\boldsymbol{B}$ given by (2.22). In particular, the components of $\boldsymbol{H}$ are computed from

$$H_x = 0 \tag{2.23}$$

$$H_y = \frac{2}{\pi}\Delta\varphi \sum_{n=1}^{N_{\mathrm{d}}} \mathcal{H}^{\mathrm{s\text{-}v}}\left(B_y \sin\varphi_n\right)\sin\varphi_n \tag{2.24}$$

Now, if B_y varies from positive saturation through the point B_z and after that down to the point $-B_z$ (2.9), the output from the scalar models in all directions will follow the upper branch of the limiting curve. For the model in the *n*-th direction the following holds

$$\mathcal{H}^{\mathrm{s\text{-}v}}\left(B_y \sin\varphi_n\right) = H_{\mathrm{lim}}^{\mathrm{s-v}}\left(B_y \sin\varphi_n\right) \tag{2.25}$$

Substituting (2.25) into (2.24) yields

$$H_y = \frac{2}{\pi}\Delta\varphi \sum_{n=1}^{N_{\mathrm{d}}} H_{\mathrm{lim}}^{\mathrm{s-v}}\left(B_y \sin\varphi_n\right)\sin\varphi_n \tag{2.26}$$

Since the input $\boldsymbol{B}$ varies along one direction only, a pure scalar model $\mathcal{H}^{\mathrm{s}}$ can be applied to compute the output as well

$$H_y = \mathcal{H}^{\mathrm{s}}\left(B_y\right) = H_{\mathrm{lim}}^{\mathrm{s}}\left(B_y\right) \tag{2.27}$$

The outputs from the two considered models, namely $\mathcal{H}^{\mathrm{v}}$ (2.26) and $\mathcal{H}^{\mathrm{s}}$ (2.27), should be equal, meaning that

$$\frac{2}{\pi}\Delta\varphi\sum_{n=1}^{N_{\mathrm{d}}} H_{\mathrm{lim}}^{\mathrm{s-v}}\left(B\sin\varphi_n\right)\sin\varphi_n = H_{\mathrm{lim}}^{\mathrm{s}}\left(B\right) \tag{2.28}$$

where, for the sake of clarity, the index y in B_y is omitted. The expression on the right-hand side represents the measured upper branch of the limiting hysteresis loop, provided that the values of B are chosen to be the measured values B_i^{m}, where i runs from 1 through the total number of measured points $N_{\mathrm{tot}}^{\mathrm{m}}$. Substituting B_i^{m} into (2.28) yields a system of $N_{\mathrm{tot}}^{\mathrm{m}}$ equations

$$\frac{2}{\pi}\Delta\varphi\sum_{n=1}^{N_{\mathrm{d}}} H_{\mathrm{lim}}^{\mathrm{s-v}}\left(B_i^{\mathrm{m}}\sin\varphi_n\right)\sin\varphi_n = H_{\mathrm{lim}}^{\mathrm{s}}\left(B_i^{\mathrm{m}}\right);\qquad i = 1\ldots N_{\mathrm{tot}}^{\mathrm{m}} \tag{2.29}$$

All the values on the right-hand side of (2.29) are known quantities. What is to be determined is $H_{\mathrm{lim}}^{\mathrm{s-v}}$ as a function of the measured B_i^{m}. In order to express the function $H_{\mathrm{lim}}^{\mathrm{s-v}}$ in terms of B_i^{m} instead of $B_i^{\mathrm{m}}\sin\varphi_n$ the linear interpolation is used. Hence, say that the value $B_i^{\mathrm{m}}\sin\varphi_n$ falls into the interval between two general measured points B_{i1}^{m} and B_{i2}^{m}

$$B_{i1}^{\mathrm{m}} \le B_i^{\mathrm{m}}\sin\varphi_n \le B_{i2}^{\mathrm{m}} \tag{2.30}$$

Thus, Equation (2.29) can be finally written as

$$\frac{2}{\pi}\Delta\varphi\sum_{n=1}^{N_{\mathrm{d}}}\left(H_{\mathrm{lim}}^{\mathrm{s-v}}\left(B_{i1}^{\mathrm{m}}\right)\frac{B_{i2}^{\mathrm{m}} - B_i^{\mathrm{m}}}{B_{i2}^{\mathrm{m}} - B_{i1}^{\mathrm{m}}} + H_{\mathrm{lim}}^{\mathrm{s-v}}\left(B_{i2}^{\mathrm{m}}\right)\frac{B_i^{\mathrm{m}} - B_{i1}^{\mathrm{m}}}{B_{i2}^{\mathrm{m}} - B_{i1}^{\mathrm{m}}}\right)\sin\varphi_n = H_{\mathrm{lim}}^{\mathrm{s}}\left(B_i^{\mathrm{m}}\right);\quad i = 1\ldots N_{\mathrm{tot}}^{\mathrm{m}} \tag{2.31}$$

The solution of this system of $N_{\mathrm{tot}}^{\mathrm{m}}$ equations for $N_{\mathrm{tot}}^{\mathrm{m}}$ unknowns provides the sought function $H_{\mathrm{lim}}^{\mathrm{s-v}}$. The results of the solution for a different number of directions N_{d} are reported in Chapter 4, Section 4.1. The limiting curve $H_{\mathrm{lim}}^{\mathrm{s-v}}$ expressed as $B_{\mathrm{lim}}^{\mathrm{s-v}}$, i.e. as a function of H, is then substituted for B_{lim} in (2.10)-(2.14) and defines the scalar model $\mathcal{H}^{\mathrm{s\text{-}v}}$ used under a vector model $\mathcal{H}^{\mathrm{v}}$.

3 Incorporation of hysteresis in field analysis of electric machines

3.1 Simplifying assumptions

Owing to the complex operation and geometry of an electric motor, the magnetic field follows complicated patterns. A complete analysis of the magnetic field of an electric motor, which is in general three-dimensional and time-dependent, is limited by the computing power of present-day computers. Especially if such an involved phenomenon as hysteresis is to be included in the field analysis of an electric motor, certain simplifications are indispensable.

From the point of view of incorporating hysteresis, the numerical technique described in the following is applicable to any electric machine. However, a close relation to induction motors in the following presentation cannot be avoided, because they have been chosen as test motors for the purpose of this thesis.

The simplifying assumptions adopted in this work can be divided into three categories. The first category includes the main simplifying assumption of a two-dimensional magnetic field; the second category comprises the simplifications related to modeling conductors of the stator winding and rotor cage, and the third category concerns the assumptions related to the nonlinear iron core modeling.

This work focuses on the computation of the core losses. In order to verify the computed results, the core losses have to be measured on actual motors. The only reasonable measurement of the core losses can be performed on motors running at no-load, because the core losses can be quite reliably separated from other loss components. This is obviously not true for other operation modes, such as full-load and locked-rotor ones. The simulations of motors are undoubtedly to be performed for the same operation conditions as were present during the measurements, that is the no-load conditions. Therefore, the magnetic field of the motors is studied at no-load. The no-load operation conditions make many of the simplifying assumptions fairly justifiable.

3.1.1 Assumption of a two-dimensional magnetic field

Apart from the complexity and high computational costs of the three-dimensional analysis of an electric machine, the geometrical input data representation and viewing of the results are inconvenient problems as well. Therefore, it is common practice to analyze an electric

machine on the assumption of its infinite axial length. This allows the field to be treated as two-dimensional, not dependent on the coordinate parallel to the shaft of the machine. Thus, the field is computed in a plane perpendicular to the shaft of the machine.

There are three main problems connected with the 2D magnetic field modeling: the influence of end-region fields, the skewing of rotor slots, and currents in the laminated iron core.

The influence of end-region fields is accounted for by introducing constant end-winding inductances into the voltage equations. Since the motors modeled in this work have unskewed rotor bars, the skewing of the rotor slots is irrelevant. Anyhow, both the end-windings and skewing of the rotor slots have only a small effect on the no-load characteristics.

All currents (both eddy currents or currents induced by potential differences of the rotor bars) flowing along the iron laminations are inconsistent with two-dimensional field analysis. Since the potential differences between the rotor bars in unskewed rotors are negligible, the inter-bar currents are usually of insignificant magnitudes.

3.1.2 Simplifications related to stator conductors and rotor cage

The stator winding is modeled using a circuit theoretical approach that assumes the current density distribution to be constant over the cross-section of the stator conductors. This means that the eddy currents and skin effect in the stator winding are ignored. As a matter of fact, the windings of modeled motors are made of such thin copper wires that the skin effect (and therefore the eddy currents) are negligible, which makes the assumption of constant current density permissible. If a detailed analysis of eddy-current effects in the stator windings is required, a technique of eliminating inner nodes, which results in the formation of macro elements, could be adopted (Szücs and Arkkio, 1999; Szücs, 2000).

Since the operation of motors is modeled at no-load, the rotor is forced to rotate at synchronous speed. The potential differences between the rotor bars remain small, which supports the assumption that the rotor cage is perfectly short-circuited. Nevertheless, the skin effect in the rotor bars is taken into account, since the rotor bars are treated as solid conductors.

3.1.3 Simplifications related to the iron core

As already mentioned above, the currents flowing along the iron sheets are not consistent with 2D magnetic field analysis. Hence, the laminated iron core is treated as a nonconducting medium, and the eddy-current losses are excluded from the field analysis. All core materials are assumed to be isotropic.

The main focus in this work is on the proper modeling of magnetic nonlinearity of the iron core, with the primary concern that the hysteresis is included in the field analysis. However, in order to make the computations more suitable from the time-consumption viewpoint, some further simplifications would be useful. The hysteresis loss in the rotor running at synchronous speed is considerably smaller than other loss components and it is negligible compared to the hysteresis loss in the stator. This allows the application of another simplification to the analysis, which lies in the negligence of the hysteresis loss in the rotor from the field analysis. The hysteretic relationship in the rotor core is replaced by a single-valued function. Note, however, that this simplification has nothing to do with the principal functionality of the method developed and is administered purely in order to save computation time. The method developed allows the hysteresis to be modeled in any desired region of a machine.

3.2 Field and circuit equations and their solution

3.2.1 Formulation of field equations

The two-dimensional solution region is the cross-section of the machine in a plane perpendicular to the shaft. If the symmetry occurs, the whole cross-section can be divided into a number of symmetry sectors with identical geometries and the field analysis is carried out only in one of these sectors, whereby the computation time is reduced. The assumption that no flux penetrates through the outer surface of the machine is adopted. This requires that the magnetic vector potential has a constant value (usually zero) on the boundary. Periodic boundary conditions are applied on the sides of a symmetry solution sector.

From magnetic materials' point of view, the regions covered by the mesh can be divided into magnetically linear regions and magnetically nonlinear regions. Depending on the nature of the model describing the $\boldsymbol{B}$-$\boldsymbol{H}$ relationship in nonlinear regions, these can be further divided

into single-valued regions, i.e. such regions in which the material nonlinearity is modeled by a single-valued function and hysteretic regions, i.e. such regions in which the material nonlinearity is governed by a vector model $\mathcal{H}^{\mathrm{v}}$. Consequently, the overall relationship between $\boldsymbol{H}$ and $\boldsymbol{B}$ can then be defined by a nonlinear function $\mathcal{F}^{\mathrm{v}}$

$$\boldsymbol{H} = \mathcal{F}^{\mathrm{v}}\left(\boldsymbol{B}\right) \tag{3.1}$$

such that

$$\mathcal{F}^{\mathrm{v}}\left(\boldsymbol{B}\right) = \begin{cases} \nu_0 \boldsymbol{B} & \text{in magnetically linear regions} \\ \nu_{\mathrm{sv}}\left(\left|\boldsymbol{B}\right|\right)\boldsymbol{B} & \text{in magnetically nonlinear single - valued regions} \\ \mathcal{H}^{\mathrm{v}}\left(\boldsymbol{B}\right) & \text{in magnetically nonlinear hysteretic regions} \end{cases} \tag{3.2}$$

with the following notation

ν_0 is the free space reluctivity

ν_{sv} is a single-valued function of the magnitude of $\boldsymbol{B}$

On the assumption of a two-dimensional magnetic field, the vector potential $\boldsymbol{A}$ and current density $\boldsymbol{J}$ have only one component. This component is oriented in the direction of the shaft (z-direction). Hence

$$\boldsymbol{A} = A\,\boldsymbol{e}_z \tag{3.3}$$

$$\boldsymbol{J} = J\,\boldsymbol{e}_z \tag{3.4}$$

where $\boldsymbol{e}_z$ is the unit vector in the z-direction, and A and J are the z-components of $\boldsymbol{A}$ and $\boldsymbol{J}$.

Since an induction motor is treated as a quasi-static magnetic system, the Maxwell equations in their quasi-static form are used. In such a case, and in accordance with the simplifying assumptions of the stator winding, rotor cage and iron core modeling, Equation (1.7) becomes

$$\nabla \times \mathcal{J}^{\nu}\left(\nabla \times \boldsymbol{A}\right) + \sigma \frac{\partial \boldsymbol{A}}{\partial t} - \beta_i \, i_i \, \boldsymbol{e}_z = 0 \tag{3.5}$$

where the nonlinear function $\mathcal{J}^{\nu}$ defining the relationship between $\boldsymbol{H}$ and $\boldsymbol{B}$ has already been introduced (3.2), subscript i stands for the phase index that runs from 1 through the number of phases of the stator winding m and

$$\beta_i = \begin{cases} \dfrac{N_{ci}}{S_i} & \text{in positively oriented coil sides of the phase } i \\ -\dfrac{N_{ci}}{S_i} & \text{in negatively oriented coil sides of the phase } i \\ 0 & \text{elsewhere} \end{cases} \tag{3.6}$$

with the following notation

N_{ci}	is the number of turns of a coil of the phase i
S_i	is the cross-sectional area of the i-th phase coil side
t	is time
σ	is the conductivity (zero everywhere, except the rotor bars and shaft)
i_i	is the i-th phase current

The current density in a coil of the i-th phase is given by

$$\boldsymbol{J}_i = \frac{N_{ci}}{S_i} i_i \, \boldsymbol{e}_z \tag{3.7}$$

The Coulomb gauge

$$\nabla \cdot \boldsymbol{A} = 0 \tag{3.8}$$

which is customarily used to assure the uniqueness of the solution in a general 3-D case, is automatically satisfied in a 2-D case.

If B-FPT is used to handle the nonlinearities involved, the function $\mathcal{F}^{\nu}$ in Equation (3.5) is split in nonlinear regions into two parts according to (1.5). Combining (1.5), Equations (3.3) and (3.4), the Coulomb gauge (3.8), and after some mathematical manipulations, Equation (3.5) is linearized and becomes

$$-\nabla\cdot\left(\nu_{xy}\nabla A\right)+\sigma\dot{A}+\left(\nabla\times\boldsymbol{R}_{\mathrm{FP}}\right)_z-\beta_i\,i_i=0 \tag{3.9}$$

where ν_{xy} is a function of position defined as

$$\begin{aligned}&\nu_{xy}=\nu_0 \qquad \text{in magnetically linear regions}\\ &\nu_{xy}=\nu_{\mathrm{FP}} \qquad \text{in magnetically nonlinear (single-valued and hysteretic) regions}\end{aligned} \tag{3.10}$$

A nonlinearity $\boldsymbol{R}_{\mathrm{FP}}$ is the Fixed-Point residual, which is defined only in nonlinear regions (in linear regions it is equal to the zero vector by definition), the subscript z indicates the z-component of a particular cross product and a dot over a letter signifies the time derivative. In (3.10) ν_{FP} stands for the Fixed-Point coefficient (1.6). Thus, for the linearized constitutive law in nonlinear regions holds

$$\boldsymbol{H}=\nu_{\mathrm{FP}}\boldsymbol{B}+\boldsymbol{R}_{\mathrm{FP}} \tag{3.11}$$

The solution of the basic field equation of an induction machine (3.5) and in turn of its linearized form (3.9) is accomplished by FEM, applying a weighted-residual approach.

3.2.2 Finite element solution of field equations

Using a weighted-residual approach, Equation (3.9) is multiplied by a trial function ξ and integrated over the entire solution region Ω (cross-section of the machine)

$$\int_{\Omega}-\nabla\cdot\left(\nu_{xy}\nabla A\right)\xi\,\mathrm{d}\Omega+\int_{\Omega}\sigma\dot{A}\,\xi\,\mathrm{d}\Omega+\int_{\Omega}\left(\nabla\times\boldsymbol{R}_{\mathrm{FP}}\right)_z\xi\,\mathrm{d}\Omega-\int_{\Omega}\xi\beta_i\,i_i\,\mathrm{d}\Omega=0 \tag{3.12}$$

After using some general vector identities and integral theorems, taking into account the boundary conditions, and after some mathematical manipulations, Equation (3.12) becomes

$$\int_{\Omega} \nu_{xy} \nabla A \cdot \nabla \xi \, \mathrm{d}\Omega + \int_{\Omega} \sigma \dot{A} \xi \, \mathrm{d}\Omega + \int_{\Omega} \left(\boldsymbol{R}_{\mathrm{FP}} \times \nabla \xi \right)_z \mathrm{d}\Omega - \int_{\Omega} \xi \beta_i \, i_i \, \mathrm{d}\Omega = 0 \tag{3.13}$$

In the finite element method the solution region is discretized into a number of finite elements. Recalling the definition of regions from the material point of view (3.2), the finite elements can be divided accordingly; that is, there are linear, nonlinear single-valued and nonlinear hysteretic elements, depending on their placement in the finite element mesh or more specifically on the nature of the material model describing the ***B*-*H*** behavior in the particular element. The field is to be computed in nodal points. The magnetic vector potential in the nodal points located on the outer surface of the machine (Dirichlet boundary) has a fixed value, which often has to be equal to zero. The potential in the nodes on the periodic boundary has the same positive or negative value as the corresponding node on the other side of a symmetry sector. The magnetic vector potential in the Neumann boundary nodes, as well as in all the other nodes (except the Dirichlet nodes and periodic-boundary nodes) is free to vary and the corresponding nodes are free or active nodes. The approximate solution is found as the following linear combination

$$A \cong \sum_{i=1}^{N_{\mathrm{n}}} N_i A_i \tag{3.14}$$

where N_i is a global shape function corresponding to the node i

A_i is a value of the vector potential in the node i

N_{n} is the total number of nodes in the finite element mesh

Substitution of (3.14) into (3.13) yields

$$\sum_{i=1}^{N_{\mathrm{n}}} A_i \int_{\Omega} \nu_{xy} \nabla N_i \cdot \nabla \xi \, \mathrm{d}\Omega + \sum_{i=1}^{N_{\mathrm{n}}} \dot{A}_i \int_{\Omega} \sigma N_i \, \xi \, \mathrm{d}\Omega + \int_{\Omega} \left(\boldsymbol{R}_{\mathrm{FP}} \times \nabla \xi \right)_z \mathrm{d}\Omega - \int_{\Omega} \xi \beta_i \, i_i \, \mathrm{d}\Omega = 0 \tag{3.15}$$

According to the Galerkin approach, a test function ξ is chosen to be a shape function N_j, where j runs from 1 through the total number of active nodes N_{a}. Thus, the following system of N_{a} ordinary differential equations of N_{a} unknown nodal values of the vector potential is obtained

$$\sum_{i=1}^{N_\mathrm{n}} A_i \int_{\Omega} \nu_{xy} \nabla N_i \cdot \nabla N_j \,\mathrm{d}\Omega + \sum_{i=1}^{N_\mathrm{n}} \dot{A}_i \int_{\Omega} \sigma N_i N_j \,\mathrm{d}\Omega$$

$$+ \int_{\Omega} \left(\boldsymbol{R} \times \nabla N_j \right)_z \mathrm{d}\Omega - \int_{\Omega} N_j \beta_i i_i \,\mathrm{d}\Omega = 0 \qquad j = 1,\ldots,N_\mathrm{a} \tag{3.16}$$

This can be written in a more compact form

$$\sum_{i=1}^{N_\mathrm{n}} S_{ij} A_i + \sum_{i=1}^{N_\mathrm{n}} T_{ij} \dot{A}_i - P_j + \sum_{i=1}^{m} D_{ji} i_i = 0 \qquad j = 1,\ldots,N_\mathrm{a} \tag{3.17}$$

where m denotes the number of phases of the stator winding and

$$S_{ij} = \int_{\Omega} \nu_{xy} \nabla N_i \cdot \nabla N_j \,\mathrm{d}\Omega \tag{3.18}$$

$$T_{ij} = \int_{\Omega} \sigma N_i N_j \,\mathrm{d}\Omega \tag{3.19}$$

$$D_{ij} = -\int_{\Omega} \beta_i N_j \,\mathrm{d}\Omega \tag{3.20}$$

$$P_j = -\int_{\Omega} \left(\boldsymbol{R}_\mathrm{FP} \times \nabla N_j \right)_z \mathrm{d}\Omega \tag{3.21}$$

Denoting

$$\mathbf{S} = \left\{ S_{ij} \right\}, \qquad j = 1,\ldots,N_\mathrm{n};\ j = 1,\ldots,N_\mathrm{a} \tag{3.22}$$

$$\mathbf{T} = \left\{ T_{ij} \right\} \qquad j = 1,\ldots,N_\mathrm{n};\ j = 1,\ldots,N_\mathrm{a} \tag{3.23}$$

$$\mathbf{D} = \left\{ D_{ij} \right\} \qquad i = 1,\ldots,m;\ \ j = 1,\ldots,N_\mathrm{a} \tag{3.24}$$

$$\mathbf{P} = \left\{ P_j \right\} \qquad j = 1,\ldots,N_\mathrm{a} \tag{3.25}$$

makes it possible to write the system (3.17) in a matrix form

$$\mathbf{S}\mathbf{A} + \mathbf{T}\dot{\mathbf{A}} - \mathbf{P}(\mathbf{A}) + \mathbf{D}^\mathrm{T}\mathbf{i} = \mathbf{0} \tag{3.26}$$

where superscript T signifies a transposed matrix, **A** is a column vector of nodal vector potential values

$$\mathbf{A} = \left\{ A_j \right\} \qquad j = 1,...,N_{\mathrm{n}} \tag{3.27}$$

and **i** is a column vector of phase currents

$$\mathbf{i} = \left\{ i_j \right\} \qquad j = 1,...,m \tag{3.28}$$

Looking at (3.21) it is seen that the elements of **P** depend on $\boldsymbol{R}_{\mathrm{FP}}$, which in turn depends on $\boldsymbol{B}$ through (3.11). Since $\boldsymbol{B}$ is computed directly from $\boldsymbol{A}$, it is clear that **P** depends on the solution **A**, which is emphasized in Equation (3.26).

The integration of expressions for the entries of matrices (3.18) - (3.21) is performed numerically by using the Gaussian quadrature. This issue is closely associated with the relation between the finite elements and hysteresis models and it is addressed in the following.

3.2.3 Finite elements and hysteresis models

From the viewpoint of the relation between the finite elements and hysteresis models, the matrix **P** (3.21) plays a crucial role. The reason is that this matrix is associated with $\boldsymbol{R}_{\mathrm{FP}}$, which is directly related to $\boldsymbol{H}$ and $\boldsymbol{B}$ through (3.11) and the relation between $\boldsymbol{H}$ and $\boldsymbol{B}$ in hysteretic elements is modeled through the vector hysteresis model. Depending on the order of the finite element mesh and the variation of $\boldsymbol{R}_{\mathrm{FP}}$ inside a nonlinear element, a certain minimum number of Gaussian integration points per finite element N_{ip} is needed for accurate enough integration of the matrix **P**. The two-column vectors, consisting of x and y components, can be defined

$$\underline{\mathbf{B}} = \left\{ \boldsymbol{B}^e \right\}, \quad \underline{\mathbf{H}} = \left\{ \boldsymbol{H}^e \right\}, \quad \underline{\mathbf{R}}_{\mathrm{FP}} = \left\{ \boldsymbol{R}_{\mathrm{FP}}^e \right\} \qquad e = 1,...,N_{\text{ip-tot}} \tag{3.29}$$

where $\boldsymbol{B}^e$, $\boldsymbol{H}^e$ and $\boldsymbol{R}_{\mathrm{FP}}^e$ are the flux density, field strength and Fixed-Point residual values in a particular integration point e and $N_{\text{ip-tot}}$ is the total number of integration points in all nonlinear elements used to numerically integrate the matrix **P**.

For a first-order mesh, which is typically used when the hysteresis is taken into account in the magnetic field computations, the variation of the magnetic vector potential inside an element is linear and the flux density and field strength are constant, which in turn means that $\boldsymbol{R}_{\mathrm{FP}}$ is constant as well, because $\boldsymbol{H}$, $\boldsymbol{B}$ and $\boldsymbol{R}_{\mathrm{FP}}$ are coupled through (3.11). Hence, the Gaussian quadrature requires one integration point per finite element for exact integration of the matrix **P** and the total number of integration points $N_{\mathrm{ip\text{-}tot}}$ is equal to the number of nonlinear finite elements.

From the previous discussion it is clear that the number of vector hysteresis models in the analysis coincides with the number of integration points in the hysteretic elements. If the number of hysteretic elements is denoted as N_{he}, then the total number of vector hysteresis models included in the analysis N_{vhm} will be

$$N_{\mathrm{vhm}} = N_{\mathrm{ip}} N_{\mathrm{he}} \tag{3.30}$$

Taking into account the number of directions of each vector hysteresis model N_{d}, the total number of scalar models included in the analysis N_{shm} is

$$N_{\mathrm{shm}} = N_{\mathrm{vhm}} N_{\mathrm{d}} \tag{3.31}$$

The history for each of N_{shm} scalar models is traced and stored in the computer memory in the form of local and global maxima and minima in order to correctly evaluate the output from each particular model.

3.2.4 Voltage equations of the stator winding

As already mentioned, it is assumed that the conductors of stator windings are made so thin that the skin effect is negligible. The current density in a coil side is constant and is calculated from Equation (3.7). The voltage equations of the stator winding are constructed in accordance with the adopted circuit theoretical approach. For the phase voltage u_i of the i-th phase holds

$$u_i = R_s i_i + L_{ew} \dot{i}_i + \dot{\Psi}_i \tag{3.32}$$

where R_s is the total phase winding resistance

L_{ew} is the end-winding inductance

Ψ_i is the flux linkage of the *i*-th phase associated with the two-dimensionally modeled core region

The flux linkage Ψ_i is calculated as a surface integral of the magnetic vector potential over the coil sides of the phase *i*. This can be expressed as the following surface integral over the entire solution region Ω

$$\Psi_i = N_s l_{Fe} \int_{\Omega} \beta_i \, A \, d\Omega \tag{3.33}$$

where N_s is the number of symmetry sectors into which the machine can be split

l_{Fe} is the equivalent core length of the machine

β_i are the functions defined by Equation (3.6)

The flux linkage is obtained from the finite element solution. Thus, a substitution of the approximate solution of the vector potential (3.14) into (3.33) yields

$$\Psi_i = N_s l_{Fe} \sum_{j=1}^{N_n} \int_{\Omega} \beta_i \, N_j \, d\Omega \; A_j \tag{3.34}$$

Now, by making use of Equations (3.34) and (3.20), Equation (3.32) can be rewritten

$$u_i = R_s i_i + L_{ew} \dot{i}_i - N_s l_{Fe} \sum_{j=1}^{N_n} D_{ij} \dot{A}_j \tag{3.35}$$

which, when written in a compact matrix form gives

$$\mathbf{u} = R_s \, \mathbf{i} + L_{ew} \, \dot{\mathbf{i}} - N_s l_{Fe} \, \mathbf{D}\dot{\mathbf{A}} \tag{3.36}$$

where $\mathbf{u}$ is a column vector of phase voltages

$$\mathbf{u} = \{u_j\} \qquad j = 1,...,m \tag{3.37}$$

The matrix **D** is defined by (3.20) and the column vectors **A** and **i** are given by (3.27) and (3.28), respectively.

3.2.5 Time discretization of combined field and voltage equations

The field equation (3.26) and circuit equation (3.36) are combined into one system of equations

$$\begin{bmatrix} \mathbf{T} & \mathbf{0} \\ -N_s l\,\mathbf{D} & \mathbf{Z}_{LD} \end{bmatrix} \cdot \begin{bmatrix} \dot{\mathbf{A}} \\ \dot{\mathbf{i}} \end{bmatrix} = \begin{bmatrix} \mathbf{P}(\mathbf{A}) \\ \mathbf{u} \end{bmatrix} - \begin{bmatrix} \mathbf{S} & \mathbf{D}^{T} \\ \mathbf{0} & \mathbf{Z}_{RD} \end{bmatrix} \cdot \begin{bmatrix} \mathbf{A} \\ \mathbf{i} \end{bmatrix} \tag{3.38}$$

where $\mathbf{Z}_{LD} = L_{ew}\,\mathbf{I}$ and $\mathbf{Z}_{RD} = R_s\,\mathbf{I}$ with **I** being a unity $(m \times m)$ matrix. The system (3.38) is a system of ordinary differential equations and represents an initial value problem. In order to solve this problem, the initial conditions should be defined. A discussion about the initial conditions is given later (Section 3.2.7).

The time discretization of (3.38) is performed by the Crank-Nicholson time-stepping scheme. Hence, in the time step *n* the solution is found from the following equation system

$$\begin{bmatrix} \mathbf{S}_n + \frac{2}{\Delta t}\mathbf{T} & \mathbf{D}^{T} \\ \mathbf{D} & \mathbf{G}_{D1} \end{bmatrix} \cdot \begin{bmatrix} \mathbf{A}_n \\ \mathbf{i}_n \end{bmatrix} = \begin{bmatrix} -\mathbf{S}_{n-1} + \frac{2}{\Delta t}\mathbf{T} & -\mathbf{D}^{T} \\ \mathbf{D} & \mathbf{G}_{D2} \end{bmatrix} \cdot \begin{bmatrix} \mathbf{A}_{n-1} \\ \mathbf{i}_{n-1} \end{bmatrix}$$
$$+ \begin{bmatrix} \mathbf{P}_{n-1}(\mathbf{A}_{n-1}) \\ \mathbf{0} \end{bmatrix} + \begin{bmatrix} \mathbf{P}_n(\mathbf{A}_n) \\ \mathbf{0} \end{bmatrix} + C_u \begin{bmatrix} \mathbf{0} \\ \mathbf{u}_n + \mathbf{u}_{n-1} \end{bmatrix} \tag{3.39}$$

where

$$\mathbf{G}_{D1} = \frac{-\frac{1}{2}\Delta t R_s - L_{ew}}{N_s l}\mathbf{I} \tag{3.40}$$

$$\mathbf{G}_{\mathrm{D2}} = \frac{\frac{1}{2}\Delta t R_{\mathrm{s}} - L_{\mathrm{ew}}}{N_{\mathrm{s}} l}\mathbf{I} \tag{3.41}$$

$$C_{\mathrm{u}} = -\frac{\Delta t}{2 N_{\mathrm{s}} l} \tag{3.42}$$

and Δt is the time interval.

Equation (3.39) is so written that all terms on its right-hand side are known, whereas the column vectors on its left-hand side are to be computed. It is a system of algebraic equations, which represents a space- and time-discretized and linearized form of hysteretic parabolic equation (3.5) combined with a time-discretized circuit equation (3.32). To find the solution, the system (3.39) must be included in an iterative scheme.

3.2.6 Iterative solution of the resulting hysteretic system of algebraic equations

The iterative solution of (3.39) can be achieved by double iteration, i.e. the iteration in which the nodal values of the vector potential are found from the system represented by the first row of (3.39) using some guessed values for the currents, and after that the currents are corrected using the system represented by the second row of (3.39). Then, the nodal values of the vector potential are computed again and the currents are adjusted. This double iteration is repeated until the convergence limit is reached. However, the iteration in which both the systems are solved simultaneously is substantially more effective than the double iteration. The reason is that the number of unknowns in the combined system is only a little larger than the number of unknowns in the discretized field equation, since the number of voltage equations is normally small. Hence, the computation time of the combined solution does not increase much when compared with the solution of the finite element problem alone. Therefore, the simultaneous iteration has been used for solving the nonlinear system of equations (3.39).

For the sake of clarity when explaining the iterative procedure, the following matrices are introduced

$$\mathbf{E}_n = \begin{bmatrix} \mathbf{S}_n + \dfrac{2}{\Delta t}\mathbf{T} & \mathbf{D}^{\mathrm{T}} \\ \mathbf{D} & \mathbf{G}_{\mathrm{D1}} \end{bmatrix} \tag{3.43}$$

$$\mathbf{g}_n = \begin{bmatrix} -\mathbf{S}_{n-1} + \dfrac{2}{\Delta t}\mathbf{T} & -\mathbf{D}^{\mathrm{T}} \\ \mathbf{D} & \mathbf{G}_{\mathrm{D2}} \end{bmatrix} \cdot \begin{bmatrix} \mathbf{A}_{n-1} \\ \mathbf{i}_{n-1} \end{bmatrix} + \begin{bmatrix} \mathbf{P}_{n-1}(\mathbf{A}_{n-1}) \\ \mathbf{0} \end{bmatrix} + C_{\mathrm{u}} \begin{bmatrix} \mathbf{0} \\ \mathbf{u}_n + \mathbf{u}_{n-1} \end{bmatrix} \tag{3.44}$$

Using this notation and omitting the time-step index n Equation (3.39) becomes

$$\mathbf{E} \cdot \begin{bmatrix} \mathbf{A} \\ \mathbf{i} \end{bmatrix} = \begin{bmatrix} \mathbf{P}(\underline{\mathbf{R}}_{\mathrm{FP}}) \\ \mathbf{0} \end{bmatrix} + \mathbf{g} \tag{3.45}$$

where, for an unmistakable demonstration of the iterative scheme, a two-column vector $\underline{\mathbf{R}}_{\mathrm{FP}}$ (3.29) is recalled in order to point out the dependence of the column vector **P** directly on the Fixed-Point residual $\underline{\mathbf{R}}_{\mathrm{FP}}$, as done in (3.45), and not on **A**, as has been preferred in the equations presented so far. All other matrices and column vectors are constant and do not change during the iterative process.

The iteration starts with the assumption of some initial guess for $\underline{\mathbf{R}}_{\mathrm{FP}}$, say $\underline{\mathbf{R}}^{0}_{\mathrm{FP}}$, where the superscript signifies the iteration step. It is taken to be the value of $\underline{\mathbf{R}}_{\mathrm{FP}}$ from the previous time step. Now, the column vector **P** can be formed using (3.21) and inserted into (3.45). The solution of the linear system can be carried out, yielding the values of **A** and **i**. Using newly computed values of **A**, the flux density two-column vector $\underline{\mathbf{B}}$ is computed. From the two-column vector $\underline{\mathbf{B}}$, the two-column vector $\underline{\mathbf{H}}$ is evaluated according to Equations (3.1) and (3.2). In single-valued elements, the single-valued relationship is used. In hysteretic elements, $\boldsymbol{H}$ is computed from $\boldsymbol{B}$ through the vector hysteresis engine $\mathcal{H}^{\mathrm{v}}$. The values of $\underline{\mathbf{B}}$ and $\underline{\mathbf{H}}$ in nonlinear and hysteretic elements are used for the determination of a new Fixed-Point residual $\underline{\mathbf{R}}^{1}_{\mathrm{FP}}$ through (3.11). This two-column vector is inserted back into (3.45) and the iteration steps are repeated until the convergence limit is satisfied. As the criterion of convergence, the ratio of the l_1 norm of the change of **A** in two consequent iterations and the l_1 norm of **A** has been used. The flowchart of the iterative procedure is depicted in Fig. 3.1, where k denotes the

iteration step. After the iteration has converged, the hysteresis engine is updated. In practice it means that possible global and local extrema of the magnetic field and flux density time variation in each hysteretic element are detected and stored in the computer memory. The iteration is repeated in each time step. The computation times and numbers of iterations are discussed in Section 4.4.

3.2.7 Overall computational algorithm

A period of the supply voltage is divided into certain number of time steps. Starting from some initial state, the simulation of the magnetic field behavior is carried out step-by-step. The evaluation of average quantities (torque, powers in the power balance, losses) requires the simulation of the steady-state operation.

If the time-stepping simulation is started from the zero field as an initial state, the starting of the motor is actually simulated. The transient phenomena connected with the starting can last for tens of periods of the supply voltage until the steady state is reached. These long transients take place because there are usually large time constants associated with the windings of electric machines. It is practically impossible to simulate such long transients. Therefore, an initial state starting from which the steady state would be reached faster has to be sought.

The results of the sinusoidal approximation in combination with the subsequent magnetostatic field computation have proven to give a good enough initial state for the time-stepping analysis (Arkkio, 1987).

First, the sinusoidal-approximation computation is carried out. The variation of the quantities in the motor is assumed to be sinusoidal. The analysis is performed in the steady state using phasors. The behavior of the iron core is modeled using the effective reluctivity approach, with the definition of the effective reluctivity as suggested by Luomi et al. (1986). The input to the sinusoidal-approximation analysis is the RMS value of the supply voltage. The analysis gives the RMS values of quantities, among which the RMS values of the stator currents are of principal interest.

The values of the currents in all the phases computed at a certain instant in time from the sinusoidal approximation are fixed and the DC magnetic field caused by these currents is

computed. In this computation it is assumed that the iron core is demagnetized. Thus, the magnetization of the core in hysteretic elements proceeds along the virgin curve. The magnetic field computed in such a way is stored and used as an initial state for the time-stepping analysis. The results of this computation are also used to set the initial state of hysteresis models, i.e. to initialize the hysteresis models.

If the step-by-step analysis is initiated from the computed DC field and corresponding instantaneous currents, instead of the zero field and zero currents, a reasonable steady state is normally attained after only a couple of periods. In each time step the iterative procedure shown in Fig 3.1 is performed.

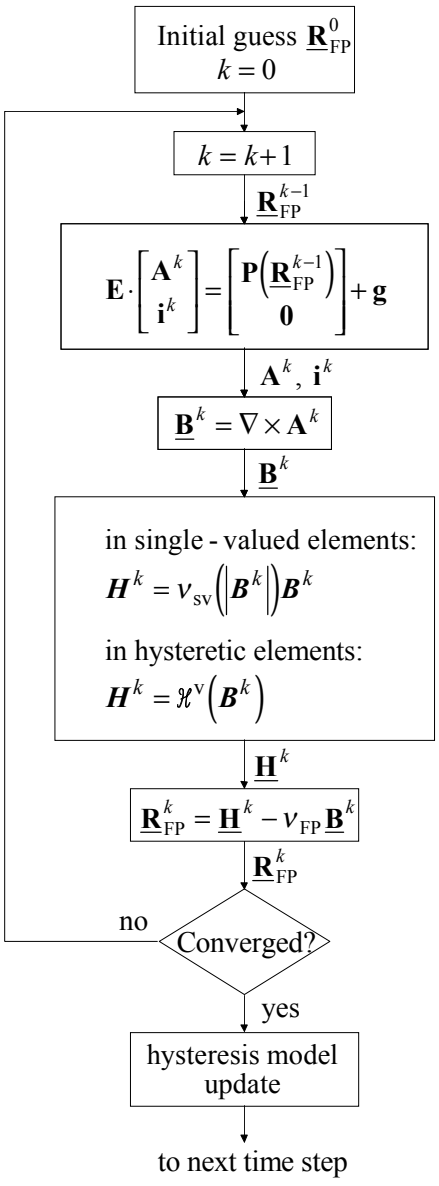

Fig. 3.1. Flowchart of the Fixed-Point iterative process as applied for a time-step solution of the combined highly nonlinear field and circuit equation system.

Thus, the overall computational algorithm of determining the variation of the magnetic field by the time-stepping method taking the ferromagnetic hysteresis into account and a consequent estimation of the power balance and core losses in an induction motor consists of five main blocks: sinusoidal approximation, initial DC-field computation, initialization of the vector hysteresis engine, step-by-step simulation itself with updating vector hysteresis models after each time step and power balance and core loss evaluation.

3.3 Core loss model

The core loss model of an induction motor that was used is based on the core loss separation concept, as discussed in Section 1.2.1. Thus, the total core loss density is estimated as a sum of the stator and rotor hysteresis, eddy-current and excess losses

$$p^{\text{core}} = p_{\text{st}}^{\text{hys}} + p_{\text{rt}}^{\text{hys}} + p^{\text{class}} + p^{\text{exc}} \tag{3.46}$$

In order to emphasize that the stator hysteresis loss is included in the field analysis and therefore computed in a different way than the rotor hysteresis loss, the total hysteresis loss is separated into two parts. Since the rotor hysteresis loss, and the stator and rotor eddy-current and excess losses are not included in the field analysis, they are determined by using the empirical formulae (Bertotti et al., 1994; Zhu et al., 1992; Zhu and Ramsden, 1998).

If not stated otherwise, the core loss formulae presented below are expressed in W/m³. In order to get the power loss in Watts, integration over the whole core volume has to be carried out.

3.3.1 Stator hysteresis loss

The stator hysteresis loss density is computed from

$$p_{\text{st}}^{\text{hys}} = \frac{1}{T}\int_T \boldsymbol{H}\cdot\frac{\mathrm{d}\boldsymbol{B}}{\mathrm{d}t}\,\mathrm{d}t = \frac{1}{T}\int_T \left(H_x \frac{\mathrm{d}B_x}{\mathrm{d}t} + H_y \frac{\mathrm{d}B_y}{\mathrm{d}t} \right)\mathrm{d}t \tag{3.47}$$

where T is the time period. The power loss density in (3.47) can be alternatively expressed as a sum of two components (Atallah and Howe, 1993)

$$p_{\mathrm{st}}^{\mathrm{hys}} = \frac{1}{T}\int_T |\boldsymbol{H}| \frac{\mathrm{d}|\boldsymbol{B}|}{\mathrm{d}t} cos\,\alpha \mathrm{d}t + \frac{1}{T}\int_T \frac{\mathrm{d}\theta}{\mathrm{d}t}\left(\boldsymbol{H}\times\boldsymbol{B}\right)_z \mathrm{d}t \tag{3.48}$$

where θ is the angle between the x-axis and vector $\boldsymbol{B}$ (angular position of $\boldsymbol{B}$), and α is the angle of lag between $\boldsymbol{H}$ and $\boldsymbol{B}$. The first term in (3.48) corresponds to the loss in a purely alternating field, because the derivative $\frac{\mathrm{d}\theta}{\mathrm{d}t}$ in such a field is zero, which makes the second term in (3.48) vanish. Hence

$$p_{\mathrm{st}}^{\text{hys-alt}} = \frac{1}{T}\int_T |\boldsymbol{H}| \frac{\mathrm{d}|\boldsymbol{B}|}{\mathrm{d}t} \mathrm{d}t \tag{3.49}$$

On the other hand, in the case of a purely rotating (circular) field, the derivative $\frac{\mathrm{d}|\boldsymbol{B}|}{\mathrm{d}t}$ is zero and the first term in (3.48) vanishes

$$p_{\mathrm{st}}^{\text{hys-rot}} = \frac{1}{T}\int_T \frac{\mathrm{d}\theta}{\mathrm{d}t}\left(\boldsymbol{H}\times\boldsymbol{B}\right)_z \mathrm{d}t \tag{3.50}$$

Thus, the total loss density is the sum of the alternating and rotational components

$$p_{\mathrm{st}}^{\mathrm{hys}} = p_{\mathrm{st}}^{\text{hys-alt}} + p_{\mathrm{st}}^{\text{hys-rot}} \tag{3.51}$$

3.3.2 Rotor hysteresis loss

The cylindrical components of the flux density are deduced from the calculated time variation of the flux density vector $\boldsymbol{B}$. The Fourier analysis is applied and each of the cylindrical components of $\boldsymbol{B}$ is expressed as a Fourier series

$$B_r = \sum_{k=1}^{N_{\mathrm{FC}}} B_{rk}\, sin\left(2\pi\, kft + \vartheta_{rk}\right) \tag{3.52}$$

$$B_\varphi = \sum_{k=1}^{N_{\mathrm{FC}}} B_{\varphi k}\, sin\left(2\pi\, kft + \vartheta_{\varphi k}\right) \tag{3.53}$$

where B_r is the radial component of $\boldsymbol{B}$

B_φ is the tangential component of $\boldsymbol{B}$

B_{rk} is the peak value of k-th harmonic component of B_r

ϑ_{rk} is the phase of k-th harmonic component of B_r

$B_{\varphi k}$ is the peak value of k-th harmonic component of B_φ

$\vartheta_{\varphi k}$ is the phase of k-th harmonic component of B_φ

f is the fundamental frequency

k is the harmonic order

N_{FC} is the total number of Fourier components included in the analysis

The hysteresis loss density in the rotor (and in the stator, if a single-valued function is used to model the B-H relationship instead of the hysteresis model) is computed from

$$p_{\mathrm{rt}}^{\mathrm{hys}} = \sum_{k=1}^{N_{\mathrm{FC}}} C_{\mathrm{hys}} k f B_{k\,\mathrm{maj}}^{n_{\mathrm{hys}}} \tag{3.54}$$

where C_{hys} and n_{hys} are constants depending on the material characteristics and $B_{k\mathrm{maj}}$ is the major axis of the ellipse traced by the k-th harmonic flux density vector.

3.3.3 Classical loss

The formula for the classical loss density contribution reads

$$p^{\mathrm{class}} = \frac{C_{\mathrm{class}}}{2\pi^2} \frac{1}{T} \int_T \left[\left(\frac{\mathrm{d}\, B_r}{\mathrm{d}\, t} \right)^2 + \left(\frac{\mathrm{d}\, B_\varphi}{\mathrm{d}\, t} \right)^2 \right] \mathrm{d}\, t \tag{3.55}$$

where C_{class} is the classical loss coefficient

$$C_{\mathrm{class}} = \frac{\pi^2 \sigma d^2}{6} \tag{3.56}$$

with σ being the electrical conductivity and d the lamination thickness.

3.3.4 Excess loss

The excess loss density is computed from the following integral

$$p^{\text{exc}} = C_{\text{exc}} \frac{1}{T} \int_T \left[\left(\frac{\mathrm{d}\, B_r}{\mathrm{d}\, t} \right)^2 + \left(\frac{\mathrm{d}\, B_\varphi}{\mathrm{d}\, t} \right)^2 \right]^{0.75} \mathrm{d}\, t \tag{3.57}$$

where C_{exc} is the excess loss coefficient.

3.3.5 Determination of the core loss coefficients

The coefficients C_{hys}, n_{hys} and C_{exc} are determined from the core loss separation measurements under alternating sinusoidal flux density (see for example Zhu and Ramsden (1995)) performed on a material sample (Appendix A). The measurement set-up along with the list of devices used in the measurement is presented in Appendix C.

First, the total core loss was measured under sinusoidal flux supply. From this total loss, the hysteresis and classical losses should be subtracted in order to get the excess loss.

Hysteresis loss coefficients

The evaluation of the hysteresis loss was carried out by utilizing the quasi-static hysteresis loops measurements. A measured family of quasi-static hysteresis loops was taken and the areas of the loops were numerically computed, resulting in the hysteresis loss per cycle.

Having experimentally determined the hysteresis loss, the coefficients C_{hys} and n_{hys} are found by fitting the measured hysteresis loss versus peak flux density curve using the least squares method. The hysteresis loss density under alternating sinusoidal flux is computed empirically using the Steinmetz formula

$$p_{\text{sin}}^{\text{hys}} = C_{\text{hys}} f B_{\text{p}}^{n_{\text{hys}}} \tag{3.58}$$

where B_{p} is the peak flux density. The determined coefficients are used in Equation (3.54) for computing the hysteresis loss under distorted and rotating flux.

Analytical calculation of the classical loss

The evaluation of the classical loss density under sinusoidal flux is straightforward

$$p_{\text{sin}}^{\text{class}} = C_{\text{class}} f^2 B_{\text{p}}^2 \tag{3.59}$$

where C_{class} is given by (3.56).

Excess loss coefficient

The excess loss coefficient C_{exc} used to compute the excess losses through (3.57) remains to be determined. The excess loss density under alternating sinusoidal flux is computed from

$$p_{\text{sin}}^{\text{exc}} = 8.7634\, C_{\text{exc}} f^{1.5} B_{\text{p}}^{1.5} \tag{3.60}$$

Here the coefficient 8.7634 appears so that a more general equation (3.57) reduces to (3.60) for alternating sinusoidal flux.

The excess loss is obtained as the difference between the total measured core loss and the sum of the hysteresis and classical losses. The measurement was performed for several frequencies and peak flux densities. The coefficient that gives the best fit over a range of frequencies and peak flux densities was determined. As a simplification, the same excess loss coefficient is used for both the alternating and rotational losses. In general, the coefficient of rotational excess loss is a function of the flux density and reduces to zero when the material is saturated and the domain structure disappears (Bertotti et al., 1994; Zhu and Ramsden, 1998).

All experimentally determined core loss coefficients are given in Table 4.2 in Section 4.1, where an example of the core loss separation for the considered material is also presented.

3.4 Power balance

An important indicator of the correctness of the motor numerical analysis is the power balance. Unlike a conventional finite element analysis of electric machines, in which the core losses are not included in the field computation, the hysteresis losses of the stator core contribute to the model power balance. Therefore, the power balance of a model motor at constant rotation speed and in the steady state is written as

$$P^{\text{in}} = P^{\text{out}} + P_{\text{st}}^{\text{res}} + P_{\text{rt}}^{\text{res}} + P_{\text{st}}^{\text{hys}} \tag{3.61}$$

where P^{in} is the input power of the stator winding

P^{out} is the output power on the shaft

$P_{\text{st}}^{\text{res}}$ is the resistive losses of the stator winding

$P_{\text{rt}}^{\text{res}}$ is the resistive losses of the rotor cage

$P_{\text{st}}^{\text{hys}}$ is the hysteresis losses of the stator core

Note that the power balance expressed by (3.61) is not the power balance of a real motor but the one of a model motor. Hence, it only comprises those components of power that are included in the analysis of a motor. The eddy-current (classical and excess) losses and the rotor hysteresis losses are not included in the analysis and therefore they are not included in (3.61) either. The friction losses are also neglected in (3.61). The components in (3.61) represent the time average values of appropriate instantaneous powers, as becomes clear from the following.

The input power of the stator winding is computed from

$$P^{\text{in}} = \sum_{i=1}^{m} \frac{1}{T} \int_T u_i i_i \, \mathrm{d}t \tag{3.62}$$

where the subscript i is the phase index and m stands for the number of phases.

The output power on the shaft is given by

$$P^{\text{out}} = w_{\text{m}} \frac{1}{T} \int_T T_{\text{e}} \, \mathrm{d}t \tag{3.63}$$

where w_{m} is the mechanical angular frequency of the rotor and T_{e} is the electromagnetic torque, computed through the Maxwell stress tensor from a surface integral

$$\boldsymbol{T}_{\text{e}} = \oint_S \boldsymbol{r} \times \left(\frac{1}{\mu_0} (\boldsymbol{B} \cdot \boldsymbol{n}) \boldsymbol{B} - \frac{1}{2\mu_0} B^2 \boldsymbol{n} \right) \mathrm{d}S \tag{3.64}$$

where $\boldsymbol{n}$ is the unit normal vector of the integration surface S. Applying (3.64) for the torque computation in induction machines, it is transformed to a line integral along the air gap

$$T_{\mathrm{e}} = \frac{l_{\mathrm{Fe}}}{\mu_0} \int_0^{2\pi} r^2 \, B_r B_\varphi \, \mathrm{d}\varphi \tag{3.65}$$

with l_{Fe} being the equivalent core length of the machine. The integration path in (3.65) is a circle of radius r. As shown by Arkkio (1987), the line integral of (3.65) can be replaced by a surface integral over the air gap

$$T_{\mathrm{e}} = \frac{l_{\mathrm{Fe}}}{\mu_0 \left(r_{\mathrm{out}} - r_{\mathrm{in}} \right)} \int_{S_{\mathrm{ag}}} r B_r B_\varphi \, \mathrm{d}S \tag{3.66}$$

with r_{out} and r_{in} being the outer and inner radii of the air gap and S_{ag} represents the cross-sectional area of the air gap. According to Arkkio (1987), the integral (3.66) has proven to give more reliable results of the torque computation than (3.65).

The resistive loss of the stator winding is computed from

$$P_{\mathrm{st}}^{\mathrm{res}} = \sum_{n=1}^{m} \frac{1}{T} \int_T R_{\mathrm{s}} i_n^2 \, \mathrm{d}t \tag{3.67}$$

and the resistive loss of the rotor cage is given by

$$P_{\mathrm{rt}}^{\mathrm{res}} = \frac{1}{T} \int_T \left(\int_V -\boldsymbol{J} \cdot \frac{\partial \boldsymbol{A}}{\partial t} \mathrm{d}V \right) \mathrm{d}t = \frac{1}{T} \int_T \left(\sum_{n=1}^{Q_{\mathrm{R}}} l_{\mathrm{Fe}} \sigma \int_{S_n} \left(\frac{\partial A}{\partial t} \right)^2 \mathrm{d}S \right) \mathrm{d}t \tag{3.68}$$

where Q_{R} stands for the number of rotor bars, n is a rotor bar index, σ is the conductivity of the rotor bar material and S_n is the cross-sectional area of the n-th rotor bar.

The stator hysteresis loss $P_{\mathrm{st}}^{\mathrm{hys}}$ in (3.61) is computed from the stator hysteresis loss density (3.47) or (3.48) by carrying out the integration over the stator core volume.

3.5 Hysteresis torque

Hysteresis loss in the rotor core of an induction motor produces torque much in the same way as resistive loss in the rotor winding (Robertson, 1911). Despite the fact that the electrical sheets of standard induction motors have small losses and therefore the hysteresis torque is small, rotor hysteresis may cause noticeable effects in modern control drives (Wieser and Lechner, 1996). In an ideal fundamental wave machine, the hysteresis torque is directly proportional to the hysteresis loss of the rotor. Under such an assumption, the measurement of the hysteresis torque (Arkkio et al., 1998) provides an opportunity to quite reliably verify the method of field analysis with a vector hysteresis model and the computation of the hysteresis loss.

In Section 3.1.3 on page 44 the simplifying assumption of a single-valued function and a subsequent exclusion of the hysteresis loss from the magnetic field analysis in the rotor was introduced. This simplifying assumption is not valid in the following text, where the computation of the hysteresis torque is described. Therefore, for the hysteresis torque computation purposes, the hysteresis is modeled throughout the whole core region included in the analysis.

3.5.1 Numerical Computation

The method of analysis developed in Section 3.2 is generally applicable to any 2D machine geometry. If windings are present, the circuit equations are considered together with the field equation. Consider now a geometry consisting of the rotor cross-section of an induction motor. This geometry, that is, the rotor cross-section only, has been used for the computation of the hysteresis torque. Since no stator is present in the geometry, the circuit equations do not have to be considered. The analysis of the hysteresis torque is based on the computation of the core loss, which is induced in the laminated rotor of an induction motor when subjected to a rotating magnetic field. The rotating field is created by imposing a sinusoidal flux with constant amplitude on the outer surface of the air gap. This flux then rotates around the rotor periphery at a constant speed. The fundamental wave of the flux is considered only. Since a 2D model is assumed, the eddy currents in the laminated core are not taken into account. Moreover, the currents flowing in the rotor bars are disregarded and the bars are modeled as air.

Since only the rotor is considered and all conductivities are equal to zero, Equation (3.5) reduces to

$$\nabla \times \mathcal{J}_{\mathrm{r}}^{\mathrm{v}}\left(\nabla \times \boldsymbol{A}\right) = 0 \tag{3.69}$$

where the nonlinear function $\mathcal{J}_{\mathrm{r}}^{\mathrm{v}}$ is defined as

$$\mathcal{J}_{\mathrm{r}}^{\mathrm{v}}\left(\boldsymbol{B}\right) = \begin{cases} \nu_0 \boldsymbol{B} & \text{in magnetically linear regions} \\ \\ \mathcal{H}^{\mathrm{v}}\left(\boldsymbol{B}\right) & \text{in magnetically nonlinear hysteretic regions} \end{cases} \tag{3.70}$$

with $\mathcal{H}^{\mathrm{v}}$ representing a vector hysteresis model. It is important to note that, in contrast to $\mathcal{J}^{\mathrm{v}}$ as defined by (3.2) on page 45, the function $\mathcal{J}_{\mathrm{r}}^{\mathrm{v}}$ (3.70) is defined in the linear and hysteretic regions only. Therefore, there are no single-valued regions in the considered finite element mesh of the rotor cross-section used for the hysteresis torque calculation purposes and the hysteresis is modelled everywhere in the rotor core as suggested by (3.70).

In order to ensure the rotating sinusoidal flux on the periphery of the rotor, the vector potential must satisfy the following boundary condition

$$A_{\mathrm{b}}\left(t, \varphi\right) = \hat{A}_{\mathrm{b}} \sin\left(p\varphi - \omega_{\mathrm{e}} t\right) \tag{3.71}$$

where A_{b} is the z-component of the vector potential on the boundary

t is time

φ is the angle of the particular point on the boundary

$\hat{A}_{\mathrm{b}}$ is the peak value (amplitude) of A_{b}

p is the number of pole pairs of the motor

ω_{e} is the electrical angular frequency

The amplitude of the vector potential on the boundary $\hat{A}_\mathrm{b}$ has been computed from

$$\hat{A}_\mathrm{b} = \frac{r}{p}\hat{B} \tag{3.72}$$

where $\hat{B}$ is the amplitude of the fundamental flux density component in the air gap and r is the radius of the boundary circle. The value of $\hat{B}$ has been determined from the time-stepping analysis of the motor, in which the hysteresis was neglected, and the iron core was modeled using a single-valued ***B*-*H*** relationship.

The solution to (3.69) is obtained in the same way as the solution to (3.5), that is by combination of FEM and B-FPT as was described in the previous sections. By discretizing Equation (3.71) in time, a sequence of quasi-static boundary conditions is obtained. Equation (3.69) is then solved in each discrete time step, always subject to new boundary conditions. After completing one time step, the vector hysteresis model is updated and the procedure moves to next time step.

Since the eddy-current and excess losses are excluded from the analysis, the loss induced in the rotor represents the hysteresis loss. It is denoted by $P_\mathrm{vhm}^\mathrm{hys}$ and computed from Equation (3.47) or (3.48) by carrying out the integration over the rotor core volume. In order to distinguish this loss from the hysteresis loss of the rotor computed by a single-valued function $p_\mathrm{rt}^\mathrm{hys}$ (3.54), the subscript $_\mathrm{vhm}$ is used, indicating that the particular loss $P_\mathrm{vhm}^\mathrm{hys}$ has been computed by means of the vector hysteresis model.

The existing power balance in the modeled system

$$P_\delta^\mathrm{in} = P_\mathrm{vhm}^\mathrm{hys} \tag{3.73}$$

relates the hysteresis loss $P_\mathrm{vhm}^\mathrm{hys}$ to the input air-gap power P_δ^in associated with the electromagnetic torque T_e

$$P_\delta^\mathrm{in} = w_\mathrm{m}\frac{1}{T}\int_T T_\mathrm{e}\,\mathrm{d}\,t \tag{3.74}$$

and allows computing the hysteresis torque in two separate ways, thus testing the numerical models. The hysteresis torque T_h is given by

$$T_\mathrm{h} = \frac{pP_\mathrm{vhm}^\mathrm{hys}}{\omega_\mathrm{e}} \tag{3.75}$$

The computational procedure described above has been applied for the hysteresis torque estimation of a test induction motor. The results of the simulations are reported in Chapter 4, in which a comparison to the measured hysteresis torque is also provided. The experimental retrieval of the hysteresis torque is briefly outlined in the following.

3.5.2 Measurement

Experimental retrieval of the hysteresis torque was carried out by a procedure described by Arkkio et al. (1998). The measuring set-up along with the list of devices used in the measurements is presented in Appendix E. The issues related to the accuracy of the measurements are discussed in Section 4.4.

In this measurement, a test cage induction machine is driven by a wound-rotor machine (Fig. 3.2). The stator winding of the wound-rotor machine is supplied from the same 50 Hz sinusoidal voltage source as the test induction machine. The rotor winding of the wound-rotor machine is excited from a power amplifier, which, in connection with an arbitrary waveform generator, allows a voltage supply of very small frequencies. Thus, a rotation of the test induction machine at a series of very small exact slips is easily achieved. The rotor of the test

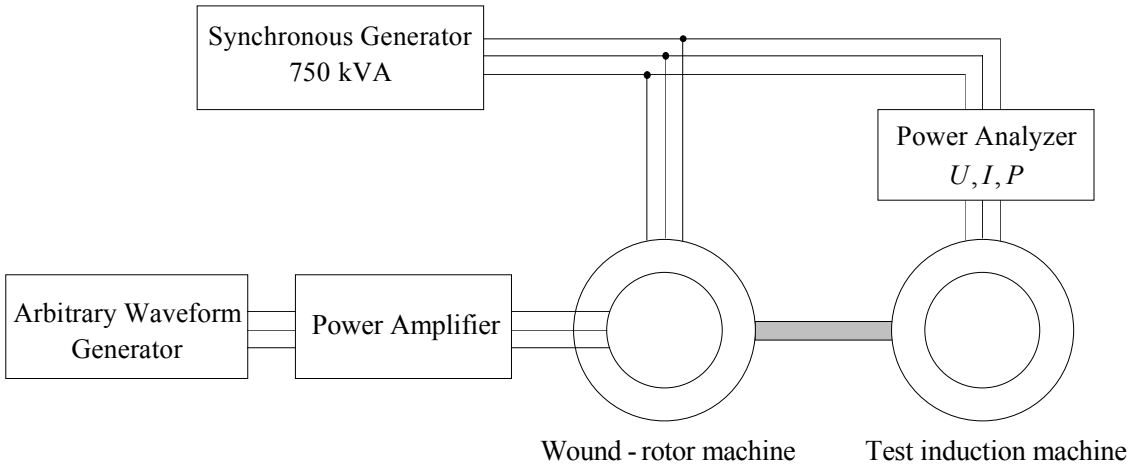

Fig. 3.2. A cage-induction motor hysteresis torque and core loss measuring set-up.

induction machine rotates a little slower than the stator field (positive slips) or a little faster that the stator field (negative slips). After a certain time period (2000 seconds in the case of a 4-pole machine for the rotor voltage frequency of 1 mHz), the rotor makes one revolution less or more than the stator rotating field. The power taken by the test induction motor is measured by a power analyzer during that time period, which actually corresponds to one relative revolution of the rotor with respect to the stator field.

An example of the measured power for a 37 kW induction motor (Appendix D) is shown in Fig. 3.3 for the rated voltage of 400 V and the positive and negative slips of 0.002 percent as a function of the rotor angle, which represents the relative position of the rotor with respect to the stator field. Owing to the magnetic anisotropy of the rotor core that causes reluctance torque, the power taken by the induction machine fluctuates. The average power is computed for both the slips, which is represented in Fig. 3.3 as a dashed line.

This procedure is performed for several small positive (motoring action) and negative (generating action) slips, which enables drawing a power versus slip curve. An example of such a measured curve is shown in Fig. 3.4, where the curve is drawn for the rated voltage. The black dots stand for the average powers taken by the induction motor, determined for each particular slip by the procedure described in the previous paragraph.

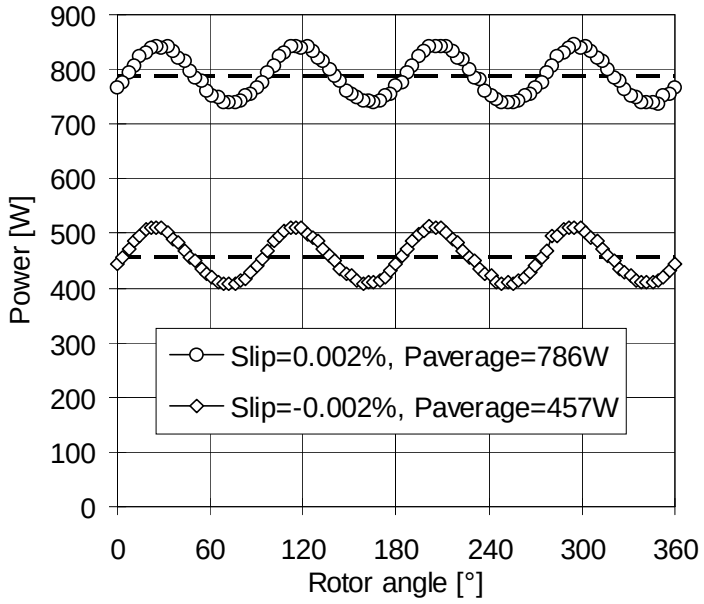

Fig. 3.3. The input power of the cage induction motor measured as a function of the rotor angle, which represents the relative angle of the rotor with respect to the stator field. The power is shown at two slips of opposite signs. The dashed lines represent the average powers for the positive and negative slips, respectively.

In order to get the input power to the motor at zero slip (synchronous speed), the linear extrapolation is used on both sides, which results in the powers shown as white dots in Fig. 3.4. It is apparent that there is an abrupt change in the power when passing the synchronous speed from motor operation to generator operation or vice versa. This step change in the power is associated with the power drop caused by the hysteresis torque, which changes its direction when passing the zero slip. For the particular case shown in Fig. 3.4 and corresponding to the rated voltage, the change in the measured power is 210 W, which corresponds to the hysteresis torque of 0.67 Nm.

It is believed that the method of measurement outlined above gives quite reliable hysteresis torque values for verifying the method of analysis. Naturally, better accuracy would be obtained in test rigs specially designed for measuring the hysteresis losses. Nevertheless, the method described above gives the possibility to study the phenomena associated with hysteresis in the geometry of an induction motor together with the real, complicated time variation of the magnetic field.

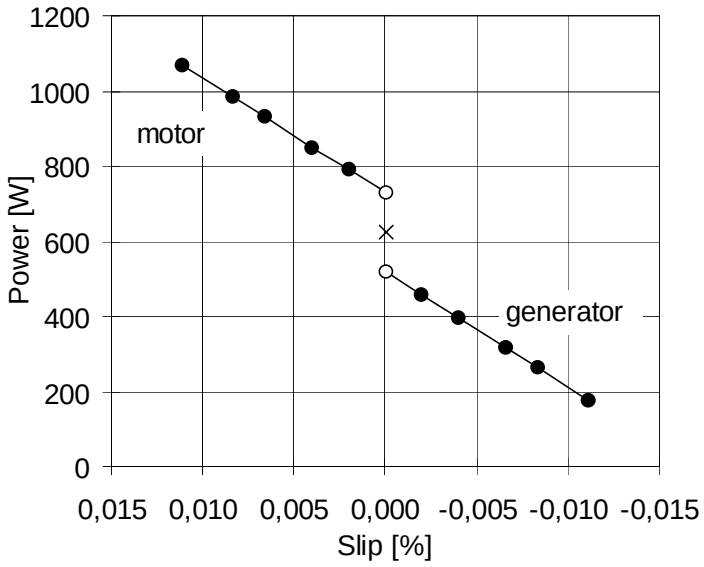

Fig. 3.4. The average power taken by the cage induction motor as a function of the slip. The drop in the power at zero slip is caused by the hysteresis torque of 0.67 Nm. The cross represents the input power of the motor after subtracting the power drop associated with the hysteresis torque. The power characterized by the cross is the sum of the core and resistive losses of the motor.

Core loss measurement

The method for experimentally determining the hysteresis torque as discussed above can be conveniently used for estimating the core loss. In fact, subtracting (adding) the power corresponding to the hysteresis torque from (to) the power obtained by the extrapolation of the measured powers to zero slip for motor (generator) operation, the average power loss taken by the induction motor at synchronous speed is obtained. The value of this power for the particular case of the rated voltage is 623 W, indicated in Fig. 3.4 by a cross. This power represents the sum of the core and resistive losses of the test motor running at synchronous speed.

The entire measuring process described above was repeated for different values of the supply voltage amplitudes. In this way the total power loss versus the supply voltage curve was constructed and it is shown in Fig. 3.5 in the form of white dots. Subtracting the resistive stator loss from the total measured losses, the core loss is acquired, represented in Fig. 3.5 by black triangles.

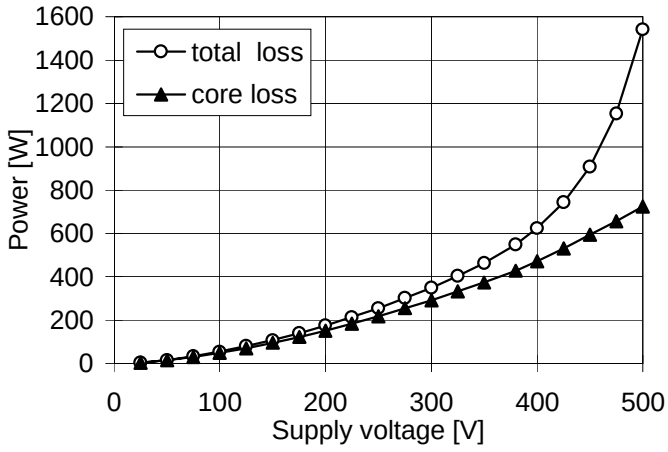

Fig. 3.5. The measured total and core losses of the cage induction motor as functions of the supply voltage. The total loss represents the sum of the resistive loss and the iron core loss. The core loss is obtained by subtracting the resistive stator loss from the total losses. Thus, the measured core losses include also the resistive rotor losses.

4 Results

This chapter reports the results obtained by the computational models and procedures described in Chapters 2 and 3. The structure of the chapter is organized as follows: Section 4.1 introduces the parameters of the hysteresis and core loss models used; Section 4.2 discusses the verification of the hysteresis model and presented numerical techniques; Section 4.3 reports the results of the application of the proposed techniques to three individual test induction motors, and Section 4.4 discusses the results from the point of view of the solution times and accuracy.

4.1 Hysteresis model and core loss model parameters

As discussed in Section 2.2, the only function needed to identify the hysteresis model is the upper branch of the limiting hysteresis loop $H_{\mathrm{lim}}^{\mathrm{s}}$. This function has been obtained by performing a DC-field measurement (Appendix B) on a ferromagnetic wound-ring sample (Appendix A). The measured upper branch of the limiting hysteresis loop for the considered ferromagnetic material is shown in Fig. 4.1. The remanence is 0.56 T and the coercive force is 60 A/m.

The parameters for modeling the magnetization curve towards saturation, introduced in Section 2.2.2, are summarized in Table 4.1.

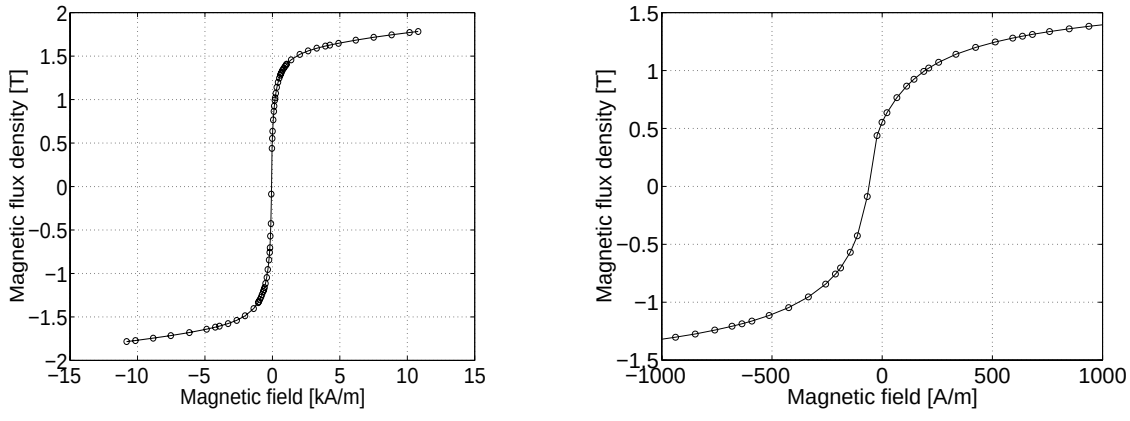

a) *b)*

Fig. 4.1. The measured upper branch of the limiting hysteresis loop of the considered ferromagnetic material (a) and an enlarged view near the zero magnetic field. These data have been used to identify the hysteresis model according to the identification procedures described in Chapter 2.

TABLE 4.1. PARAMETERS OF THE HYSTERESIS MODEL OF THE CONSIDERED FERROMAGNETIC MATERIAL FOR MODELLING THE MAGNETIZATION CURVE CLOSE TO SATURATION.

parameter	value
H_z [A/m]	10 811
B_z [T]	1.78
H_s [A/m]	150 000
B_s [T]	2.2
μ_z [H/m]	$15.2\,\mu_0$
H_0 [A/m]	13 735

Fig 4.2 shows a modeled saturated symmetric *B*-*H* loop. The loop has been obtained by means of the hysteresis model in the hysteretic part of the *B*-*H* relationship and by using the analytical function represented by Equation (2.15) with the parameters from Table 4.1 in the single-valued part of the *B*-*H* relationship.

Recalling the simplifying assumptions of the no-load motor analysis from Section 3.1, the nonlinearity of the rotor core is modeled by a single-valued function. This function is represented here by an anhysteretic curve of the considered ferromagnetic material, approximated as an average of the upper and lower branches of the limiting hysteresis loop. If the hysteresis in the stator core is replaced by a single-valued function in order to compare the core loss computation between the conventional and presented approaches, the nonlinearity of the stator core is also modeled by the same nonlinear single-valued function.

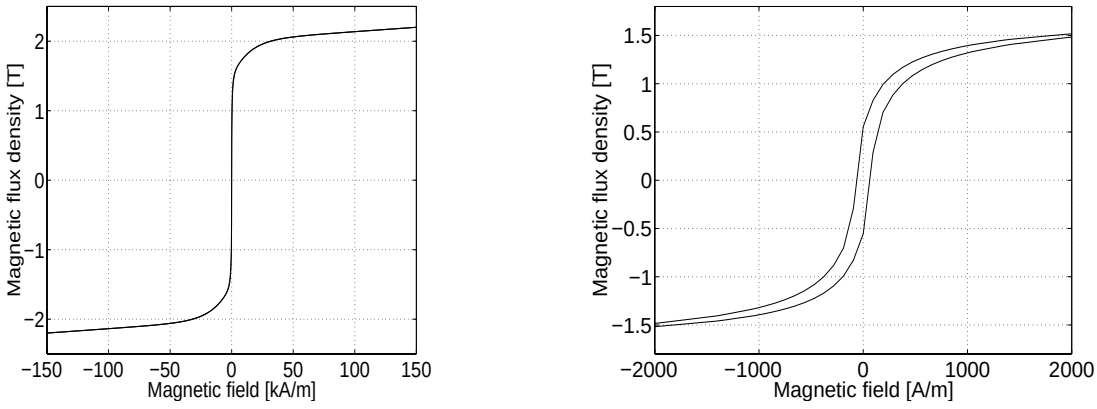

a) *b)*

Fig. 4.2. The simulated highly saturated symmetric hysteresis loop (a) and an enlarged view near the zero magnetic field (b).

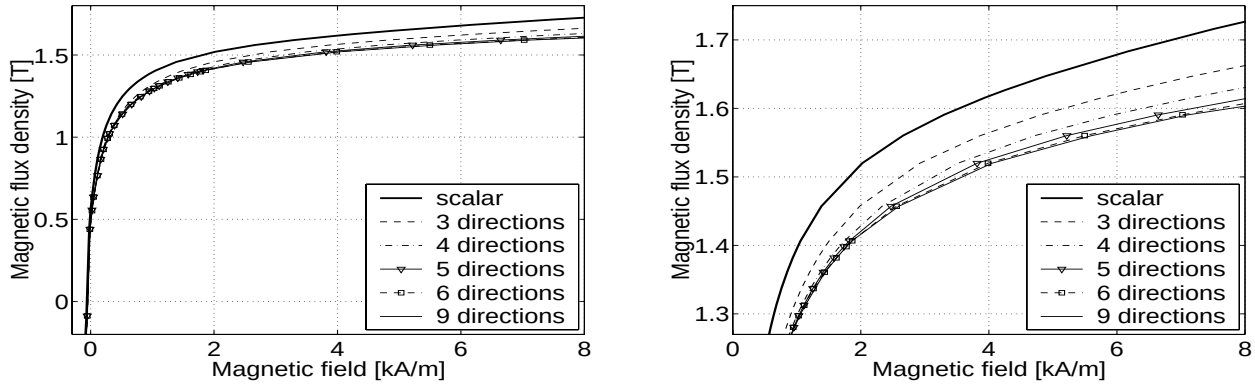

Fig. 4.3. The computed limiting curves of scalar models working under vector models of different directions (a) and an enlarged view (b).

Regarding the vector model, the limiting curve of the scalar model working under the vector model $H_{\text{lim}}^{\text{s-v}}$ has been determined from the measured $H_{\text{lim}}^{\text{s}}$ according to the procedure described in Section 2.3.2. The limiting curve $H_{\text{lim}}^{\text{s-v}}$ has been computed for several directions of the vector model. An example of $H_{\text{lim}}^{\text{s-v}}$ for 3, 4, 5, 6 and 9 directions is shown in Fig. 4.3 along with the original scalar limiting curve $H_{\text{lim}}^{\text{s}}$. In order to see the differences between the vector limiting curves of different directions, the curves are shown for positive values of the magnetic field only (Fig. 4.3 a) and an enlargement is also provided (Fig. 4.3 b). It is clear from Fig. 4.3 that after the number of directions of the vector model reaches 6, the vector limiting curve practically does not change. From this point of view, the recommended number of directions seems to be 6.

The core loss coefficients have been determined according to the procedure described in Section 3.3.5. The obtained coefficients, which were used for the empirical core loss evaluation through the formulae presented in Section 3.3, are summarized in Table 4.2.

TABLE 4.2. COEFFICIENTS OF THE EMPIRICAL CORE LOSS MODEL.

Coefficient	C_{hys}	n_{hys}	C_{class}	C_{exc}
Value	243	1.71	1.0	0.86

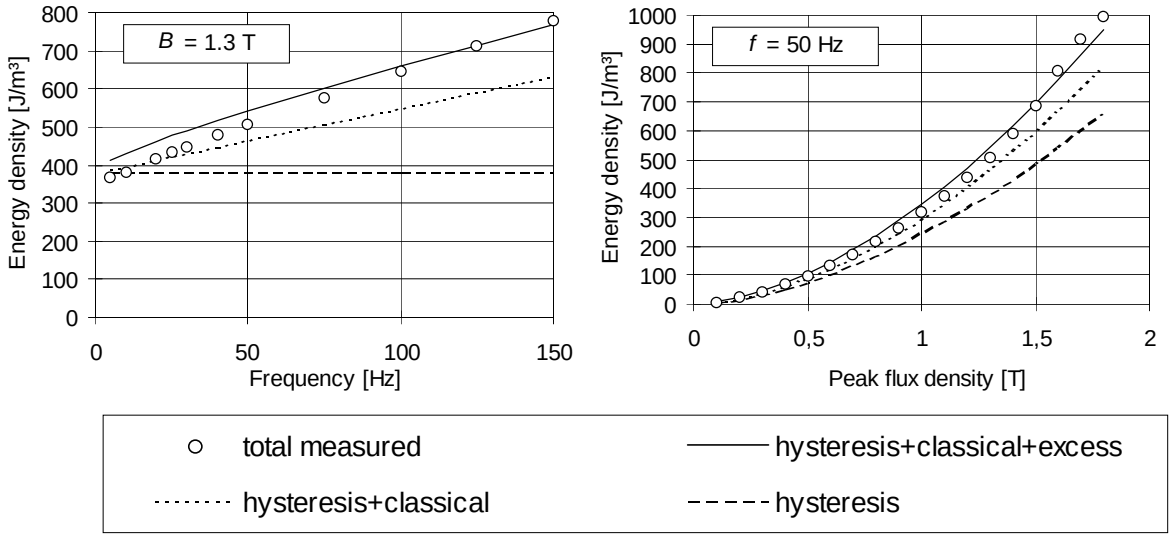

a) *b)*

Fig. 4.4. Separation of the core losses on the wound-ring sample. The losses are shown as functions of the frequency under sinusoidal flux density of 1.3 T peak value (a) and as functions of the peak flux density for frequency of 50 Hz (b). The solid and broken lines represent the computed losses using the empirical model with the coefficients from Table 4.2. The single white circles represent the total measured core losses.

An example of the core loss separation performed on the test wound-ring sample is depicted in Fig. 4.4, where the empirically computed and measured core losses are shown as functions of the frequency and peak flux density. In both cases the correspondence between the measured and empirically evaluated core losses is tolerable with the relative error of no more than 13%.

The considered ferromagnetic material, whose main nonlinear and core loss features have been presented above, is used from this point forward in all presented applications. As regards the simulations of motors, the same material has been used to model the iron cores of all three studied motors. However, the actual material of the studied motors is unfortunately not exactly known, which should be kept in mind when comparing the calculated and measured results.

4.2 Verification of numerical models

4.2.1 Scalar hysteresis model verification

The scalar model is verified by a direct comparison of its outputs to the DC-field measurements performed on the wound-ring sample for different symmetric and unsymmetric hysteresis loops and branching. The computed and measured hysteresis loops are reported in Fig. 4.5.

Fig. 4.5 a) shows a symmetric hysteresis loop with the peak flux density of 1.35 T. A certain minor discrepancy can be observed, especially near the turning points of the loop. A comparison between the computed and measured minor loops is presented in Fig. 4.5 b). The *B-H* tracing starts from the point of zero magnetic field and remanent flux density. The magnetic field in A/m approximately imitates the following pattern 0 > 500 > -200 > 50 > -50 > 500, whereby two minor loops are created. The error is present particularly in the modeling

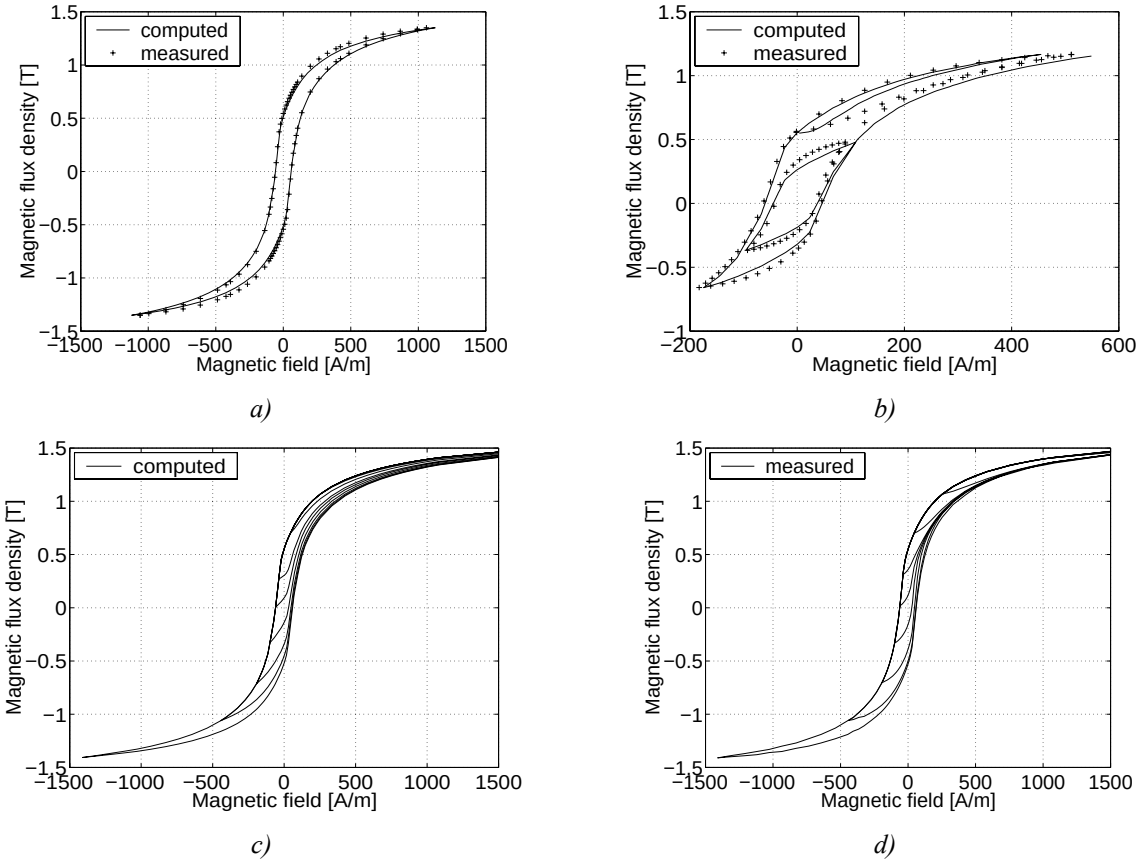

Fig. 4.5. Comparison between computed and measured hysteresis branching: a) symmetric hysteresis loop with the peak magnetic flux density of 1.35 T, b) hysteresis branching with minor loops, c) and d) first order reversal curves.

of the first upper minor loop; otherwise the correspondence is relatively good. The computed and measured first-order reversal curves are shown in Fig. 4.5 c) and d) respectively. Similarly as observed in Fig. 4.5 c), regarding the small minor loops for which the turning value of the magnetic field is larger than zero, the disagreement is generally worse than for the remaining reversal curves. Despite the discrepancies revealed in Fig. 4.5, this simplified Preisach model gives predictions that agree reasonably well with the experiments, and therefore it is qualified for the FEM implementation. For even better accuracy, identifying the model by using the first-order reversal curves should be performed. It would certainly be interesting to see the comparison between these two approaches; however, this is beyond the scope of this work, but may be performed and reported in the future.

4.2.2 Vector model and numerical technique verification

A natural way to verify a vector hysteresis model is undoubtedly to perform the measurements under the rotating field, for example, by making use of a single-sheet rotational core loss tester (Zhu and Ramsden, 1993b). Since such equipment has not been available, other ways of verifying the vector model had to be found. First of all, a comparison between the vector model applied along one direction and the scalar model is reported. After that, the verification of the hysteresis model is based on the computation of the hysteresis torque and associated losses in a simplified geometry of a 37 kW test induction motor (Appendix D) and their comparison with measurements. The slotless and slotted rotor structures are investigated as laminated ferromagnetic bodies subject to a rotating magnetic field. The first-order finite element mesh used for the calculations corresponds to the rotor mesh of the 37 kW test induction motor shown in Fig. F2 in Appendix F.

Vector model applied along one direction

A test of the prepared vector model, in which the input to the vector model has been restricted to vary only along one direction, is shown in Fig. 4.6. A set of first-order reversal curves has been chosen for the comparison between the output from the vector and scalar models. The vector model consisted of three (a) and six (b) scalar models (directions). In both the reported cases the agreement is satisfactory.

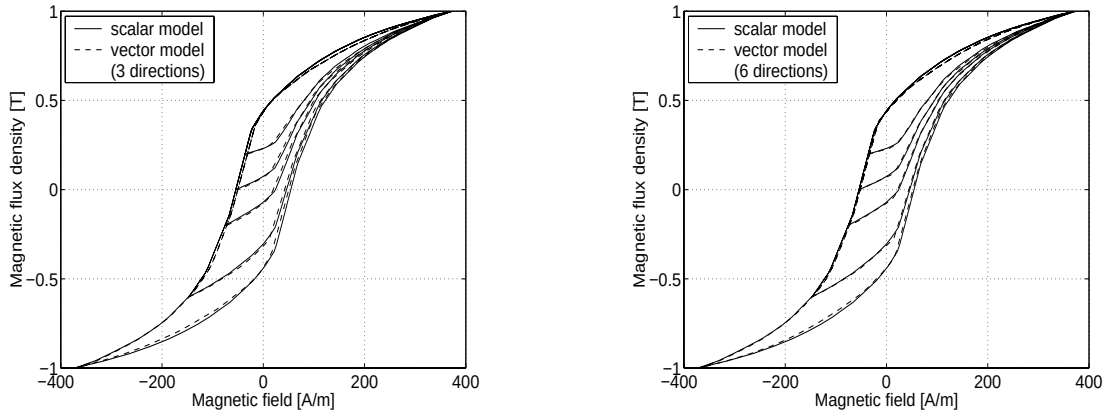

a) *b)*

Fig. 4.6. Comparison of minor loop computations between the scalar model and the vector model with a) 3 directions and b) 6 directions applied along one direction.

Slotless rotor geometry

The numerical technique described in Section 3.5 has been applied to a geometry consisting of a slotless rotor of a 37 kW induction motor. Such a simplified geometry has been chosen in order to eliminate the torque ripple caused by slotting from the analysis. The verification of the numerical technique comprising the vector hysteresis model is based on the power balance (3.73) existing in the model system. The hysteresis loss (3.47) and the input air-gap power (3.74) are computed and compared.

As an example, a simulation with 50 time-steps per electrical period is reported, with the amplitude of the fundamental flux density component corresponding to a voltage of 400 V. Two electrical periods were computed, starting from the zero field as an initial state. The computations were carried out for vector hysteresis models with several different directions.

It was observed that the computation with more than 50 time-steps did not significantly influence the results.

The time variation of the torque is shown in Fig. 4.7 a) for the vector model of 2, 3, 4 and 6 directions. Since a slotless geometry is considered, with the fundamental wave of the flux in the air gap, the time variation of the torque is expected to be smooth. It is clear from Fig. 4.7 a) that the simulation with 2 directions is unable to correctly predict that behavior, because ripple occurs in the torque. Naturally, the more directions the smoother the torque becomes, as seen from the curve corresponding to the simulation with 6 directions.

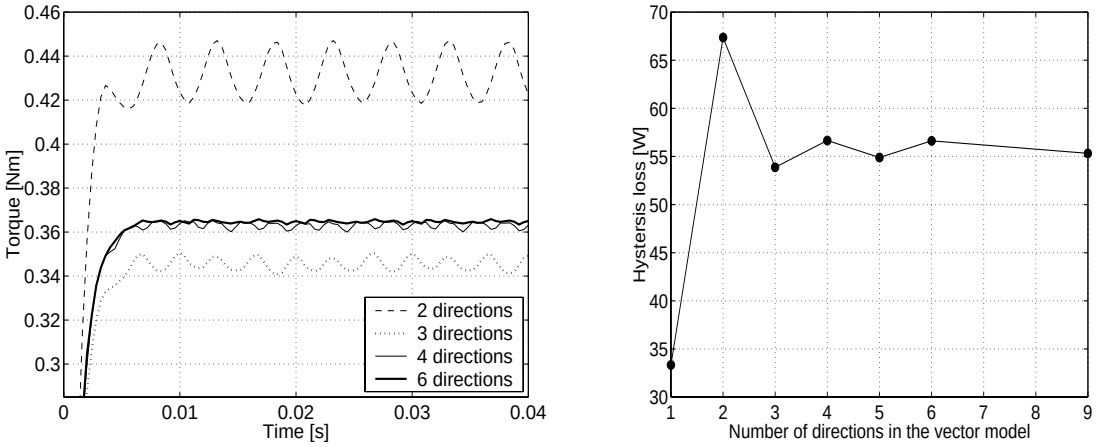

a) *b)*

Fig. 4.7. Results of the simulation for the slotless geometry: a) The electromagnetic torque as a function of time. (b) The hysteresis loss as a function of the number of directions in the vector model.

After reaching the steady state, the hysteresis loss is determined from Equation (3.47) and eventually separated into alternating and rotational components according to (3.48). The computed hysteresis loss is reported in Fig. 4.7 b) as a function of the number of directions in the vector model. An oscillatory convergence to a certain value is evident. This graph is important for suggesting the optimal number of directions in the vector model, related to the prediction of the hysteresis loss. Clearly, a vector model with 1 and 2 directions is not recommended. A vector model with more than 6 directions seems to be unreasonable as well. In order to be on the safer side, that is to rather predict a little higher than lower losses, an even number of directions may be recommended. Thus, the choice has to be made between 4 and 6 directions. The smoother torque and better hysteresis loss computation accuracy suggest 6 directions. However, since the difference between the computed hysteresis loss for 4 and 6 directions is only marginal, 4 directions seems to be a fair trade-off. In any case, 6 directions seems to be sufficient from the smooth hysteresis torque and hysteresis loss computation accuracy points of view.

The computed power balance (3.72) for the slotless geometry simulation is reported in Table 4.3. The percentage error is related to the input power. The numbers presented show that the accuracy of the proposed numerical technique is satisfactory.

TABLE 4.3. POWER BALANCE AS A FUNCTION OF THE NUMBER OF DIRECTIONS IN THE VECTOR MODEL FOR THE SLOTLESS GEOMETRY SIMULATION.

Number of directions:	1	3	4	6	9
Input power [W]	34.41	54.27	57.03	57.02	55.71
Hysteresis loss [W]	33.34	53.88	56.66	56.62	55.33
Error [W]	1.07	0.39	0.37	0.40	0.38
Error [%]	3.11	0.72	0.65	0.70	0.68

Realistic slotted rotor geometry

Applying the numerical procedure to a realistic rotor geometry allows a comparison of the computed hysteresis torque with the hysteresis torque obtained experimentally, as described in Section 3.5.2. In the simulation, an electrical period was divided into 50 time-steps and the number of directions in the vector model was set to 6. Similar to the slotless geometry, two electrical periods were computed starting from the zero field as an initial state. As an example, the computed electromagnetic torque for the amplitude of the fundamental flux density component corresponding to 400 V is shown in Fig. 4.8. In contrast to the rather smooth torque for 6 directions in the slotless case (Fig. 4.7 a), the computed torque exhibits ripple caused by the slotting of the rotor. Although the slots in the studied geometry are closed, at higher voltages the iron bridges above the slots saturate and the slots become magnetically 'visible' from the air-gap side, which causes the ripple in the torque.

Similar computations have been carried out for voltages ranging from 50 up to 500 V. The hysteresis loss induced in the rotor and subsequently the corresponding hysteresis torque

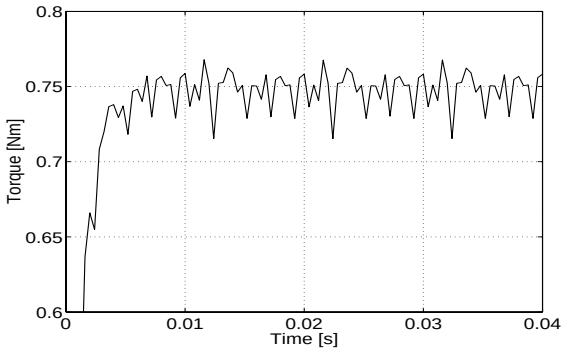

Fig. 4.8. The electromagnetic torque as a function of time in the simulations with the realistic slotted rotor and the amplitude of the fundamental flux density wave corresponding to 400 V.

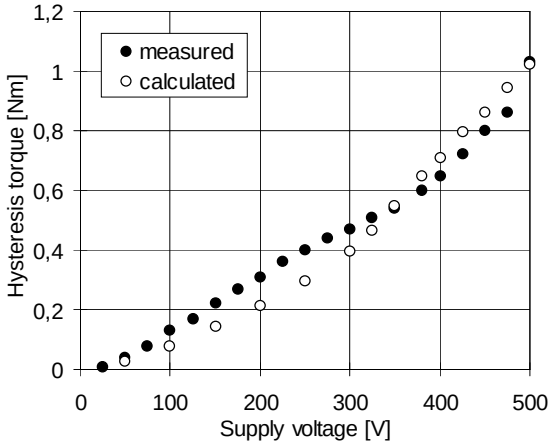

Fig. 4.9. The computed and measured hysteresis torque as a function of the supply voltage for a 37 kW induction motor. As a reference, the rated torque of the motor is 240 Nm.

have been computed and compared with the measured results. This comparison is shown in Fig. 4.9. At small supply voltages, the method of analysis gives too small values of the hysteresis torque. At higher voltages, the calculated torque grows a little faster with the increasing voltage than the measured torque. According to Fig. 4.10, which shows the loss distribution caused by the alternating (a) and rotational (b) fields, the fast growth of the hysteresis torque at the highest voltages is associated with the alternating losses in the teeth, and the rotational losses in the yoke.

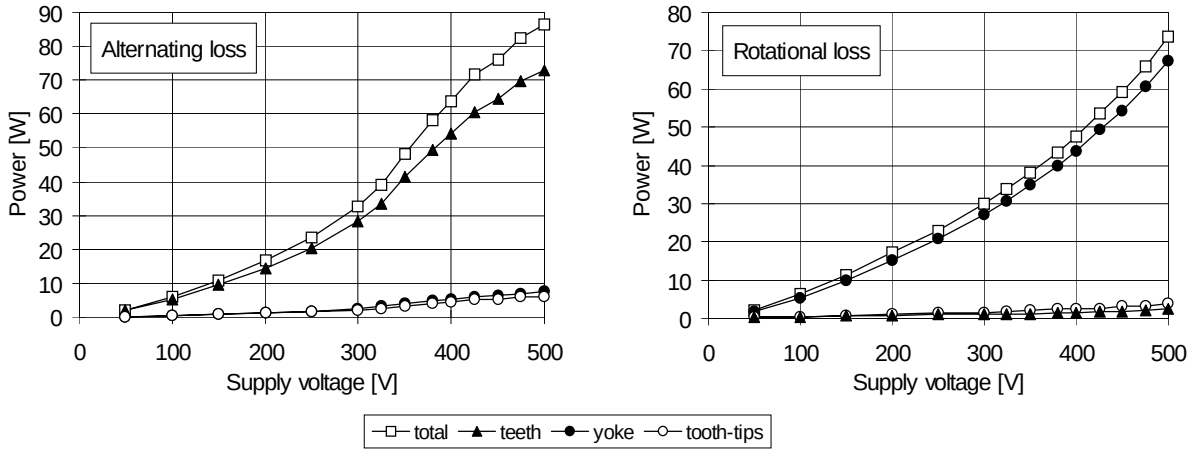

a) *b)*

Fig. 4.10. The computed hysteresis loss in different parts of the studied rotor geometry as a function of the supply voltage. The hysteresis loss is separated into a) alternating and b) rotational components.

4.3 Application to induction motors

4.3.1 Test motors

The main parameters of three individual induction machines used in the simulations and measurements are given in Table D1 in Appendix D. The cross-sectional geometries of the test machines in a plane perpendicular to the shaft are shown in Appendix F. All the test machines had unskewed rotor bars.

The geometries of 37 and 315 kW motors consist of four symmetry sectors with identical geometries. There are two symmetry sectors with identical geometries in the case of the 30 kW motor. Obviously, it is enough to analyze one of the sectors, called the solution sector, which spans one pole pitch.

Symmetry sectors and associated boundary conditions have already been discussed in Section 3.2. In accordance with what was mentioned there, it is assumed that the flux does not penetrate the outer surface of the motor. This corresponds to the zero boundary condition for the magnetic vector potential on the outer surface of the solution sector. The potential on the sides of the solution sector is controlled by the negative periodic boundary conditions, which means that the potential on one side of a solution sector is free to vary, and on the other side it has the same value with the opposite sign.

The finite element meshes of the solution sectors of the studied motors are depicted in Appendix F. For time-consumption reasons, when solving the field with hysteresis included, the finite element meshes are constructed from first-order triangular elements. The total number of nodes, the total number of elements and the numbers of elements covering different regions are summarized in Table 4.4. The hysteretic elements cover the stator core, the single-valued elements cover the rotor core and shaft, and the linear elements cover the stator windings, the rotor bars and the air gap.

The assumptions related to the iron core have been discussed in Section 3.1.3. In brief, the currents in the laminated core of the motor are ignored, the magnetic properties of the rotor core are approximated by a single-valued B-H curve and the magnetic properties of the stator core are accounted for through the vector hysteresis model, with the limiting curve

TABLE 4.4. THE NUMBER OF NODES AND ELEMENTS IN THE FINITE ELEMENT MESHES OF THE STUDIED MOTORS.

Parameter: Motor:	30 kW	37 kW	315 kW
Number of quadrants	2	1	1
Number of nodes	1 245	863	1 231
Number of elements	2 198	1 510	2 186
Number of hysteretic elements	540	360	576
Number of single-valued elements	702	486	622
Number of linear elements	956	664	988

shown in Fig. 4.1. The total number of vector hysteresis models corresponds to the number of hysteretic elements. As for the 37 kW motor, if the number of directions in each vector model is chosen as 6, the total number of scalar hysteresis models included in the analysis is 2 160.

In the single-valued part of the *B-H* relationship (Fig. 2.1), i.e. in a region close to saturation, a single-valued function (2.15) is used, whose main parameters are summarized in Table 4.1.

Since the principal means of verification of the proposed numerical techniques applied to electric machines is the comparison between the computed and measured no-load core losses, the magnetic field of the test motors is analyzed at no-load. The results of the no-load simulations are presented for the 37 kW motor only. In particular, the flux density variations and hysteresis loops in different motor regions as well as the core loss distribution and power balance are reported. The comparison between the computed and measured losses is summarized for all the motors. Some of the results have been presented in the following series of papers: Saitz and Arkkio (1999), Saitz (2000), Saitz et al. (2000) and Saitz (2001).

4.3.2 No-load operation

The magnetic field analysis of the 37 kW test motor is presented below. In the time-stepping analysis, the stator winding was powered from a symmetric, three-phase, 50 Hz sinusoidal voltage supply and the rotor was forced to rotate at synchronous speed. The rotation of the rotor is modeled by changing the finite element mesh in the air gap. The number of time-steps per period of supply voltage was 400, and the number of directions in the vector models was 6.

Fig. 4.11 shows the phase current waveforms of the studied motor at no-load supplied by 100 V and 400 V. The figures on the left hand side have been produced from the time-stepping computed results and the figures on the right-hand side have been prepared from the measured data. Since the slots of the rotor are closed, the current waveforms for the lower voltage supply are practically sinusoidal. As the voltage rises, the bridges over the rotor slots become saturated, the permeability in those areas decreases and therefore the rotor slotting starts to be seen from the stator side. The higher harmonics due to slotting of the rotor are present in the current waveforms. The correspondence between the computed and measured waveforms is good for the voltage of 100 V. The discrepancy is higher for the rated voltage, what is attributed to the lack of exact knowledge of the iron magnetic properties in the motor studied.

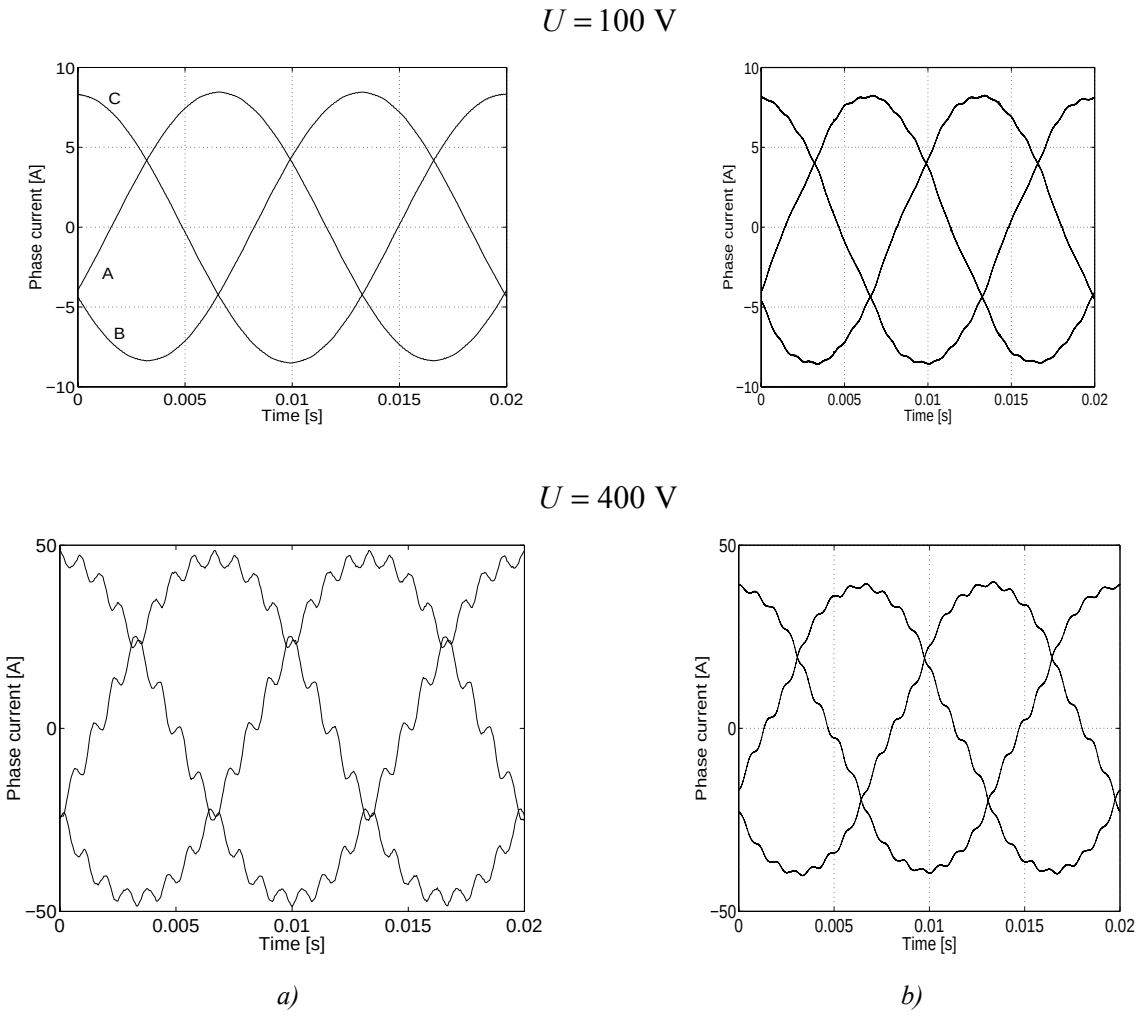

Fig. 4.11. The computed (a) and measured (b) waveforms of the phase currents of the 37 kW test induction motor running at synchronous speed and supplied by a voltage of 100 V and 400 V.

The loci of the flux density vectors and ***B-H*** relationships have been recorded for presentation at the points shown in Fig. 4.12. Since the stator core is of major interest, five points have been chosen for presentation essentially covering tooth-tip, tooth and yoke of the stator. One point has been selected in the rotor core of the induction motor studied.

Figure 4.13 shows the curves of the flux density vectors' loci in the iron core of the studied induction motor running at synchronous speed. In the stator teeth (b) as well as in the stator tooth-tips (a), the flux density variation is almost alternating. At the end of the teeth (c) and behind the slots of the stator (d) the flux density variation can no longer be considered as alternating. The rotation of the flux density vectors in these parts of the iron core is obvious. In the point near the outer surface of the stator (e), the flux density variation becomes again alternating; however, this time it alternates along the tangential direction, whereas in the teeth and tooth-tips the alternation is along the radial direction. Since first-order elements have been used in the finite element mesh, and the element in which the point (e) lies contains two nodes at the outer surface where the vector potential is fixed to zero, the variation of the flux density in this point is in fact purely alternating. The flux density vectors in the rotor tooth-tips also follow very complicated patterns (f), which are created by the combination of the rotating and DC-biased fields. The flux density in other parts of the rotor core is practically constant.

Figure 4.13 clearly indicates complex patterns, which the flux density vectors trace in the different parts of the stator and rotor iron core of an induction motor. As far as the core loss calculation of induction motors is concerned, the curves presented in this figure represent clear evidence that the simplified core loss computation methods, which assume the flux density variation to be unidirectional and sinusoidal, are not appropriate and will likely lead to inaccurate results.

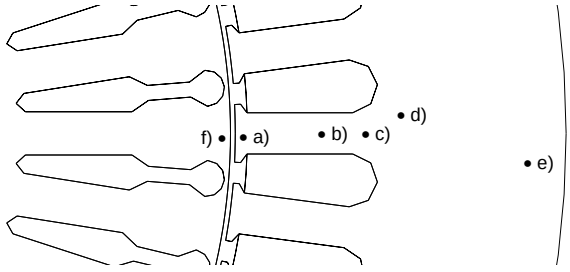

Fig. 4.12. The points for which the flux density vectors loci and B-H relationships have been recorded for presentation.

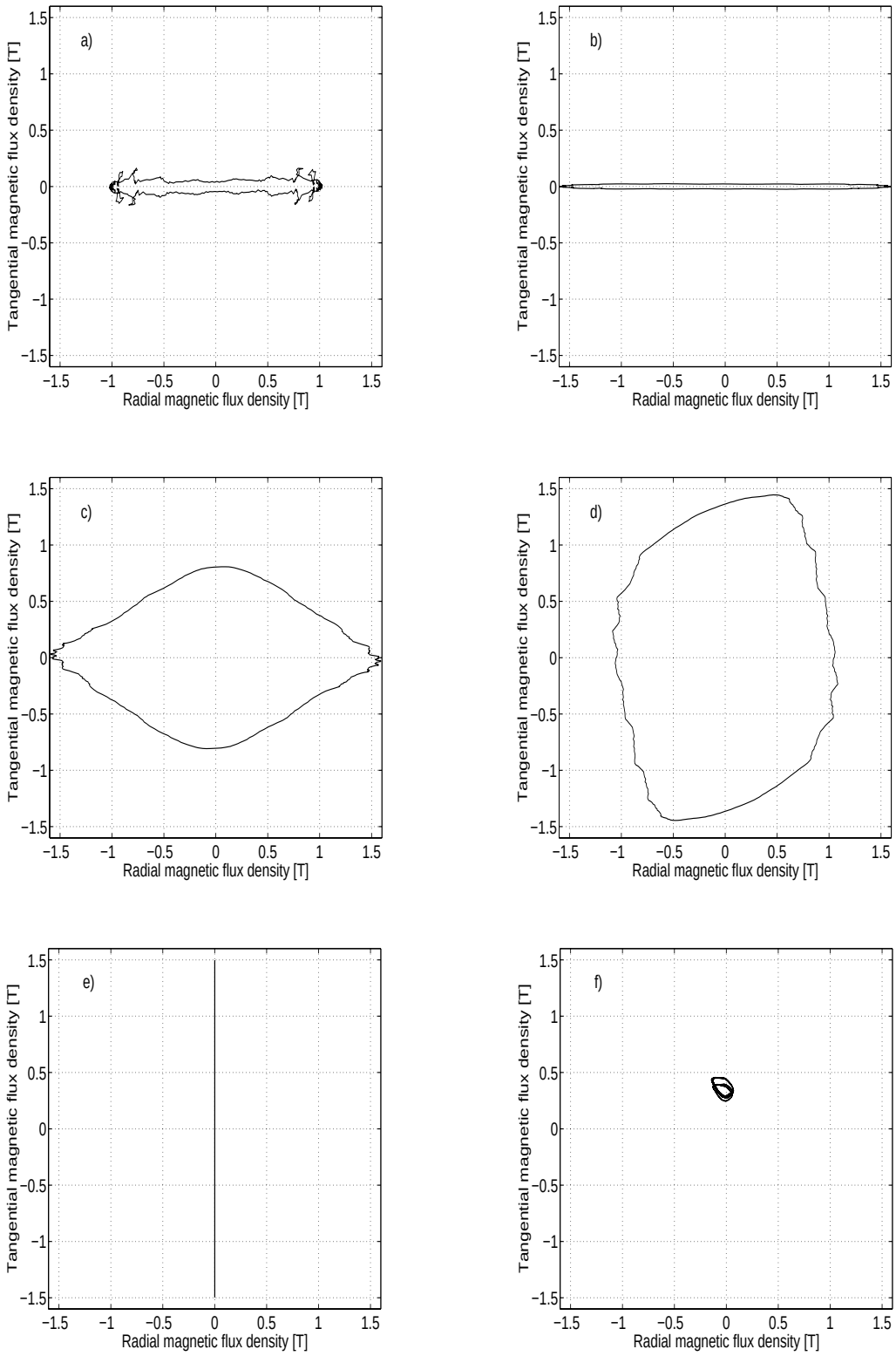

Fig. 4.13. The loci of the flux density vectors in the iron core of the studied induction motor running at synchronous speed and supplied by the rated voltage. The curves have been recorded at the points from (a) through (f) according to the sketch shown in Fig. 4.12.

The curves in Fig. 4.14 represent the *B-H* relationships at the points of the studied motor's iron core according to Fig. 4.12. As already mentioned, the magnetic field in the tooth-tips and the teeth of the stator core is practically alternating, with the variation almost

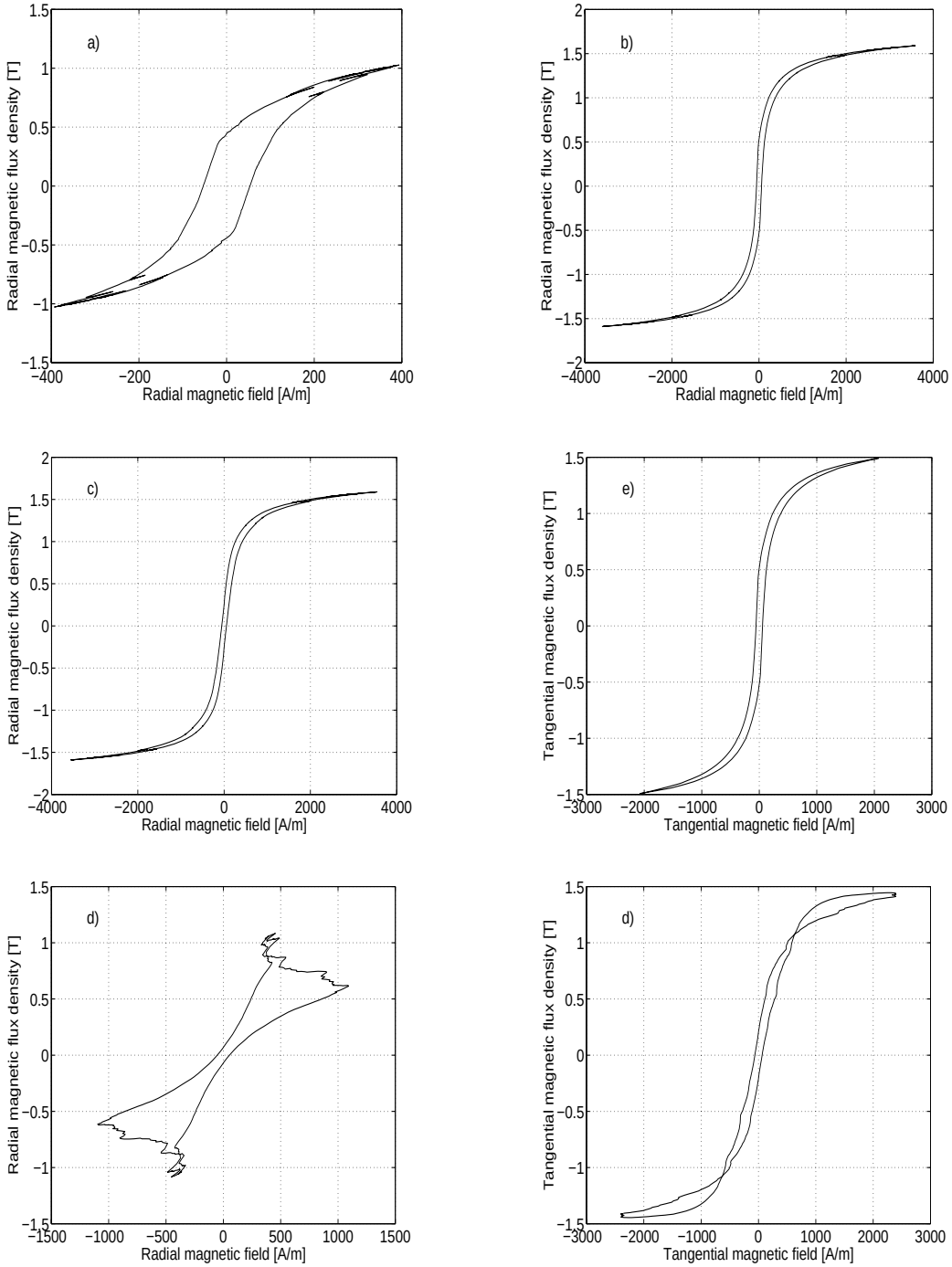

Fig. 4.14. The B-H relationships of the flux density and magnetic field radial (a)-(d) and tangential (e) components. The curves have been recorded at the points from (a) through (e) according to the sketch shown in Fig. 4.12 during the time-stepping simulation of the studied induction motor running at synchronous speed and supplied by the rated voltage.

solely in the radial direction. The *B-H* relationship between the radial components of the flux density and magnetic field (a-b) is clearly hysteretic. The variations in the tangential direction are of small magnitudes and are not shown. At the end of the teeth and behind the slots of the stator, the flux density and magnetic field vectors rotate and rotational hysteresis occurs. Nevertheless, the *B-H* relationship between the radial components of the flux density and magnetic field at the end of the teeth (c) is still a hysteresis loop of conventional shape. This obviously cannot be said about the *B-H* relationship between the radial and tangential components of the flux density and magnetic field behind the slots (d), where the rotating field effects are pronounced. Since the variation of the field near the outer surface of the stator is alternating in the tangential direction, the *B-H* relationship between the tangential components of the flux density and magnetic field is shown (e). The *B-H* relationship in the rotor is a single-valued one, modeled by the curve depicted in Fig. 4.2 b), and therefore omitted in Fig. 4.14. Instead, the time variation of the radial component of the flux density and its spectrum at point (f) of the rotor core are shown in Fig. 4.15.

As indicated above, at the end of the teeth and behind the slots of the stator, the rotation of the flux density and magnetic field vectors is pronounced. An example of this situation is

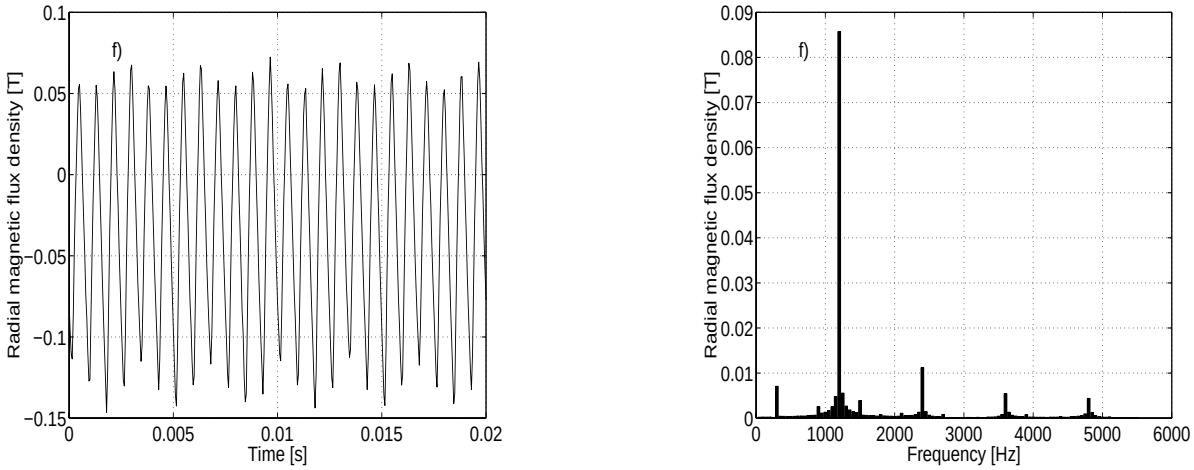

Fig. 4.15. The time variation of the radial component of the magnetic flux density and its spectrum. The time variation has been recorded at point (f) of the rotor core according to Fig. 4.12, during the time-stepping simulation of the studied induction motor running at synchronous speed and supplied by the rated voltage. The ripple in the time variation is caused by slotting of the stator. The most pronounced component of the spectrum appears at the frequency of 1 200 Hz, which corresponds to the first stator slot harmonic.

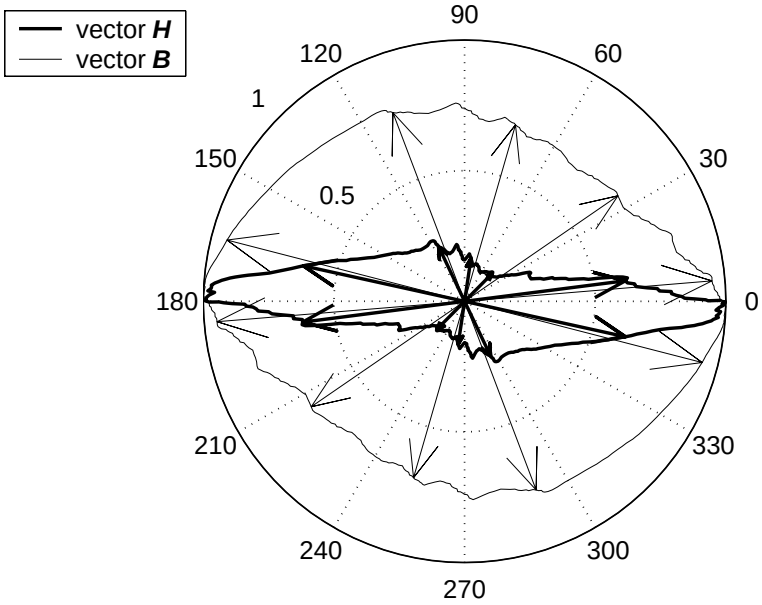

*Fig. 4.16. The loci of the magnetic field strength **H** and flux density **B** vectors traced at point (d) according to Fig. 4.12 during one period of the motor steady-state no-load operation. The vectors rotate in the counter-clockwise direction and for the sake of clarity they are normalized (Bmax=1.54 T, Hmax=2640 A/m) and shown only at 10 instants in time out of 400, into which a period of the supply voltage was discretized.*

shown in Fig. 4.16, where the loci of the magnetic field ***H*** and flux density ***B*** vectors traced at point (d) of the stator core is reported. The rotational hysteresis causes vector ***B*** to lag behind vector ***H*** by a certain time-varying angle, shown related to the angular position of vector ***H*** in Fig. 4.17.

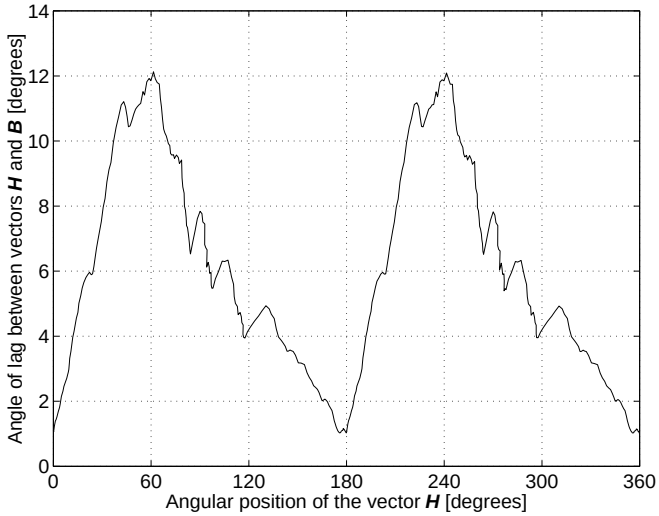

*Fig. 4.17. The angle of lag between vectors **H** and **B** at point (d) according to Fig. 4.12 during one period of the motor's steady-state no-load operation.*

4.3.3 Computed core losses and power balance

Core loss distribution

The core losses are computed according to the core loss model presented in Section 3.3 from the no-load distribution of the magnetic field and flux density in time and space. The coefficients for the empirical formulae are summarized in Table 4.1, Section 4.1.

The computed core losses in the stator of the 37 kW test motor as functions of the supply voltage are shown in Fig. 4.18 a). Apparently, the hysteresis contribution to the total stator core losses is a dominant one. The classical and excess losses are of about the same magnitude. The same situation but for the rotor is depicted in Fig. 4.18 b). The eddy-current loss (sum of the classical and excess losses) is much higher than the hysteresis loss. Owing to higher slot harmonics present in the flux density harmonic content, especially in the tooth tips (Fig. 4.15), the classical loss prevails over the excess loss.

The computed total (stator plus rotor) core losses separated into hysteresis, classical and excess losses as functions of the supply voltage are presented in Fig. 4.19 a). The major contribution to the total core loss appears to be the hysteresis loss. However, when computing

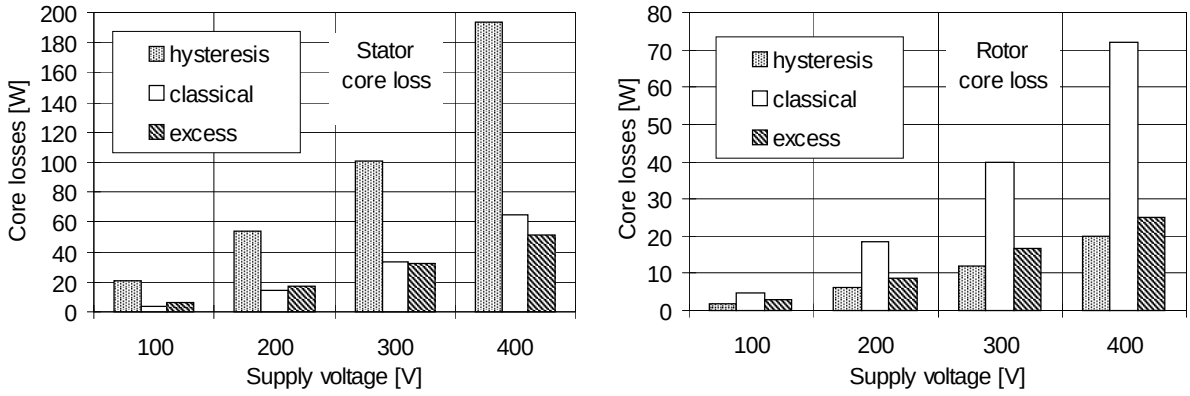

a) *b)*

Fig. 4.18. The computed core losses of the studied 37 kW induction motor in the stator (a) and rotor (b), separated into hysteresis, classical and excess losses as functions of the supply voltage. Note that the hysteresis loss in the stator is computed directly from the simulated hysteresis loops, whereas the rotor hysteresis loss is determined by using the empirical model.

the total eddy-current loss by summing the classical and excess loss contributions, it can be seen that the eddy-current loss is at least as important as the hysteresis loss. The difference between the classical and excess losses comes from the rotor part, as was explained in the previous paragraph.

The proportion of the stator and rotor core losses in per cent of the total core loss as a function of the supply voltage is shown in Fig. 4.19 b). Clearly, the major part of the total core loss is induced in the stator laminations. Regarding the rated voltage of 400 V, more than 70% of the total core loss is created on the stator side.

Figure 4.20 concentrates on the hysteresis loss in the stator core. Note that the hysteresis loss of the stator is the only loss that is included in the analysis of the magnetic field. All the other losses are not incorporated in the analysis and they are computed using empirical formulae. The separation between alternating and rotational hysteresis losses is presented and the distribution of these losses in main parts of the stator core as functions of the supply voltage is given. The major part of the alternating and rotational hysteresis losses comes from the yoke contribution. The tooth-tip contributions are not of significant magnitude, because closed rotor slots reduce the flux density harmonic content on the stator side. Regarding the rotational loss, the yoke contribution is the only important contribution. Apart from the yoke, about half of the alternating loss is induced in the teeth. Another important point arises from

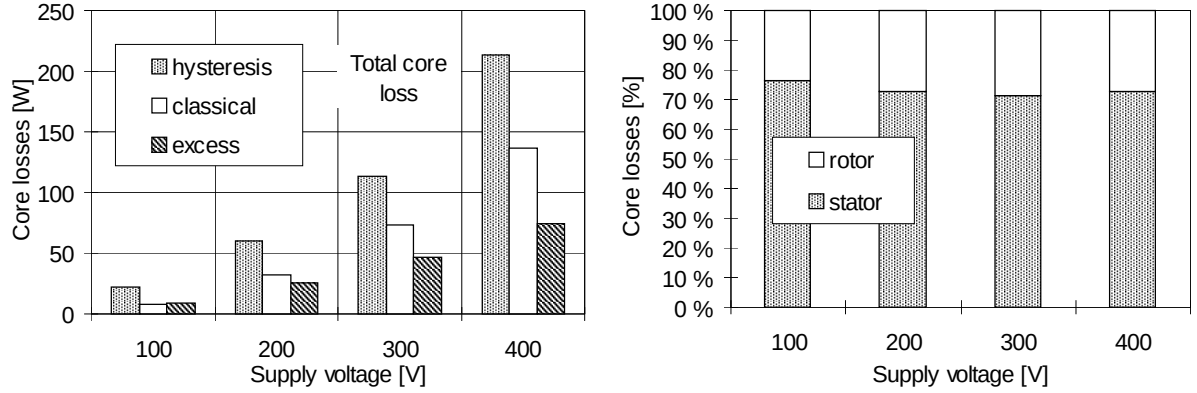

Fig. 4.19. a) The computed total core losses of the studied 37 kW induction motor separated into hysteresis, classical and excess losses as functions of the supply voltage. b) The proportion of the stator and rotor core losses as functions of the supply voltage.

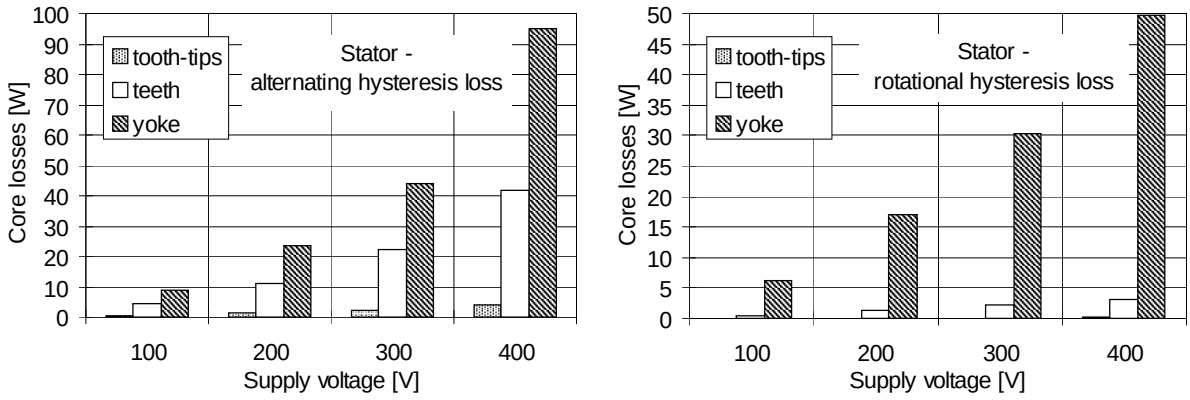

Fig. 4.20. The stator alternating (a) and rotational (b) hysteresis losses as functions of the supply voltage. The alternating and rotational hysteresis losses have been computed using Equations (2.55) and (2.57) respectively.

comparing the magnitudes of the alternating and rotational losses. It can be seen that the rotational loss is about 30% of the alternating loss. Hence, the rotational loss significantly contributes to the total hysteresis loss, and not accounting for the rotational loss when computing the losses can lead to serious errors.

Figure 4.21 examines the stator losses that are not included in the analysis of the magnetic field, namely the classical and excess losses, computed by the empirical formulae. A comparison of these losses shows, as already indicated, that these losses are of approximately the same significance, and their distribution between yoke, teeth and tooth-tips is similar.

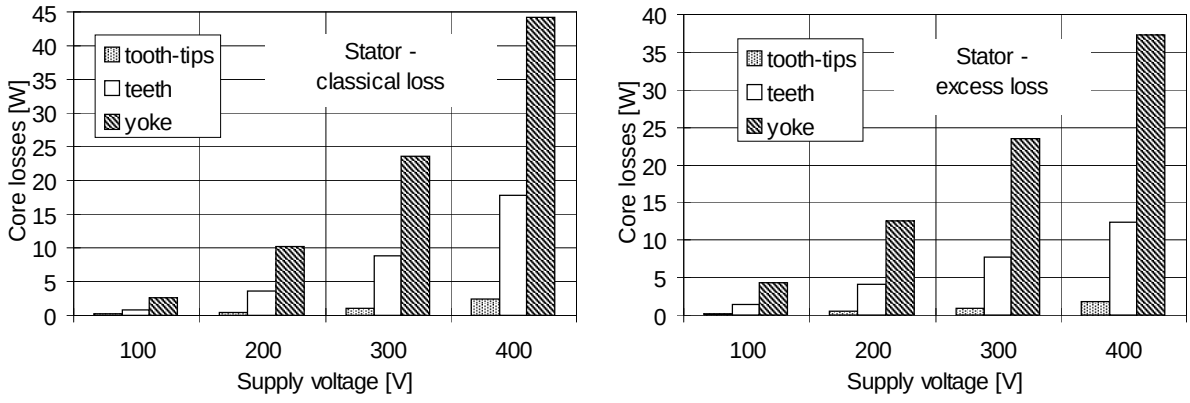

Fig. 4.21. The stator classical (a) and excess (b) losses as functions of the supply voltage. The computation of these losses has been accomplished from the computed magnetic field by employing the empirical formulae.

Figure 4.22 presents the distribution of the core losses in the rotor core. Since the field in the substantial part of the rotor (yoke, teeth) is practically constant (dc field), the core losses, unlike in the stator core, are situated primarily in the tooth-tips. The teeth contribution is insignificant and the yoke contribution is not noticeable. The dominance of the classical loss is obvious, as previously explained.

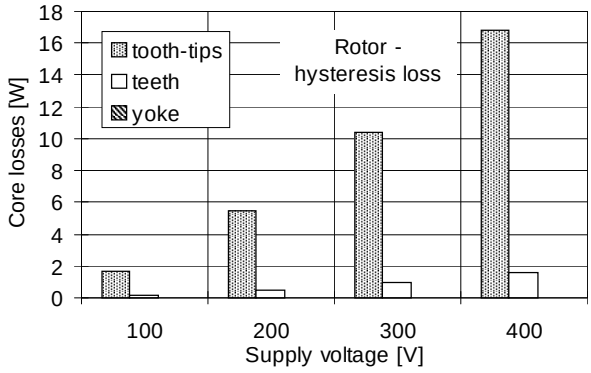

a)

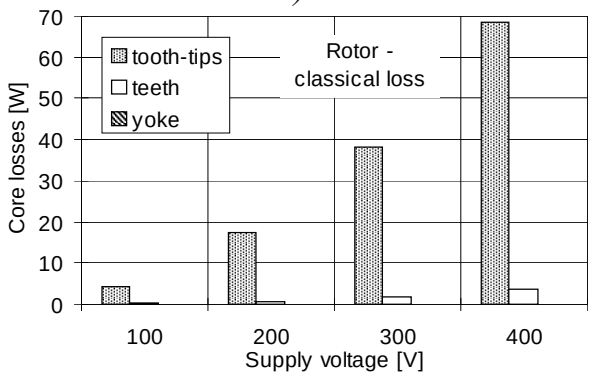

b)

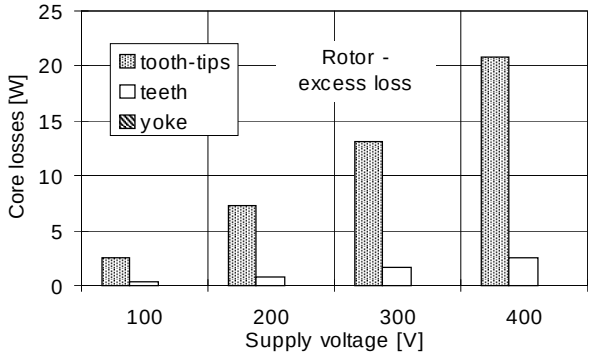

c)

Fig. 4.22. The rotor hysteresis (a), classical (b) and excess (c) losses as functions of the supply voltage. The computation of these losses has been accomplished from the computed magnetic field by employing the empirical formulae. The losses in the yoke are so small that they are not visible in the graph.

Influence of the time-step size on the power balance and core losses

The power balance of the test 37 kW motor has been evaluated from the results of the no-load operation according to the procedure outlined in Section 3.4. The calculations were performed vector models was set to 6 in all the calculations. The effect of the time-step size on the power balance for the studied motor is reported in Table 4.5. The shaft power is negative owing to higher harmonics torques associated with the losses in the rotor bars caused by higher harmonics fluxes. The reported error has been computed by subtracting all the other power components from the input power. The percentage error is computed with respect to the input power. The improvement of the computed power balance accuracy with decreasing time-step size is obvious.

TABLE 4.5. THE EFFECT OF THE TIME-STEP SIZE ON THE POWER BALANCE OF THE 37 KW MOTOR.

Time-step size [ms]:	0.2	0.1	0.05	0.025
Input power [W]	346.22	343.15	342.16	323.44
Shaft power [W]	-112.90	-115.61	-121.14	-138.88
Resistive stator losses [W]	223.83	224.69	224.76	226.89
Resistive rotor losses [W]	11.68	22.83	29.90	34.01
Hysteresis stator losses [W]	190.96	193.00	193.90	194.50
Error [W]	32.65	18.24	14.74	6.92
Error [%]	9.43	5.32	4.31	2.14

Table 4.6 presents the influence of the time-step size on the computation of the core losses (3.46). The most affected component is the classical loss, which increases almost 100% from the largest to the smallest studied time-step size. The change of the stator hysteresis loss with the time-step size is not significant.

TABLE 4.6. THE EFFECT OF THE TIME-STEP SIZE ON THE CORE LOSSES OF THE 37 KW MOTOR.

Time-step size [ms]:	0.2	0.1	0.05	0.025
Hysteresis loss (stator) [W]	190.96	193.00	193.90	194.50
Hysteresis loss (rotor) [W]	18.61	19.64	19.87	20.23
Classical loss [W]	80.59	113.67	136.52	150.1
Excess loss [W]	59.51	69.35	74.80	78.76
Total core losses [W]	349.67	395.66	425.09	443.59

Influence of the number of directions included in vector models on the power balance and core losses

The effect of the number of directions, that is, the number of scalar hysteresis models included in the vector models, on the power balance and core losses computations is presented in Table 4.7 and 4.8, respectively. These results have been computed using 400 time-steps per period.

As can be seen, the number of scalar models has only a small influence on the power balance, except for the number of directions equal to 1. This corresponds to the findings associated with the simulations of the slotless geometry in the beginning of this chapter. As can be seen from Table 4.7, although the error of the power balance does not practically change, the input power and shaft power noticeably vary with the number of directions. It is believed, however, that after 3, the number of directions does not significantly influence the shaft and input powers. Rather, the change in the powers is associated with the fact that the instantaneous no-load electromagnetic torque in the steady state oscillates very closely around zero, which affects the computation accuracy of its time average. As a matter of fact, a slight change in the time integration bounds produces a change in the computed electromagnetic torque and thus in the shaft power. This change, however, is offset by the similar behavior of the input power, which diminishes the final effect of the chosen integration bounds on the computed power balance.

TABLE 4.7. THE EFFECT OF THE NUMBER OF DIRECTIONS IN VECTOR MODELS ON THE POWER BALANCE OF THE 37 KW MOTOR.

Number of directions:	1	3	4	6	9
Input power [W]	254.14	329.09	302.58	342.16	336.93
Shaft power [W]	-82.36	-103.52	-157.77	-121.14	-125.06
Resistive stator losses [W]	173.62	213.89	221.24	224.76	225.07
Resistive rotor losses [W]	27.56	31.73	29.79	29.90	29.92
Hysteresis stator losses [W]	91.45	173.40	195.96	193.90	192.85
Error [W]	43.87	13.59	13.36	14.74	14.15
Error [%]	17.26	4.13	4.42	4.31	4.20

Regarding the core losses (Table 4.8), the stator hysteresis loss is the only component that is noticeably affected. This is because the number of directions has a direct impact on the vector models, which are included in the analysis and through which the stator hysteresis loss is eventually modeled. The dependence of the stator hysteresis loss on the number of directions confirms the results presented in Table 4.3, where the power balance in the slotless geometry simulation has been reported. The computation with more than 6 directions is clearly redundant, whereas computation with only three directions is not enough. Since the difference between 6 and 4 directions is very small, computation with 4 directions is recommended, bearing in mind that the computed total core losses are about half a per cent overestimated.

TABLE 4.8. THE EFFECT OF THE NUMBER OF DIRECTIONS IN VECTOR MODELS ON THE CORE LOSSES OF THE 37 KW MOTOR.

Number of directions:	1	3	4	6	9
Hysteresis loss (stator) [W]	91.45	173.40	195.96	193.90	192.85
Hysteresis loss (rotor) [W]	20.47	20.05	19.77	19.87	19.78
Classical loss [W]	152.69	137.43	136.83	136.52	136.54
Excess loss [W]	83.38	75.25	74.97	74.80	74.82
Total core losses [W]	347.99	406.13	427.53	425.09	423.99

4.3.4 Comparison of measured and computed core losses

This section compares the core loss computation results obtained by the proposed numerical procedure and the experimentally retrieved results. In the computations, a period of the supply voltage was discretized into 400 time-steps and 6 directions were used in the vector models included in the analysis. In addition to the results obtained by time-stepping with hysteresis, the results computed by replacing the hysteresis in the stator by a single-valued function are reported. The measurements were carried out according to the technique outlined in Section 3.5.2.

Figure 4.23 shows the comparison between the computed and measured losses for the three test motors. The computed loss represents the sum of the core loss and the resistive rotor loss so that a comparison to the measured loss is straightforward.

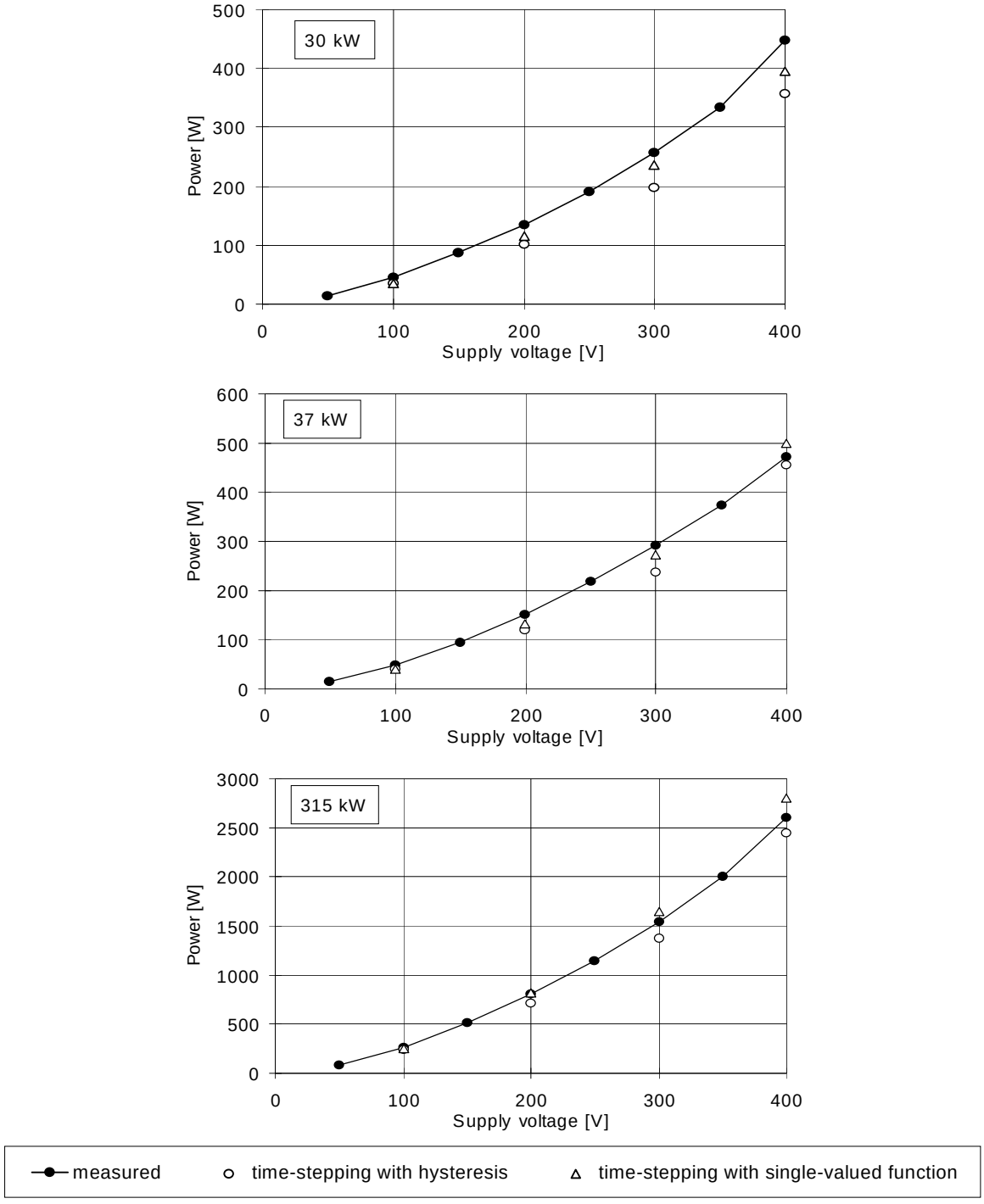

Fig. 4.23. The comparison between the measured and computed no-load losses for the three test induction motors. The computed and measured losses represent the sum of the core losses and the resistive losses of the rotor.

As can be seen from Fig. 4.23, the losses determined by time-stepping with the Preisach model are generally smaller than the losses predicted by time-stepping with a single-valued function and the empirical core loss model. This is related to the prediction of the hysteresis losses in the stator core, as indicated in Fig. 4.24, where the separation of the losses and their comparison, as predicted by the two methods for all three motors, is reported. According to the presented results, the inclusion of hysteresis in the field analysis does not influence the prediction of the losses that are not included in the field analysis.

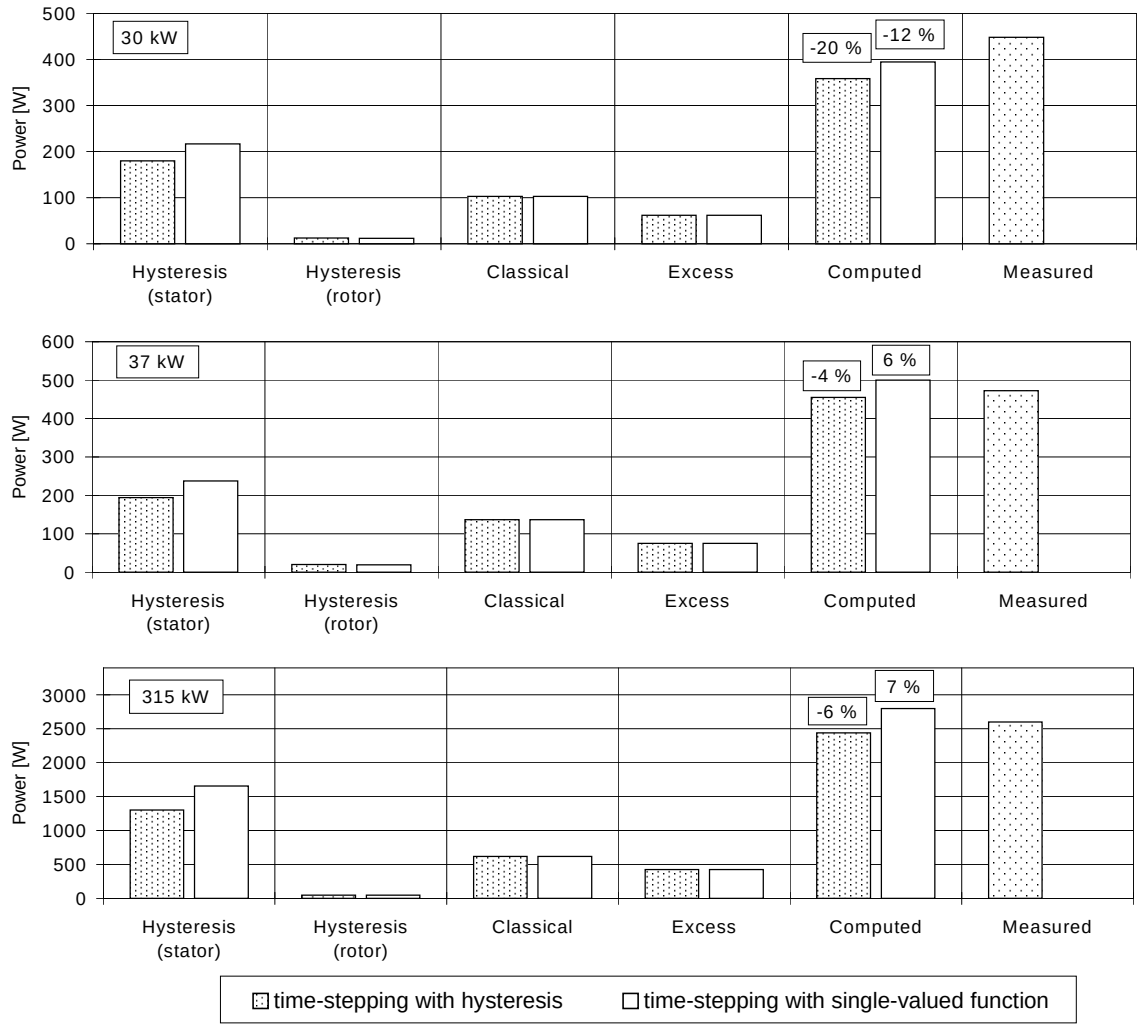

Fig. 4.24. The comparison between the no-load core loss components corresponding to rated voltage supply computed by time-stepping with hysteresis and by time-stepping with single-valued function. The percentage shown above the computed results indicates the error deviation from the measured results.

4.4 Computation times and accuracy of the results

Concerning finite element magnetic field analysis, the computation times and accuracy of the results are very important issues. Usually, they are related reciprocally and therefore a give-and-take policy has to be often applied. This was also the case in this research work, where, in order to make the analysis feasible and computation times bearable, certain simplifications had to be introduced. The issues of accuracy and computation times are discussed in the following, in which the accuracy of the measured results is also reported.

Computation times

The numerical computations were performed using computer programs developed in the MATLAB environment. MATLAB is very efficient when dealing with vectorized operations. However, certain computations (especially for-loops) do not run fast enough in MATLAB. Therefore, in order to make the computation faster, some functions, which contain unavoidable for-loops, were transformed into MEX-files. MEX-files are dynamically linked subroutines that are created from C (or FORTRAN) source code. They can be automatically loaded and executed by the MATLAB interpreter. The MEX-files were constructed using the MATLAB Compiler, which transforms ordinary MATLAB scripts (M-files) into C and creates MEX-files. MEX-files run substantially faster than M-files provided that the original code written as M-file is not vectorized too much.

The developed programs were run on a COMPAQ Alpha Server GS140 with a processor clock frequency of 525 MHz.

Typical numbers of iterations needed during one period of the field simulation of the test 37 kW motor running at synchronous speed and supplied by the rated voltage are shown in Fig. 4.25. Time-stepping with hysteresis (a), and time-stepping with single-valued function (b), are compared. The similarity in number of iterations between the two methods proves that the Fixed-Point technique works as efficiently and reliably with hysteresis as it works with single-valued functions. In other words, when using the Fixed-Point iteration, the inclusion of hysteresis in time-stepping finite element simulation does not essentially change the number of iterations needed for convergence.

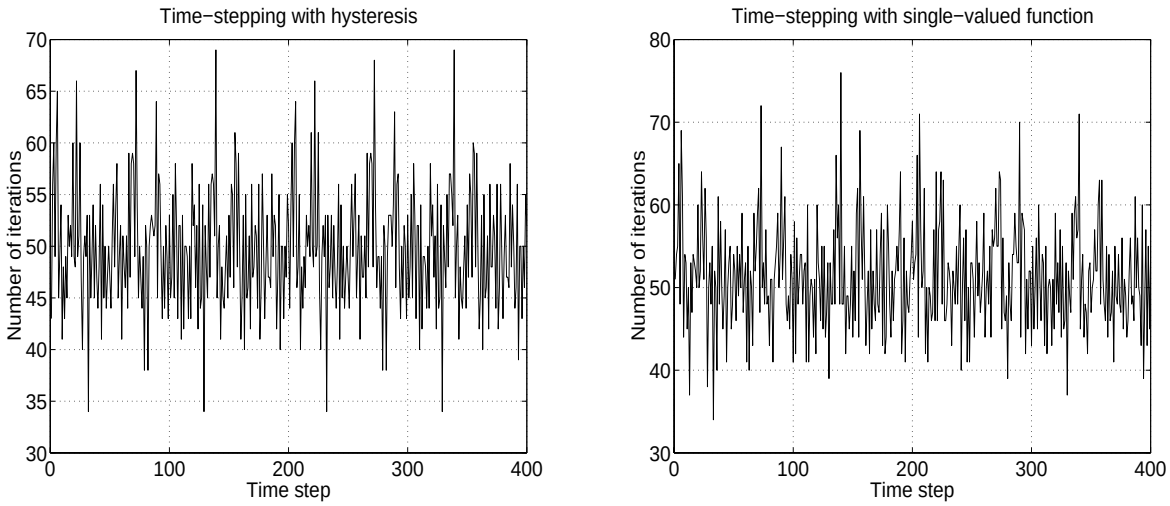

a) *b)*

Fig. 4.25. Typical numbers of iterations in each particular time-step during one period of the no-load field computation of the test 37 kW induction motor supplied by the rated voltage: a) time-stepping with hysteresis (6 directions), b) time-stepping with single-valued function. One period of the supply voltage has been discretized into 400 time-steps. The convergence criterion (page 55) stopping value was set to $5 \cdot 10^{6}$.

Table 4.9 summarizes typical values of some of the indicators related to the number of iterations and CPU times and compares time-stepping with single-valued function (SVF) and time-stepping with hysteresis, considering the different number of directions included in the vector models. The claim made in the previous paragraph is confirmed by the average number of iteration steps, which hardly changes when moving from time-stepping with single-valued

TABLE 4.9. TYPICAL CPU TIMES AND NUMBER OF ITERATIONS IN THE TIME-STEPPING NO-LOAD SIMULATION OF THE 37 KW TEST MOTOR. THE TIMES GIVEN ARE RELATED TO ONE PERIOD OF THE SUPPLY VOLTAGE DISCRETIZED INTO 400 TIME STEPS. THE ABBREVIATION SVF IN THE NUMBER OF DIRECTIONS ROW STANDS FOR THE ANALYSIS WITH THE SINGLE-VALUED FUNCTION. THE CONVERGENCE CRITERION (PAGE 55) STOPPING VALUE WAS SET TO $5 \cdot 10^{-6}$.

Number of directions:	SVF	3	4	6	9
total time (1 period – 400 time-steps) [min]	374	698	929	1218	1715
total number of iterations	20 521	20 433	20 163	19 900	19 917
average time per time-step [s]	56	105	139	183	257
average number of iterations per time-step	51	51	50	50	50
maximum number of iterations per time-step	76	70	71	69	69
average time per iteration step [s]	1.09	2.05	2.76	3.67	5.17

function to time-stepping with hysteresis and even remains essentially unchanged in the analyses with different numbers of directions. However, the most significant information that arises from Table 4.9 is the ratio between the total times, which shows how many times the incorporation of hysteresis slows down the time-stepping field simulation. For instance, the computation with 4 directions takes about 2.5 times more CPU time than the computation with a single-valued function, and the computation with 6 directions lasts about 3 times longer. When deciding about how many directions should be employed in vector models, one should keep in mind that the computation with 6 directions takes about 30% more CPU time than the computation with 4 directions.

Having discussed the CPU times and numbers of iterations, concerning time-stepping with a single-valued function, it should be noted that it is a usual practice to employ the Newton-Raphson iteration scheme and the magnetic reluctivity as a function of square flux density. However, for the sake of comparison, the Fixed-Point technique was used in all the computations presented above with a single-valued function given in the form of a *B-H* relationship.

Accuracy of the computed results

The accuracy of the hysteresis model used, the empirical formulae and the core loss computation of the test motors are now discussed.

As reported earlier, a certain discrepancy was observed when comparing the measured results and computed outputs from the scalar hysteresis model. This is most probably a result of a trade-off associated with the simplified identification procedure of the scalar model. It is believed that better accuracy would be obtained if some other more involved identification procedure were employed, for instance the identification of the scalar model by using first-order transition curves.

As far as the vector model is concerned, a direct comparison with the experiments, requiring rather complicated procedures and experimental set-ups, has not been performed. Instead, the accuracy of the vector model has been tested indirectly by comparing the computed and measured hysteresis torques. It has turned out that the predictions gave too small values of the torque for voltages smaller than 300 V. At higher voltages, the accuracy improved, not surpassing the error of 11%, which can be considered reasonable. Nevertheless,

the known deficiencies of a classical vector Preisach model, such as the fact that the model overestimates the rotational hysteresis, certainly deteriorate the accuracy of the results. A simple procedure for determining the vector distribution function probably takes its toll as well. For more precise vector modelling, the approach presented by Bottauscio et al. (1998) could be used. This approach, similarly to the method used in this work, allows the identification of the vector distribution function directly from the scalar one for isotropic materials.

One more simplification related to the hysteresis model, and one that possibly reduces the accuracy, should be addressed. The simplification involves the employment of the first-order finite element mesh for the magnetic field analysis. The accuracy is expected to be improved by employing a denser first-order finite element mesh, especially in the core region. This, however, would increase the computation time. In principle, there is no problem in using a second-order mesh with isoparametric elements. In such a case the number of integration points in one element required for sufficiently accurate numerical integration would be higher than one, as discussed in Section 3.2.3. This means that it would be necessary to keep a history track for each of these points, which would enlarge the computation time and memory size requirement several times, as far as the hysteresis model is concerned.

The computed core losses for the 30 kW motor are too small when compared to the measured values. This is especially the case when the time-stepping with hysteresis is concerned. The predicted core losses for the other two test motors are tolerable, with the relative error not exceeding 10% for the rated voltages. The error is attributed to different simplifications that have been made in order to make the analysis computationally feasible (two-dimensional field approximation, no skin effect in the conductors of the stator winding, no currents in the laminated iron core, no hysteresis in the rotor core, rotor cage completely short-circuited). Unfortunately, a fair comparison of the computed and measured results is hindered by the fact the exact core material properties of the measured test motors have not been available. In order to make more general and reliable conclusions about the accuracy of the proposed calculation method, more motors should be put under scrutiny as well. On the other hand, however, it should be remarked that real machines are not the best test rigs for verifying core loss models and calculations.

In respect of the empirical formulae, the accuracy is again limited by the determination of the coefficients only from the measurements under alternating flux. In order to improve the computation of the losses by empirical formulae, the separation of the losses under rotating flux should be performed (Bertotti et al., 1994; Zhu and Ramsden, 1998).

Accuracy of measurements

The core loss measurements on the test induction motor were performed in order to verify the proposed calculation methods. Concerning these measurements, a NORMA 6100 power analyzer was used to measure the total power taken by the motor. The induction motor running close to the synchronous speed has a small power factor. The power factor in all the measured cases was within the range 0.01 – 0.1. According to the specifications of the power analyzer, the measuring error should be smaller than 1% at these power factors. This is related to the total measured power. However, in order to get the core loss from the total measured loss, the resistive loss of the stator winding should be subtracted. It is estimated that the error of the resistive loss determination is less than 5%. This error is due to the uncertainty associated with temperature and skin effect when computing the resistance of the winding. The portion of the power associated with the core loss depends on the magnitude of the supply voltage. For 100 V about 90% of the total loss is the core loss. For the rated voltage of 400 V it is 75%, and for 500 V it is only 45%. The smaller the portion of the core loss, the larger the influence of the resistive loss error on the accuracy. Thus, it can be roughly estimated that the error in the measured core loss is less than 3% at voltages below the rated one. At the highest voltage the error is less than 8.5%.

5 Conclusions

The thorough literature review performed in the beginning of this research work and constantly updated during the course of the research supports the conclusion that the problem of field computation with hysteresis has become a major research topic. The proposed solutions to the problem are numerous, obviously indicating that the research topic is unsettled and that the ultimate solution has not yet been found.

The simple hysteresis model used in this work does not demand complex measurements and its accuracy proved to be reasonable by comparison in DC fields. However, the prediction of the hysteresis losses by the model could be a little better.

As far as the technique of identifying a vector distribution function is concerned, it can be concluded from the presented results that the method is simple, easy to use and sufficiently accurate.

The hysteresis torque computations and measurements confirm that this technique is a good tool to validate a vector hysteresis model, because it allows the model to be tested in real complicated patterns of the field behavior in rotating machines.

Numerous computations with the presented method of 2D time-stepping finite element magnetic field analysis taking the hysteresis into account by combining a Preisach model and the Fixed-Point iteration have shown that the technique is robust, reliable and always convergent. The method is general and can be applied to the 2D magnetic field finite element analysis of any electric machine. For the time being, the relatively lengthy CPU times can be regarded as a drawback of the method. However, the possibility of employing some other, more efficient iterative schemes has been investigated and shows promising results; ultimately, rapidly growing computer power will enable, in the near or not too distant future, the solution of computationally very heavy problems.

The computed results show that computation with more than 6 directions included in the vector models is merely redundant. On the other hand, simulations with less than 4 directions in the vector models are not recommended.

The comparisons between the computed and measured core losses on the test induction motors show that, in general, the results are acceptable. In any case, more motors and with different supplies (frequency converter) and with precisely known core material properties should be analyzed in order to make more general and reliable verdicts about the efficiency and accuracy of the proposed calculation methods.

References

Adly, A. A. and Mayergoyz, I. D. 1993. **A new vector Preisach-type model of hysteresis**. Journal of Applied Physics, vol. 73, no. 10, pp. 5824-5826.

Adly, A. A., Mayergoyz, I. D., Gomez, R. D. and Burke, E. R. 1993. **Computation of magnetic fields in hysteretic media**. IEEE Transactions on Magnetics, vol. 29, no. 6, pp. 2380-2382.

Akbaba, M. and Fakhro, S. Q. 1992. **Field distribution and iron loss computation in reluctance augmented shaded-pole motors using finite element method**. IEEE Transactions on Energy Conversion, vol. 7, no. 2, pp. 302-307.

Alotto, P., Girdinio, P. and Molfino, P. 1994. **A 2D finite element procedure for magnetic analysis involving non-linear and hysteretic materials**. IEEE Transactions on Magnetics, vol. 30, no. 5, pp. 3379-3382.

Amar, M. and Kaczmarek, R. 1995. **A general formula for prediction of iron losses under nonsinusoidal voltage waveform**. IEEE Transactions on Magnetics, vol. 31, no. 5, pp. 2504-2509.

Amar, M., Kaczmarek, R. and Protat, F. 1994. **Magnetic losses in PWM voltage excitation schemes**. Proceedings of ICEM'94, Paris, France, 5-8 September 1994, pp. 536-541.

Amin, B. 1995. **Contribution to iron-loss evaluation in electrical machines**. European Transaction on Electrical Power Engineering, vol. 5, no. 5, pp. 325-332.

Amor, Y. O., Féliachi, M. and Mohellebi, H. 2000. **A new convergence procedure for the finite element computing associated to Preisach hysteresis model**. IEEE Transactions on Magnetics, vol. 36, no. 4, pp. 1242-1245.

Appino, C., Bertotti, G., Bottauscio, O., Fiorillo, F., Tiberto, P., Binesti, D., Ducreux, J. P., Chiampi, M. and Repetto, M. 1996. **Power losses in thick steel laminations with hysteresis**. Journal of Applied Physics, vol. 79, no. 8, pp. 4575-4577.

Arkkio, A. 1987. **Analysis of induction motors based on the numerical solution of the magnetic field and circuit equations**. Helsinki, Acta Polytechnica Scandinavica, Electrical Engineering Series No. 59, 97 p.

Arkkio, A. and Niemenmaa, A. 1992. **Estimation of losses in cage induction motors using finite element techniques**. Proceedings of ICEM'92, Manchester, UK, 15-17 September 1992, pp. 317-321.

Arkkio, A., Niemenmaa, A. and Saitz, J. 1998. **Hysteresis torque in a cage induction motor**. Proceedings of the International Conference on Electrical Machines, Istanbul, Turkey, 2-4 September 1998, pp. 1494-1499.

Atallah, K. and Howe, D. 1993. **Calculation of the rotational power loss in electrical steel laminations from measured H and B**. IEEE Transactions on Magnetics, vol. 29, no. 6, pp. 3547-3549.

Atallah, K., Zhu, Z. Q. and Howe, D. 1992. **An improved method for predicting iron losses in brushless permanent magnet DC drives**. IEEE Transactions on Magnetics, vol. 28, no. 5, pp. 2997-2999.

Bergqvist, A., Tiberg, H. and Engdahl, G. 1993. **Application of a vector Preisach model in a magnetic circuit**. Journal of Applied Physics, vol. 73, no. 10, pp. 5839-5841.

Bergqvist, A. 1994. **On magnetic hysteresis modeling.** Doctoral thesis, Stockholm, Royal Institute of Technology, Electric Power Engineering, 209 p.

Bertotti, G. 1988. **General properties of power losses in soft ferromagnetic materials**. IEEE Transactions on Magnetics, vol. 24, no. 1, pp. 621-630.

Bertotti, G. 1992. **Dynamic generalization of the scalar Preisach model of hysteresis**. IEEE Transactions on Magnetics, vol. 28, no. 5, pp. 2599-2601.

Bertotti, G., Boglietti, A., Chiampi, M., Chiarabaglio, D., Fiorillo, F. and Lazzari, M. 1991. **An improved estimation of iron losses in rotating electrical machines**. IEEE Transactions on Magnetics, vol. 27, no. 6, pp. 5007-5009.

Bertotti, G., Canova, A., Chiampi, M., Chiarabaglio, D., Fiorillo, F. and Rietto, A. M. 1994. **Core loss prediction combining physical models with numerical field analysis**. Journal of Magnetism and Magnetic Materials, vol. 133, pp. 647-650.

Biorci, G. and Pescetti, D. 1958. **Analytical theory of the behaviour of ferromagnetic materials**. Il Nuovo Cimento, vol. 7, no. 6, pp. 829-842.

Boglietti, A., Bottauscio, O., Chiampi, M., Pastorelli, M. and Repetto, M. 1996. **Computation and measurement of iron losses under PWM supply conditions**. IEEE Transactions on Magnetics, vol. 32, no. 5, pp. 4302-4304.

Boglietti, A., Chiampi, M., Repetto, M., Bottauscio, O. and Chiarabaglio, D. 1998. **Loss separation analysis in ferromagnetic sheets under PWM inverter supply**. IEEE Transactions on Magnetics, vol. 34, no. 4, pp. 1240-1242.

Bottauscio, O., Chiarabaglio, D., Chiampi, M. and Repetto, M. 1995. **A hysteretic periodic magnetic field solution using Preisach model and fixed-point technique**. IEEE Transactions on Magnetics, vol. 31, no. 6, pp. 3548-3550.

Bottauscio, O., Chiampi, M. and Repetto, M. 1996. **Finite element analysis of iron loss behaviour: effect of frequency and lamination thickness**. Proceedings of the 3rd International Workshop on Electric and Magnetic Fields, Liege, Belgium, 6-9 May 1996, pp. 417-422.

Bottauscio, O., Chiarabaglio, D., Ragusa, C., Chiampi, M. and Repetto, M. 1998. **Analysis of isotropic materials with vector hysteresis**. IEEE Transactions on Magnetics, vol. 34, no. 4, pp. 1258-1260.

Bottauscio, O., Chiampi, M., Chiarabaglio, D., Ragusa, C. and Repetto, M. 1999. **Ferromagnetic hysteresis and magnetic field analysis**. ICS Newsletter, vol. 6, no. 1, pp. 3-7.

Bottauscio, O., Chiampi, M. and Chiarabaglio, D. 2000a. **Advanced model of laminated magnetic cores for two-dimensional field analysis**. IEEE Transactions on Magnetics, vol. 36, no. 3, pp. 561-573.

Bottauscio, O., Chiampi, M., Fiorillo F. and Repetto, M. 2000b. **Dynamic hysteresis and voltage driven solution of a ferromagnetic laminated core**. IEEE Transactions on Magnetics, vol. 36, no. 4, pp. 1238-1241.

Boucetta, A., Jammal, A. and Grellet, G. 1994. **Computing ferrite core losses at high frequency by finite elements method including temperature influence**. IEEE Transactions on Magnetics, vol. 30, no. 5, pp. 3733-3736.

Cecchetti, A., Ferrari, G., Masoli, F. and Soardo, G. P. 1978. **Rotational power losses in 3 % SiFe as a function of frequency**. IEEE Transactions on Magnetics, vol. 14, no. 5, pp. 356-358.

Chiampi, M., Negro, A and Tartaglia, M. 1980. **A finite element method to compute three-dimensional magnetic field distribution in transformer cores**. IEEE Transactions on Magnetics, vol. 16, pp. 1413-1419.

Chiampi, M., Chiarabaglio, D. and Repetto, M. 1994a. **An accurate investigation on numerical methods for nonlinear magnetic field problems**. Journal of Magnetism and Magnetic Materials, vol. 133, pp. 591-595.

Chiampi, M., Repetto, M and Chiarabaglio, D. 1994b. **An improved technique for nonlinear magnetic problems**. IEEE Transactions on Magnetics, vol. 30, no. 6, pp. 4332-4334.

Chiampi, M., Chiarabaglio, D. and Repetto, M. 1995. **A Jiles-Atherton and fixed-point combined technique for time periodic magnetic field problems with hysteresis**. IEEE Transactions on Magnetics, vol. 31, no. 6, pp. 4306-4311.

Deblecker, O., Lobry, J. and Broche, C. 1998. **New solution method for magnetodynamic problems in hysteretic media using transmission-line modelling (TLM) and Preisach theory**. Proceedings of the 4th International Workshop on Electric and Magnetic Fields, Marseille, France, 12-15 May 1998, pp. 201-206.

Delincé, F., Nicolet, A., Henrotte, F., Genon, A. and Legros, W. 1994. **Influence of hysteresis on the behaviour of coupled finite element - electric circuit models**. IEEE Transactions on Magnetics, vol. 30, no. 5, pp. 3383-3386.

Del Vecchio, R. M. 1980. **An efficient procedure for modeling complex hysteresis processes in ferromagnetic materials.** IEEE Transactions on Magnetics, vol. 16, no. 5, pp. 809-811.

Del Vecchio, R. M. 1982. **The inclusion of hysteresis processes in a special class of electromagnetic finite element calculations.** IEEE Transactions on Magnetics, vol. 18, no. 1, pp. 275-284.

Dular, P., Gyselinck, J., Henrotte, F., Legros, W. and Melkebeek, J. 1998. **Modeling of eddy currents in steel laminations using complementary** 3**D finite element formulations with enforced magnetic fluxes**. Proceedings of the 4th International Workshop on Electric and Magnetic Fields, Marseille, France, 12-15 May 1998, pp. 177-182.

Dupré, L. R., Van Keer, R. and Melkebeek, J. A. A. 1997a. **An iron loss model for electrical machines using the Preisach theory**. IEEE Transactions on Magnetics, vol. 33, no. 5, pp. 4158-4160.

Dupré, L. R., Van Keer, R. and Melkebeek, J. A. A. 1997b. **Modelling and identification of iron losses in nonoriented steel laminations using Preisach theory**. IEE Proceedings - Electr. Power Appl., vol. 144, no. 4, pp. 227-234.

Dupré, L. R., Bottauscio, O., Chiampi, M., Repetto, M. and Melkebeek, J. A. A. 1999. **Modeling of electromagnetic phenomena in soft magnetic materials under unidirectional time periodic flux excitations**. IEEE Transactions on Magnetics, vol. 35, no. 5, pp. 4171-4184.

Dupré, L., Gyselinck, J. and Melkebeek, J. 1998a. **Complementary finite element methods in 2D magnetics taking into account a vector Preisach model**. IEEE Transactions on Magnetics, vol. 34, no. 5, pp. 3048-3051.

Dupré, L. R., Van Keer, R. and Melkebeek, J. A. A. 1998b. **A study of the influence of laser cutting and punching on the electromagnetic behaviour of electrical steel sheets using a combined finite element-dynamic Preisach model**. Proceedings of the 4th International Workshop on Electric and Magnetic Fields, Marseille, France, 12-15 May 1998, pp. 195-200.

Dupré, L. R., Bottauscio, O., Chiampi, M., Fiorillo, F., Lo Bue, M., Melkebeek, J., Repetto, M. and Von Rauch, M. 1998c. **Dynamic Preisach modelling of ferromagnetic laminations under distorted flux excitations**. IEEE Transactions on Magnetics, vol. 34, no. 4, pp. 1231-1233.

Dupré, L. R., Bertotti, G. and Melkebeek, J. A. A. 1998d. **Dynamic Preisach model and energy dissipation in soft magnetic materials**. IEEE Transactions on Magnetics, vol. 34, no. 4, pp. 1168-1170.

Féliachi, M. and Meunier, G. 1985. **Two dimensional hysteresis model using finite element method.** IEEE Transactions on Magnetics, vol. 21, no. 6, pp. 2362-2365.

Findlay, R. D., Stranges, N. and MacKay, D. K. 1994. **Losses due to rotational flux in three phase induction motors**. IEEE Transactions on Energy Conversion, vol. 9, no. 3, pp. 543-549.

Fiorillo, F. and Novikov, A. 1990a. **An improved approach to power losses in magnetic laminations under nonsinusoidal induction waveform**. IEEE Transactions on Magnetics, vol. 26, no. 5, pp. 2904-2910.

Fiorillo, F. and Novikov, A. 1990b. **Power losses under sinusoidal, trapezoidal and distorted induction waveform**. IEEE Transactions on Magnetics, vol. 26, no. 5, pp. 2559-2561.

Fiorillo, F. and Rietto, A. M. 1990. **Rotating and alternating energy loss vs. magnetizing frequency in SiFe laminations**. Journal of Magnetism and Magnetic Materials, vol. 83, pp. 402-404.

Flack, T. J. and Williamson, S. 1996. **On the possible use of magnetic slot wedges to reduce iron losses in cage motors**. Proceedings of ICEM'96, Vigo, Spain, 10-12 September 1996, pp. 417-422.

Ferreira da Luz, M. V., Bastitela N. J., Sadowski, N., Carlson R. and Bastos, J. P. A. 2000. **Calculation of iron losses in induction motors using the finite element method**. Proceedings of ICEM'2000, Espoo, Finland, 28-30 August 2000, pp. 1512-1515.

Fetzer, J., Kurz, S., Lehner, G. and Rucker W. M. 2000. **Application of BEM-FEM coupling and the vector Preisach model for the calculation of** 3**D magnetic fields in media with hysteresis**. IEEE Transactions on Magnetics, vol. 36, no. 4, pp. 1258-1261.

Friedman, G. and Mayergoyz, I. D. 1989. **Computation of magnetic field in media with hysteresis**. IEEE Transactions on Magnetics, vol. 25, no. 5, pp. 3934-3936.

Gourdin, C., Ossart, F., Hirsinger, L. and Billardon, R. 1998. **Finite element implementation of an internal variable hysteresis model including stress dependence**. Proceedings of the 4th International Workshop on Electric and Magnetic Fields, Marseille, France, 12-15 May 1998, pp. 189-194.

Gyimóthy, Sz. and Iványi, A. 1994. **Implementation and application of the 2D vectorial Preisach model for field calculation with finite element method**. Proceedings of the 6th Int. IGTE Symposium on Numerical Field Calculation in Electrical Engineering, 26-28 Sept. 1994, Graz, Austria, pp. 89-94.

Gyselinck, J., Dupré, L., Vandevelde, L. and Melkebeek, J. 1996. **Calculation of iron losses in electrical machines using the Preisach model**. Proceedings of the 3rd International Workshop on Electric and Magnetic Fields, Liege, Belgium, 6-9 May 1996, pp. 423-428.

Gyselinck, J., Dupré, L., Vandevelde, L. and Melkebeek, J. 1998. **Calculation of no-load induction motor core losses using the rate-dependent Preisach model**. IEEE Transactions on Magnetics, vol. 34, no. 6, pp. 3876-3881.

Gyselinck, J., De Wulf, M., Vandevelde, L. and Melkebeek, J. 1999a. **Incorporation of vector hysteresis end eddy current losses in 2D FE magnetodynamics**. Proceedings of Electrimacs'99, 14-16 September 1999, Lisbon, Portugal, vol. 3, pp. 37-44.

Gyselinck, J., Vandevelde, L., Melkebeek, J., Dular, P., Henrotte, F. and Legros, W. 1999b. **Calculation of eddy currents and associated losses in electrical steel laminations**. IEEE Transactions on Magnetics, vol. 35, no. 3, pp. 1191-1194.

Gyselinck, J., Vandevelde, L., Makaveev D. and Melkebeek, J. 2000. **Calculation of no load losses in an induction motor using an inverse vector Preisach model and an eddy current loss model**. IEEE Transactions on Magnetics, vol. 36, no. 4, pp. 856-860.

Hantila, F. I. 1974. **Mathematical models of the relation between B and H for non-linear media**. Revue Roumaine des Sciences Techniques - Électrotechnique et Énergétique, vol. 19, no. 3, pp. 429-448.

Hantila, F. I. 1975. **A method of solving stationary magnetic field in non-linear media**. Revue Roumaine des Sciences Techniques - Électrotechnique et Énergétique, vol. 20, no. 3, pp. 397-407.

Hayashi, Y. and Miller, T. J. E. 1995. **A new approach to calculating core losses in the SRM**. IEEE Transactions on Magnetics, vol. 31, no. 5, pp. 1039-1046.

Henrotte, F., Nicolet, A., Delincé, F., Genon, A. and Legros, W. 1992. **Modeling of ferromagnetic materials in 2D finite element problems using Preisach's model**. IEEE Transactions on Magnetics, vol. 28, no. 5, pp. 2614-2616.

Hong, S., Kim, D., Jung, H. and Won, J. 1994. **Vector hysteresis model for unoriented magnetic materials**. IEEE Transactions on Magnetics, vol. 30, no. 5, pp. 3371-3374.

Hong, S., Lee, S. and Won, J. 1995. **Properties of the vector hysteresis model for unoriented magnetic materials**. IEEE Transactions on Magnetics, vol. 31, no. 3, pp. 1833-1836.

Ionita, V. 1991a. **An iterative method for the quasistationary magnetic field calculation of nonlinear magnetic materials with hysteresis**. Revue Roumaine des Sciences Techniques - Électrotechnique et Énergétique, vol. 36, no. 3, pp. 291-298.

Ionita, V. 1991b. **A study on the magnetization of magnetic materials with hysteresis**. Revue Roumaine des Sciences Techniques - Électrotechnique et Énergétique, vol. 36, no. 4, pp. 399-408.

Ionita, V., Cranganu-Cretu, B. and Ioan, D. 1996. **Quasi-stationary magnetic field computation in hysteretic media**. IEEE Transactions on Magnetics, vol. 32, no. 3, pp. 1128-1131.

Iványi, A. 1997. **Hysteresis models in electromagnetic computation**. Budapest, Akadémiai Kiadó, 229 p.

Jamil, M. K. and Demerdash, N. A. 1990. **Harmonics and core losses of permanent magnet DC motors controlled by chopper circuits**. IEEE Transactions on Energy conversion, vol. 5, no. 2, pp. 408-413.

Jamil, M. K., Baldassari, P. and Demerdash, N. A. 1992. **No-load induction motor core losses using a combined finite element state space model**. IEEE Transactions on Magnetics, vol. 28, no. 5, pp. 2820-2822.

Jayaraman, S. and Strangas, E. G. 1994. **Iron losses from time dependent finite element solutions**. Proceeding of ICEM'94, Paris, France, 5-8 September 1994, pp. 683-686.

Jiles, D. C. and Atherton, D. L. 1984. **Theory of ferromagnetic hysteresis**. Journal of Applied Physics, vol. 55, pp. 2115-2120.

Jiles, D. C. 1994. **Modelling of effects of eddy current losses on frequency dependent hysteresis in electrically conducting media**. IEEE Transactions on Magnetics, vol. 30, no. 6, pp. 4326-4328.

Kaczmarek, R., Amar, M. and Protat, F. 1996. **Iron loss under PWM voltage supply on Epstein frame and in induction motor core** IEEE Transactions on Magnetics, vol. 32, no. 1, pp. 189-194.

Kim, H., Jung, H. and Hong, S. 1998a. **Finite element analysis of hysteresis motor using the vector magnetization-dependent model**. IEEE Transactions on Magnetics, vol. 34, no. 5, pp. 3495-3498.

Kim, J. Ch., Lee, J. H., Jung, I. S. and Hyun, D. S. 1998b. **Vector control scheme of synchronous reluctance motor considering iron core loss**. IEEE Transactions on Magnetics, vol. 34, no. 5, pp. 3522-3527.

Klug, L. and Ibrahim, S. A. 1987. **Computation of the power and efficiency of induction motors at frequency speed control**. Modelling, Simulation and Control, A, AMSE Press, vol. 13, no. 1, pp. 1-8.

Köfler, H. 1990. **Losses in electrical machines**. Espoo, Helsinki University of Technology, Laboratory of Electromechanics, Report series 26, 111 p.

Kurz, S., Fetzer, J. and Lehner, G. 1993**. Application of the finite element method and the vector-Preisach-model for the calculation of** 2**-dimensional magnetostatic fields in media with hysteresis.** Archiv für Elektrotechnik 76, pp. 405-415. (In German).

Leonard, P. J., Rodger, D., Karagular, T. and Coles, P. C. 1995. **Finite element modelling of magnetic hysteresis**. IEEE Transactions on Magnetics, vol. 31, no. 3, pp. 1801-1804.

Lee, J. H., Kim, J. Ch. and Hyun, D. S. 1998. **Dynamic characteristics analysis of synchronous reluctance motor considering saturation and iron loss by FEM**. IEEE Transactions on Magnetics, vol. 34, no. 5, pp. 2629-2632.

Lee, J. H. and Hyun, D. S. 1999. **Hysteresis analysis for the permanent magnet assisted synchronous reluctance motor by coupled FEM & Preisach modelling**. IEEE Transactions on Magnetics, vol. 35, no. 3, pp. 1203-1206.

Lee, J. H. and Hyun, D. S. 2000. **Hysteresis characteristics computation on PWM fed synchronous reluctance motor using coupled FEM and Preisach modeling**. IEEE Transactions on Magnetics, vol. 36, no. 4, pp. 1209-1213.

Luomi, J., Niemenmaa, A. and Arkkio A. 1986. **On the use of effective reluctivities in magnetic field analysis of induction motors fed from a sinusoidal voltage source**. Proceedings of the International Conference on Electrical Machines, München, Germany, 8-10 September 1986, vol. 2, pp. 706-709.

Macfadyen, W. K., Simpson, R. R. S., Slater, R. D., Wood, W. S. 1973. **Representation of magnetisation curves by exponential series.** Proceedings IEE, vol. 120, no. 8, pp. 902-904.

Machado, V. M. and Ribeiro, A. L. 1998. **Eddy current and hysteresis losses in ferromagnetic media**. IEEE Transactions on Magnetics, vol. 34, no. 4, pp. 1267-1269.

Mayergoyz, I. D. 1982. **Iteration methods for the calculation of steady magnetic fields in nonlinear ferromagnetic media.** COMPEL, vol. 1, no. 2, pp. 89-110.

Mayergoyz, I. D. 1991. **Mathematical models of hysteresis.** New York, Springer-Verlag, 207 p.

McClay, C. I., Williamson, S. and Mueller, M. A. 1996. **Calculation of high-frequency losses in closed-slot induction motor rotors**. Proceedings of the International Conference on Electrical Machines, Vigo, Spain, 10-12 September 1996, pp. 411-416.

Moses, A. J. 1990. **Electrical steels: past, present and future developments**. IEE Proceedings-A, vol. 137, no. 5, pp. 233-245.

Miano, G., Serpico, C., Verolino, L. and Visone, C. 1995. **Comparison of different hysteresis models in FE analysis of magnetic field diffusion**. IEEE Transactions on Magnetics, vol. 31, no. 3, pp. 1789-1792.

Naidu, S. R. 1990. **Simulation of the hysteresis phenomenon using Preisach's theory**. IEE Proceedings-A, vol. 137, no. 2, pp. 73-79.

Naidu, S. R. 1991. **Time domain model for the ferromagnetic core, including the effects of hysteresis and eddy currents**. IEE Proceedings-A, vol. 138, no. 1, pp. 44-50.

Nakata, T. 1998. **Present situation, trends and what is needed for the future in the FEM analysis of electrical machines**. Proceedings of the International Conference on Electrical Machines, Istanbul, Turkey, 2-4 September 1998, pp. 685-691.

Nee, H-P. and Nipp, E. 1994. **A contribution to the calculation of harmonic iron losses of inverter-fed induction motors**. Proceeding of the International Conference on Electrical Machines, Paris, France, 5-8 September 1994, pp. 698-703.

Ninet, O., Peccolo, M. A., Fraisse, H. and Masson, J. P. 1996. **Experimental validation of a 2-D magnetostatic field calculation including hysteresis**. Proceedings of the 3rd International Workshop on Electric and Magnetic Fields, Liege, Belgium, 6-9 May 1996, pp. 435-440.

Ninet, O., Raulet, M. A. and Masson, J. P. 1998. **Hysteresis influence study in surface field calculation**. Proceedings of the 4th International Workshop on Electric and Magnetic Fields, Marseille, France, 12-15 May 1998, pp. 207-212.

Ossart, F. and Meunier, G. 1991. **Results on modeling magnetic hysteresis using the finite-element method**. Journal of Applied Physics, vol. 69, no. 8, pp. 4835-4837.

Pahner, U., Belmans, R. and Hameyer, K. 1998. **Optimizing ferromagnetic characteristic to reduce Newton iterations**. Proceedings of the XV Symposium on Electromagnetic Phenomena in Nonlinear Circuits, Liége, Belgium, 22-24 September 1998, pp. 7-10.

Philips, D. A. and Delincé, F. 1993. **Practical use of the Preisach model from measurements to finite elements**. IEEE Transactions on Magnetics, vol. 29, no. 6, pp. 2383-2385.

Philips, D., Dupré, L., Cnops, J. and Melkebeek, J. 1994a. **The application of the Preisach model in magnetodynamics: theoretical and practical aspects**. Journal of Magnetism and Magnetic Materials, vol. 133, pp. 540-543.

Philips, D. A., Dupré, L. R. and Melkebeek, J. A. 1994b. **Magneto-dynamic field computation using a rate-dependent Preisach model**. IEEE Transactions on Magnetics, vol. 30, no. 6, pp. 4377-4379.

Philips, D. A., Dupré, L. R. and Melkebeek, J. A. 1995. **Comparison of Jiles and Preisach hysteresis models in magnetodynamics**. IEEE Transactions on Magnetics, vol. 31, no. 6, pp. 3551-3553.

Raulet, M. A. and Masson, J. P. 1998. **Implementation of a dynamic hysteresis generator in the magnetic field diffusion equation**. Proceedings of the 4th International Workshop on Electric and Magnetic Fields, Marseille, France, 12-15 May 1998, pp. 445-450.

Robertson, D. 1911. **Rotor hysteresis in polyphase induction motors**. The Electrician, October 13, pp. 12-14.

Rouve, L-L., Ossart, F., Waeckerlé, T. and Kedous-Lebouc, A. 1996. **Magnetic flux and losses computation in electrical laminations**. IEEE Transactions on Magnetics, vol. 32, no. 5, pp. 4219-4221.

Saari, J. and Arkkio, A. 1994. **Losses in high-speed asynchronous motors**. Proceeding of the International Conference on Electrical Machines, Paris, France, 5-8 September 1994, pp. 704-708.

Saitz, J. 1999a. **Ferromagnetic hysteresis in finite element computation of magnetic fields**. Espoo, Acta Polytechnica Scandinavica, Electrical Engineering Series No. 96, 76 p.

Saitz, J. 1999b. **Newton-Raphson method and fixed-point technique in finite element computation of magnetic field problems in media with hysteresis**. IEEE Transactions on Magnetics, vol. 35, no. 3, pp. 1398-1401.

Saitz, J. and Arkkio, A. 1999. **Core loss estimation of a cage induction motor using the vector Preisach hysteresis model incorporated in finite element analysis**. Proceedings of the EDPE conference, Stará Lesná, the High Tatras, Slovakia, 5-7 October 1999, pp. 473-478.

Saitz, J. 2000. **Computation of the core loss in an induction motor using the vector Preisach hysteresis model incorporated in finite element analysis**. IEEE Transactions on Magnetics, vol. 36, no. 4, pp. 769-773.

Saitz, J., Arkkio, A. and Negrea, M. 2000. **Finite element modeling of the magnetic field in asynchronous motors taking ferromagnetic hysteresis into account**. Proceedings of the 9th International Conference and Exhibition on Power Electronics and Motion Control (EPE-PEMC 2000), September 5-7, 2000, Kosice, Slovakia, pp. 5-86 - 5-92.

Saitz, J. 2001. **Magnetic field analysis of induction motors combining Preisach hysteresis modeling and finite element techniques**. IEEE Transactions on Magnetics, accepted for publication (September 2001).

Slemon, G. R. and Liu, X. 1990. **Core losses in permanent magnet motors**. IEEE Transactions on Magnetics, vol. 26, no. 5, pp. 1653-1655.

Silvester, P. P. and Ferrari, R. L. 1991. **Finite elements for electrical engineers**. Cambridge, Cambridge University Press, 344 p.

Smith, A. C. and Phipson, G. 1991. **Iron losses in cage induction motors**. Proceedings of the 5th International Conference on Electrical Machines and Drives, London, UK, 11-13 September 1991, pp. 255-259.

Smith, A. C., White, I., Le Flem, G. and Glew, C. N. 1996. **Frame losses in large cage induction motors**. Proceedings of ICEM'96, Vigo, Spain, 10-12 September 1996, pp. 405-410.

Szücs, A. and Arkkio, A. 1999. **Consideration of eddy currents in multi-conductor windings using the finite element and the elimination of inner nodes**. IEEE Transactions on Magnetics, vol. 35, no. 3, pp. 1147-1150.

Szücs, A. 2000. **Macro elements in the finite element analysis of multi-conductor eddy-current problems**. IEEE Transactions on Magnetics, vol. 36, no. 4, pp. 813-817.

Štumberger, B, Hribernik, B. and Hamler, A. 2000. **Core loss calculation in electrical machines**. Proceedings of ICEM'2000, Espoo, Finland, 28-30 August 2000, pp. 1516-1520.

Takahashi, N., Miyabara, S. and Fujiwara, K. 1998. **Investigation on finite element analysis using Preisach hysteresis model**. Proceedings of the 4th International Workshop on Electric and Magnetic Fields, Marseille, France, 12-15 May 1998, pp. 183-188.

Tellinen, J. 1998. **A simple scalar model for magnetic hysteresis**. IEEE Transactions on Magnetics, vol. 34, no. 4, pp. 2200-2206.

Toms, H. L., Colclaser, R. G. Jr. and Krefta, M. P. 2001. **Two-dimensional finite element magnetic modeling for scalar hysteresis effects**. IEEE Transactions on Magnetics, vol. 37, no. 2, pp. 982-988.

Wieser, R. and Lechner, A. 1996. **The influence of rotor hysteresis effects on space phasor models of induction machines**. Proceedings of ICEM'96, Vigo, Spain, pp. 119-124.

Zhu, J. G., Ramsden, V. S. and Watterson, P. A. 1992. **Finite element calculation of core losses in motors with non-sinusoidal fields**. Proceedings of ICEM'92, Manchester, UK, 15-17 September 1992, pp. 1182-1186.

Zhu, J. G. and Ramsden, V. S. 1993a. **Core loss modelling in rotational electrical machines**. Proceedings of The International Conference on Electrical Machines in Australia, Adelaide, Australia, 14-16 September 1993, vol. 1, pp. 52-57.

Zhu, J. G. and Ramsden, V. S. 1993b. **Two-dimensional measurement of magnetic field and core loss using a square specimen tester**. IEEE Transactions on Magnetics, vol. 29, no. 6, pp. 2995-2997.

Zhu, J. G., Ramsden, V. S. and Sievert, J. D. 1994. **Prediction of core loss with elliptical flux from measurements with alternating and circular fluxes in electrical steel sheets**. Proceedings of the International Symposium on Non-Linear Electromagnetic Systems ISEM'94, Seoul, Korea, 1994.

Zhu, J. G. and Ramsden, V. S. 1995. **A novel calculation of core losses in rotating electrical machines**. Proceedings of the 2nd Chinese International Conference on Electrical Machines CICEM'95, Hangzhou, China, 31 August-2 September 1995, pp. 631-636.

Zhu, J. G., Ramsden, V. S. and Sievert, J. D. 1995. **Modelling of rotational hysteresis loss in electrical sheet steels**. Proceedings of the International Symposium on Non-Linear Electromagnetic Systems ISEM'95, Cardiff, Wales, UK, 17-20 September 1995.

Zhu, J. G. and Ramsden, V. S. 1998. **Improved formulations for rotational core losses in rotating electrical machines**. IEEE Transactions on Magnetics, vol. 34, no. 4, pp. 2234-2242.

Appendix A. Parameters of the measured ferromagnetic wound-ring

The test sample used for the DC-field measurements and core loss separation measurements was prepared from ferromagnetic laminations obtained from a manufacturer of electric machines as typical laminations used in electric machines. There was no heat treatment of the laminations after punching. The burrs caused by punching were leveled off with a file. The parameters of the ferromagnetic wound-ring sample are given in Table A1.

TABLE A1. PARAMETERS OF THE MEASURED FERROMAGNETIC WOUND-RING.

Parameter:	
Mass [kg]	0.1083
Number of laminations	20
Lamination thickness [mm]	0.5
Outer diameter [mm]	95
Inner diameter[mm]	85
Mass density [kg/m^3]	7690
Lamination conductivity [S/m]	24.2×10^5
Number of turns of the magnetizing winding	711
Diameter of the magnetizing-winding wire [mm]	1.18
Number of turns of the measuring winding	780
Diameter of the measuring-winding wire[mm]	0.315

Appendix B. DC-field measurement on a wound-ring sample

The upper branch of the limiting hysteresis loop as well as other symmetric and unsymmetric quasi-static hysteresis loops of a ferromagnetic material were experimentally determined using the measuring set-up shown in Fig. B1. The parameters of the wound-ring sample are summarized in Appendix A. The ring was wound with magnetizing and measuring windings. The whole measurement is controlled by a PC, which instructs an Arbitrary Waveform Generator about the required sequence of input dc voltages. The signal is amplified in a Power Amplifier and fed into the magnetizing winding of the test ring. The measuring winding is connected to an Integrating Fluxmeter in order to get the flux and thus the flux density from the induced voltage. The primary current is used to compute the magnetic field intensity. The data are transferred to the PC and collected into files.

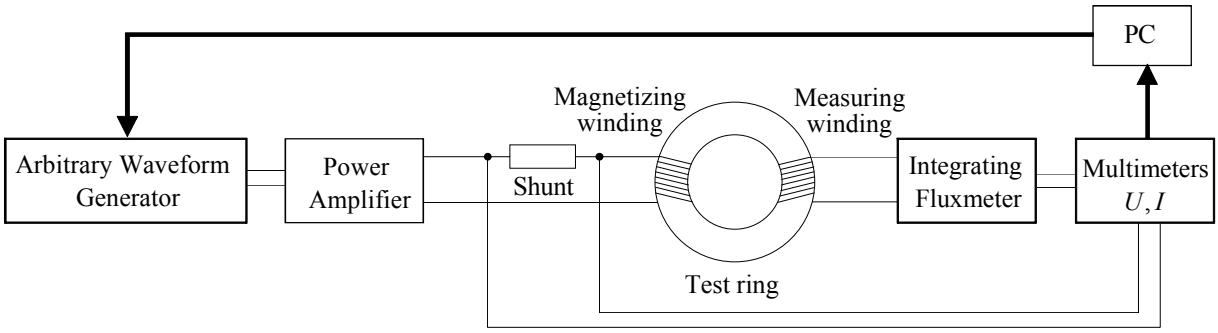

Fig. B1. The set-up for dc-field measurements.

List of devices:

Arbitrary Waveform Generator: AWG 2005, Sony-Tektronix

Power Amplifier: Switching Amplifier SW 5250A, Elgar Corporation

Shunt: Nebenwiderstand N 20; 15 A, 300 mV

Integrating Fluxmeter: MF-3D, Walker Scientific

Two Multimeters: Fluke 8842A

Appendix C. Core loss separation measurement on a wound-ring sample

The set-up for the core loss separation measurements on a wound-ring sample is shown in Fig. C1. The parameters of the wound-ring sample are summarized in Appendix A. The ring was wound with magnetizing and measuring windings. The whole measurement is controlled by a PC, which instructs an Arbitrary Waveform Generator about the frequency and magnitude of input sinusoidal voltages. The signal is amplified in a Power Amplifier and fed into the magnetizing winding of the test ring. The negative feedback to the Power Amplifier keeps the voltage on the ring terminals sinusoidal. The extra resistor is connected to the primary circuit in order to keep the dc value of the current as small as possible. The data from a Power Analyzer are transferred to the PC and collected into files.

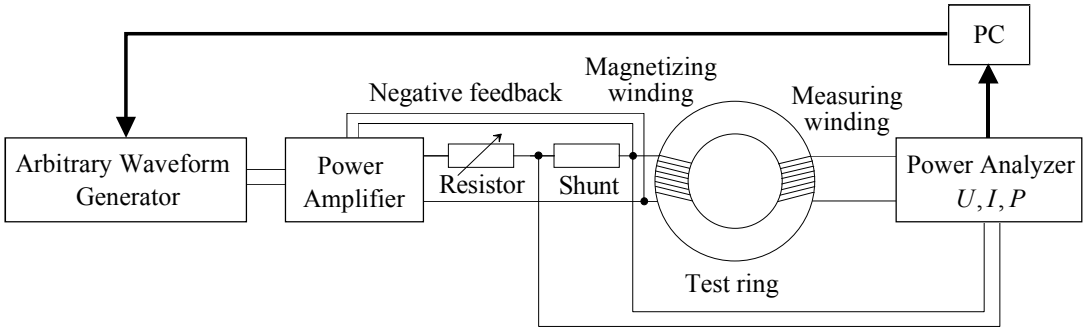

Fig. C1. The set-up for core loss separation measurements.

List of devices:

Arbitrary Waveform Generator: AWG 2005, Sony-Tektronix

Power Amplifier: Switching Amplifier SW 5250A, Elgar Corporation

Resistor: 20 Ω, 3.9 A

Power Analyzer: Wide Band Power Analyzer D 6100, Norma

Shunts: Norma LEM shunts 0.1 A - 10 A; accuracy: ± 0.03 % of rdg.
0.03 A - 1 A; accuracy: ± 0.1 % of rdg.

Appendix D. Main parameters of the test induction motors

TABLE D1. THE MAIN PARAMETERS OF THE TEST INDUCTION MOTORS.

Parameter: Motor:	30 kW	37 kW	315 kW
Number of pole pairs	1	2	2
Number of phases	3	3	3
Outer diameter of the stator core [mm]	323	310	600
Air-gap diameter [mm]	189	199	378
Core length [mm]	183	249	529
Number of stator slots	36	48	72
Number of rotor slots	28	40	52
Connection	delta	star	delta
Rated voltage [V]	400	400	400
Rated frequency [Hz]	50	50	50
Rated current [A]	53	72	523
Rated power [kW]	30	37	315

Appendix E. Experimental set-up for the hysteresis torque and core loss measurements on the test induction motors

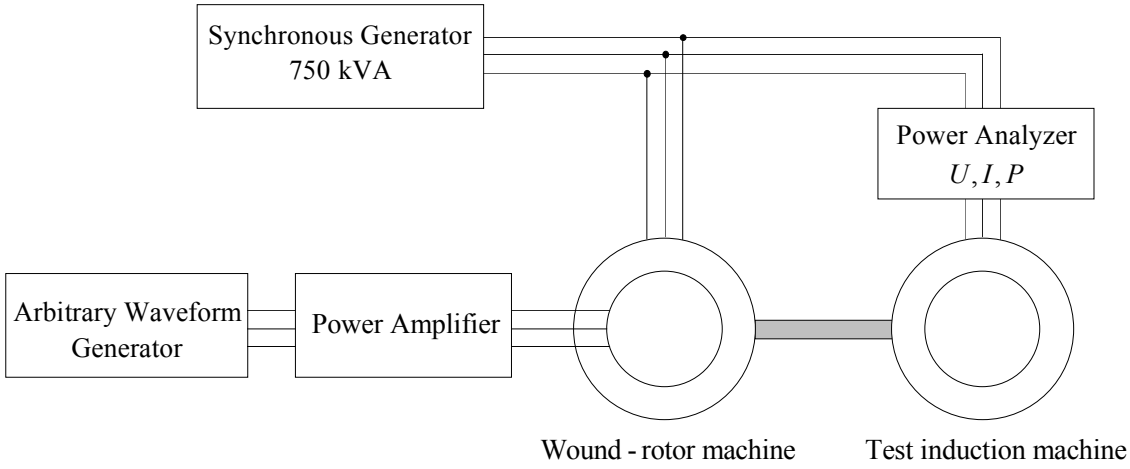

Fig. E1. A cage-induction motor hysteresis torque and core loss measuring set-up.

List of devices:

Arbitrary Waveform Generator: AWG 2005, Sony-Tektronix

Power Amplifier: Switching Amplifier SW 5250A, Elgar Corporation

Power Analyzer: Wide Band Power Analyzer D 6100, Norma
Accuracy of the active-power meter in AC+DC mode:
power factor 1: measuring error < 0.2 %
power factor 0.1: measuring error < 0.3 %
power factor 0.01: measuring error < 1 %

Shunts: Norma LEM shunts: 0.1 A - 10 A; accuracy: ± 0.03 % of rdg.
0.3 A - 50 A; accuracy: ± 0.03 % of rdg.
3 A - 100 A; accuracy: ± 0.03 % of rdg.
6 A - 300 A; accuracy: ± 0.1 % of rdg.

Test induction motors: 30 kW, 37 kW and 315 kW (Appendix D)

Wound-rotor motors: 4-pole, 0.9 kW, 380 V (in connection with the 30 kW and 37 kW motors)
4-pole, 18.5 kW, 380 V (in connection with the 315 kW motor)

The connection shown in the sketch in Fig. E1 is directly valid for the 37 kW and 315 kW test motors. In the case of the 2-pole 30 kW test motor, two extra synchronous machines (4-pole and 8-pole) were connected in between the synchronous generator and wound-rotor machine.

Appendix F. Cross-sectional geometries and finite element meshes of the test induction motors

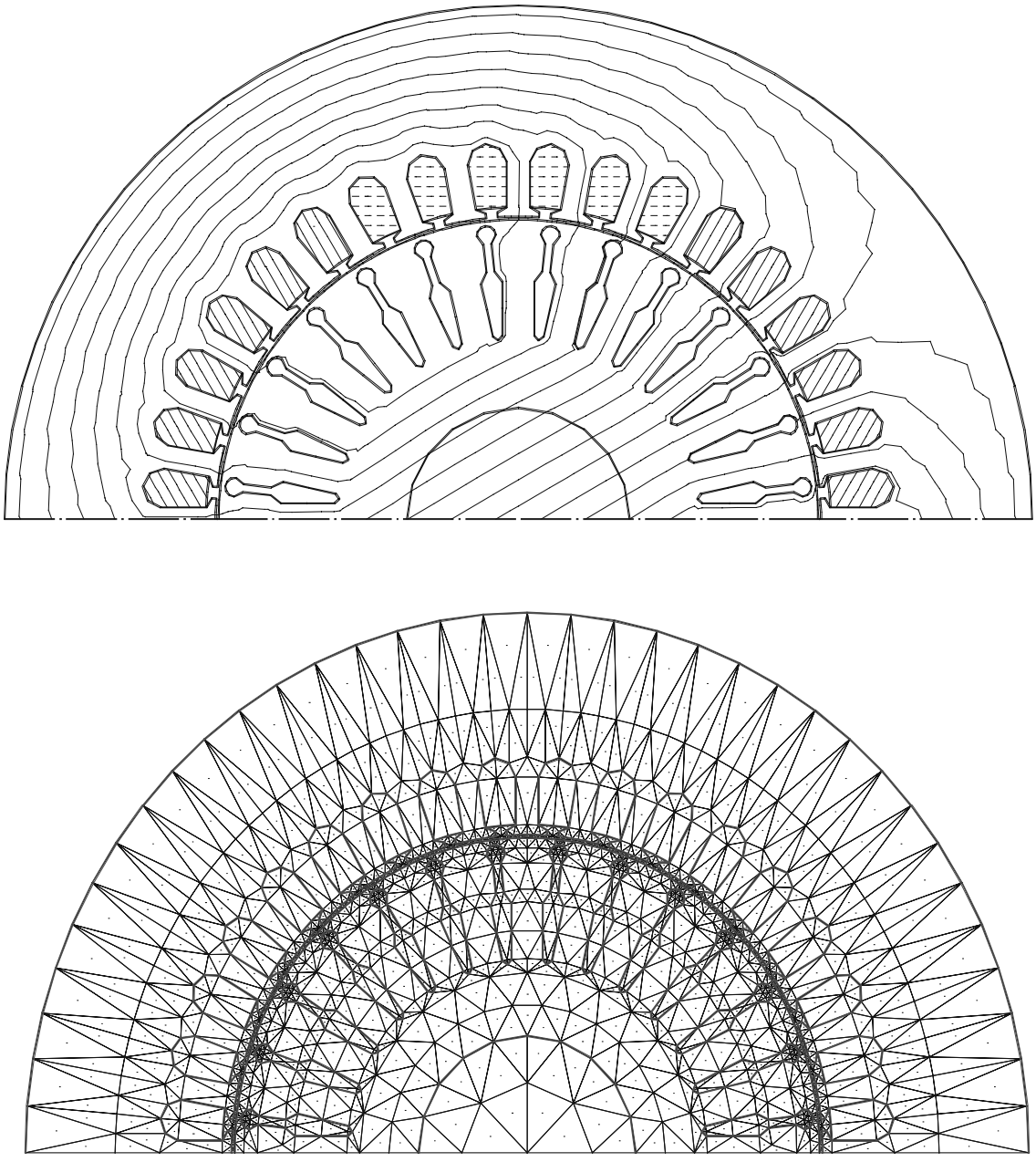

Fig. F1. The geometry, DC field and finite element mesh of the 30 kW test induction motor.

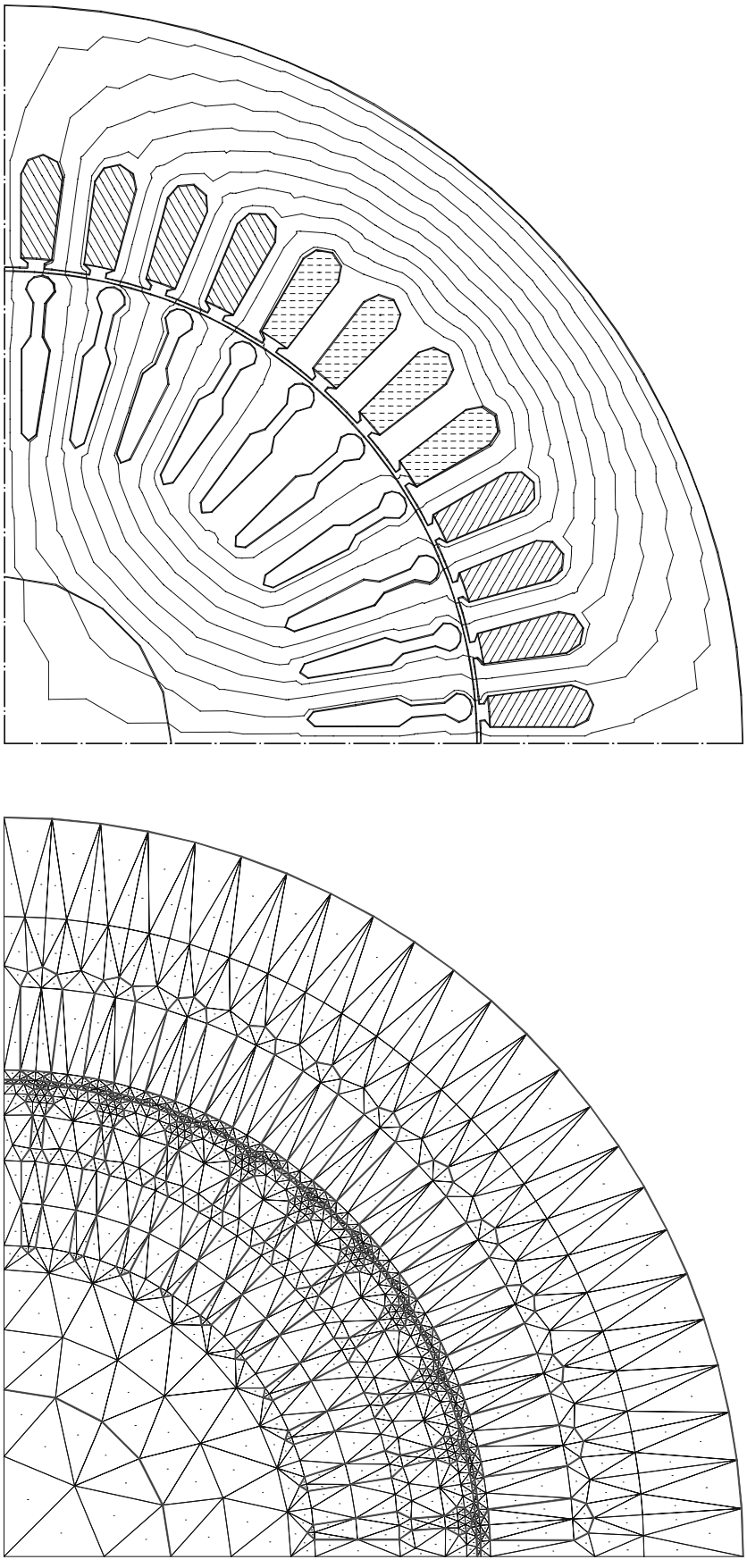

Fig. F2. The geometry, DC field and finite element mesh of the 37 kW test induction motor.

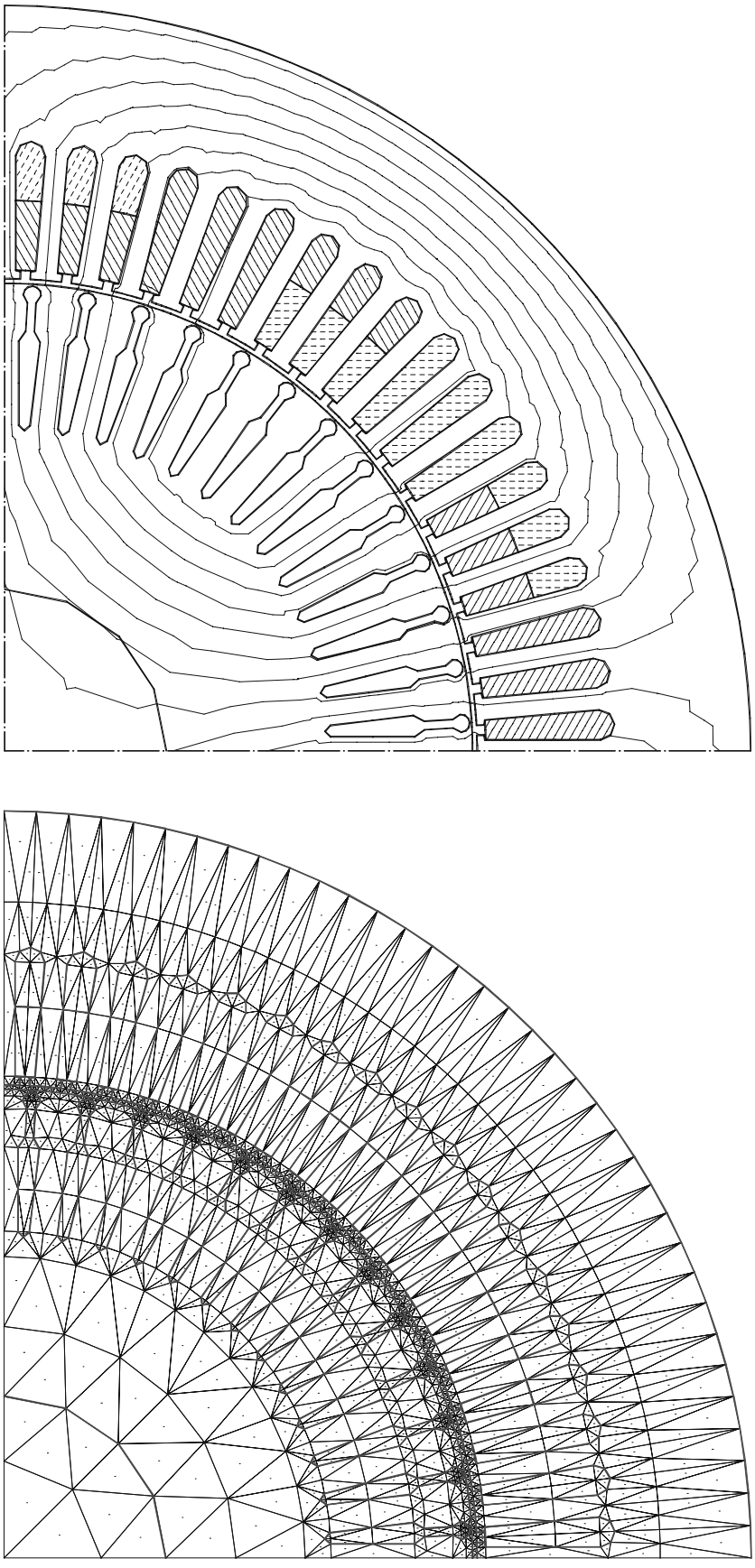

Fig. F3. The geometry, DC field and finite element mesh of the 315 kW test induction motor.